Novel synthesis of functional carbon forms and their energy applications

A thesis submitted to the University of Pune for the degree of Doctor of Philosophy in Chemistry by

Rohan Rajeev Gokhale

Dr. (Mrs) Jyoti P. Jog (Research Guide)

Dr. Satishchandra B. Ogale (Research Co-Guide)

Polymer Science and Engineering Division, Physical and Materials Chemistry Division, National Chemical Laboratory, Pune- 411008, India

July 2014

सीएसआयआर–राष्ट्रीय रासायनिक प्रयोगशाला
(वैज्ञानिक तथा औद्योगिक अनुसंधान परिषद)
डॉ. होमी भाभा मार्ग, पुणे – 411 008. भारत
CSIR-NATIONAL CHEMICAL LABORATORY
(Council of Scientific & Industrial Research)
Dr. Homi Bhabha Road, Pune - 411008. India

Certificate

This is to certify that the work presented in the thesis titled '**Novel synthesis of functional carbon forms and their energy applications**' by Rohan Rajeev Gokhale, submitted for the degree of **Doctor of Philosophy in Chemistry** was carried out under our supervision at the Polymer Science and Engineering Division and the Physical and Materials Chemistry Division, National Chemical Laboratory, Dr. Homi Bhabha Road, Pune- 411008, India. All the material obtained from other sources has been duly acknowledged in this thesis.

Dr. (Mrs) Jyoti P. Jog (Guide)
Scientist G (Retired)
National Chemical Laboratory,
Dr. Homi Bhabha Road,
Pune-411008, India

Dr. Satishchandra B. Ogale (Co-guide)
Chief Scientist
National Chemical Laboratory,
Dr. Homi Bhabha Road,
Pune-411008, India

Communication Channels
NCL Level DID : 2590
NCL Board No. : +91-20-25902000
EPABX : +91-20-25893300
: +91-20-25893400
FAX
Director's Office : +91-20-25902601
COA's Office : +91-20-25902660
COS&P's Office : +91-20-25902664
WEBSITE
www.ncl-india.org

Declaration

I, Mr. Rohan Rajeev Gokhale, hereby declare that the work incorporated in my thesis titled '***Novel synthesis of functional carbon forms and their energy applications***' was carried out by myself, for the degree of **Doctor of Philosophy** in **Chemistry**, under the guidance of Dr. (Mrs) Jyoti P. Jog and Dr. Satishchandra B. Ogale. This work has not been previously submitted to this University or any other University for the degree of PhD, or any other degree. Any material that has been obtained from other sources, has been duly acknowledged in this thesis.

Date: July 24, 2014

Place: NCL, Pune

Rohan Rajeev Gokhale

(Research Student)


Dedicated to my family, friends and teachers

Acknowledgement

I take this opportunity to thank all who have been instrumental in the completion of my PhD research and thesis.

Firstly, I would like to thank Dr. Satishchandra B. Ogale for giving me an opportunity to work under his guidance at the National Chemical Laboratory (CSIR). His influence on my work, philosophy and life has been phenomenal. He gave me the creative space and freedom which every researcher earnestly desires. Not only has his guidance been tremendously inspiring in our scientific endeavours but his general approach and philosophy towards life and people has also helped us grow as human beings. I would also like to thank Dr. (Mrs) Jyoti P. Jog for her constant support, encouragement and comforting influence.

I take this opportunity to express my gratitude to Dr. S. Sivram (former Director, NCL), Dr. Sourav Pal (Director, NCL), Dr. M. G. Kulkarni (former Head of PSE division), Dr. Verma (Head of PSE division), Dr. Anil Kumar (Head of Physical and Materials Chemistry Division) for providing the infrastructure and advanced facilities for research and giving me an opportunity to work at CSIR-NCL. I would also like to acknowledge the role of University Grants Commission (UGC), Govt. of India for providing me with research fellowships during my PhD study period.

I wish to thank our collaborators Dr. Beatrice Hannoyer, Dr. Sreekumar Kurungot, Dr. Vanchiappan Aravindan, Dr. Srinivasan Madhavi, Sreekuttan M. Unni and Joyasis Debgupta for all the help and support during the course of the research work. I thank all the journal editors, reviewers of our published articles and the editors, authors who have allowed us to reprint their published material in this thesis.

I would like to thank my teacher Dr. Lakshmy Ravishankar for inspiring us in the way she did during our BSc. days and later on as well. Her motivation is definitely the single largest force that guided me towards a PhD degree and a future career in scientific research. The Vaze college study circle with great friends like Nilesh, Charuta, Mahesh, Adil, Rohit, Sudhir and Nishikant, is indeed a wonderful academic memory of the time. I would also like to thank my teachers in the Dept. of Chemistry, Vaze college, Dr. Alka Kolhatkar, Dr. Awale, Dr. V. Paanse and Dr. G.G Pusalkar

for their help and support. I would like to thank Dr. Konde-Deshmukh for his help and encouragement during my MSc. days at Fergusson College, Pune.

Words cannot express my indebtedness to my grandparents, Prof. L. N. Gokhale and Dr. (Mrs) Shobhana Gokhale. Their love, encouragement and support has always been a pillar of strength and inspiration in my life. I feel their loss tremendously and only wish they were here to see this. May their souls rest in peace.

I wish to thank my family, Aai, Baba and Ritwik for their constant and unconditional love, support and comfort. My mother's constant emphasis on the importance of education, ambition and her scientific curiosity has always been a guiding light for me. I wish to thank my lovely wife Charuta for her unconditional love and friendship. She has unhesitatingly shared all my joys and pains in equal measure and made them her own.

I deeply acknowledge the help and support from my laboratory friends/intern students, Dr. Rajesh, Dr. Vivek Dhas, Dr. Subas, Dr. Abhimanyu, Dr. Anup, Dr. Arif, Dr. Parvez Shaikh, Dr. Vivek Antad, Dr. Harish, Dr. Ashish, Prasad, Vishal, Upendra, Satyawan, Pradeep, Satish, Yogesh, Wahid, Umesh, Sambhaji, Sumit B, Kush, Sarika, Divya, Meenal, Lily, Mandakini, Reshma, Shruti, Dipti, Dhanya, Megha, Pooja, Shraddha, Mukta, Ketaki, Nilima, Aparna, Rupali, Shital, Srashti, Kalyani, Anand. Special thanks to my seniors/friends, Dattakumar Mhamane, Anil Suryawanshi and Vishal Thakare for their tremendous help during the laboratory research work. Happy cheers to the gang of friends, Abhik, Prasad, Rounak, Pravarthana and Aniruddha for all our memorable trips, fun and work together.

I wish to thank my best friends, Aditya Kulkarni and Vaibhav Pitale for always being there for me. I must also acknowledge the great time I had with my friends and cousins, Adwait, Akshay, Ashwini, Aditya, Saloni, Tanu, Chandrahas and others. Thanks are also due to my relatives, my maternal grandparents, Arun mama, Anju atya, Sanjeev mama, Subod mama, Smita mami, Nina maushi and all others for their constant support.

Finally, I thank the almighty God and the holy respected gurus, Swami Vivekananda and Shri Paramhansa Yoganandaji for being with me all the way.

List of Abbreviations

Abbreviation	Name
AC	Activated Carbon
AEMFCs	Anion Exchange Membrane Fuel Cells
CNS	Carbon nanosphere
CNTs	Carbon Nanotubes
CVD	Chemical Vapour Deposition
DCB	o-Dichlorobenzene
DSSCs	Dye sensitized solar cells
EDLC	Electrochemical double layer capacitor
FE SEM	Field emission scanning electron microscopy
FWHM	Full width at half maximum
FTO	Fluorine doped tin oxide
FTIR	Fourier Transform Infrared Spectroscopy
GQDs	Graphene Quantum Dots
GFMC	Gram flour derived mesoporous carbon
HOPG	Highly Oriented Pyrolytic Graphite
HR TEM	High resolution transmission electron microscopy
Li-HEC	Lithium ion hybrid electrochemical capacitor
LIBs	Lithium ion batteries
MWNTs	Multi-walled carbon nanotubes
ODC	Oligomer derived carbon
PL	Photoluminescence
PVC	Poly Vinyl Chloride
PLD	Pulsed laser deposition
PLPS	Pulsed Laser-induced Photochemical Stitching
PTFE	Poly tetrafluoro-ethylene
RDE	Rotating disk electrode
SWNTs	Single-walled carbon nanotubes
SEM	Scanning electron microscopy
TEM	Transmission electron microscopy
TGA	Thermogravimetric analysis
UV	Ultraviolet
XPS	X-ray photoelectron Spectroscopy
XRD	X-ray diffraction

Contents

Abstract

Carbon materials form one of the widest applicable systems in recent days all over the world. Carbon macro, meso and nano forms have been used in applications ranging from water purification, sensors, electronics, gas adsorption and storage to energy storage and generation devices. The most recent energy applications of carbon materials include generation devices like fuel cells and solar cells and storage devices like supercapacitors and batteries. Traditionally carbon has been synthesized by physical and chemical methods that include chemical vapour deposition, pulsed laser deposition, arc discharge, pyrolysis, hydrothermal or chemical synthetic routes. Carbon exhibits diverse range of properties which make it a material of such high utility. Depending on the structure, morphology and specific allotrope nature, carbon can demonstrate high electronic conductivity (CNTs, Graphene etc.) or have an insulating nature (Diamond). Different carbon systems possess high surface area, high tensile strength, thermal conductivity and several other properties which make them highly applicable materials.

In this thesis, a new photochemical route towards the synthesis of carbon materials has been explored. This process involves a rapid photochemical reaction of free radicals resulting in the formation of carbon nano-forms. The process can take place at room temperature and ambient conditions. This bottom-up method involves the use of small haloaromatic molecule precursors. We demonstrate that this process can be used to make a range of carbon nanoparticles and films. It is also shown that this photochemical route presents new avenues and possibilities of formation of novel carbon structure that have been hitherto unexplored. The catalytic properties of the carbon films generated by this method have been tested and proved to be effective counter-electrodes in dye sensitized solar cells (DSSCs) with energy conversion efficiencies comparable to the Pt based electrodes. Furthermore, the use of natural protein rich food waste precursors like gram flour has also been investigated in order to introduce heteroatom dopants in the final carbonized product. A method of ‘cooking’ the gram flour in SiO_2 nanoparticle-water dispersion has been used. The SiO_2 particles were later removed by HF treatment in order to generate pores. The N doped carbon system synthesized by this method has been used as an efficient oxygen reduction electrocatalyst at the cathode of fuel cells. Similarly porous 3D graphene-

like carbon has been synthesized by a unique molecular level activation method. This was done by synthesis of a specific oligomer which possesses functional groups that can create porosity during pyrolysis. The carbon has been used for energy storage in a Lithium ion hybrid electrochemical capacitor (Li-HEC).

In the **first chapter**, introduction to carbon and its various forms, properties, synthesis protocols and applications has been presented. A scope of the present work has also been included.

In the **second chapter**, basics of synthesis protocols and characterization methods used in the thesis have been described.

In the **third chapter**, an introduction to the concept of Pulsed Laser-induced Photochemical Stitching (PLPS) has been presented. The use of UV laser irradiation on dichlorobenzene and chlorobenzene molecules to generate carbon nanospheres and carbon based composites has been described. A plausible mechanism for the new phenomenon has been studied.

In the **fourth chapter**, the PLPS method has been used to make carbon films with a broccoli like morphology. The films synthesized on FTO coated glass substrates have been used as counter-electrodes in DSSCs. The growth process and morphology of the films have been studied.

In the **fifth chapter**, the synthesis of a hetero-atom doped carbon system from protein rich food precursor namely gram flour has been explored. The hierarchically porous carbon material exhibited excellent electrocatalytic activity in the cathodic oxygen reduction reaction of fuel cells.

In the **sixth chapter**, synthesis of a novel oligomer salt from 4-amino benzoic acid as the starting material has been explored. This oligomer salt was pyrolyzed to obtain 3D n-graphene cage like self assembly which exhibited a high surface area. The material showed excellent charge storage properties in a Li-HEC device.

In the **seventh chapter**, a summary of the thesis has been presented along with a possible future direction of research work.

Finally, the **appendix** describes a parallel application of PLPS generated carbon films in field emission and the use of PLPS to generate blue luminescent Graphene Quantum Dots (GQDs).

Chapter 1

Introduction

This chapter gives a basic introduction to the premise of the research work described in this thesis. A broad introduction to the basics of carbon, different types of carbon, the synthesis protocols and the diverse applications is presented. This chapter also lays out a roadmap for the direction of research presented in this thesis.

1. Carbon: An Introduction

Of all the elements historically described in the periodic table, Carbon is one of the most intriguing, widely studied and explored element in nature. It is the fourth most abundant element in the universe by mass after Hydrogen, Helium and Oxygen. Carbon is classified as a non-metal in the periodic table and exists in Group 14 along with other elements like Silicon (Si), Germanium (Ge), Tin (Sn) and Lead (Pb). This group of elements exhibit a property of catenation (formation of bonds with atoms of the same element) which is seen most remarkably in carbon owing to its smaller size. The atomic number of carbon is 6 and it has an approximate mass number of 12. It also exists in rare isotopic forms with mass number of 13 and 14. ^{14}C is a radioactive isotope and its presence in systems helps is determining the age of the sample by a process called radio-carbon dating. The carbon has an electronic configuration of $1s^2$, $2s^2$, $2p^2$, with a partially filled p orbital. The atom has a radius of 0.077 nm.

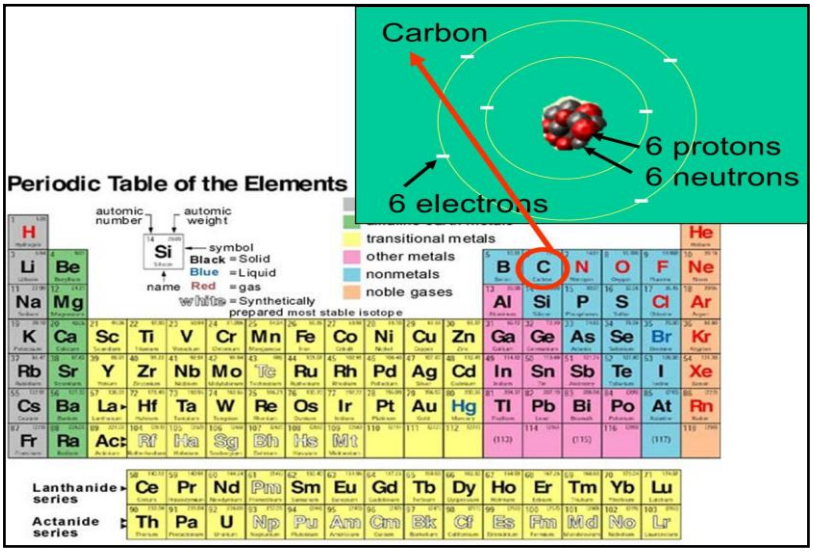

Figure 1.1 *Periodic table (Image from Reference 1)*

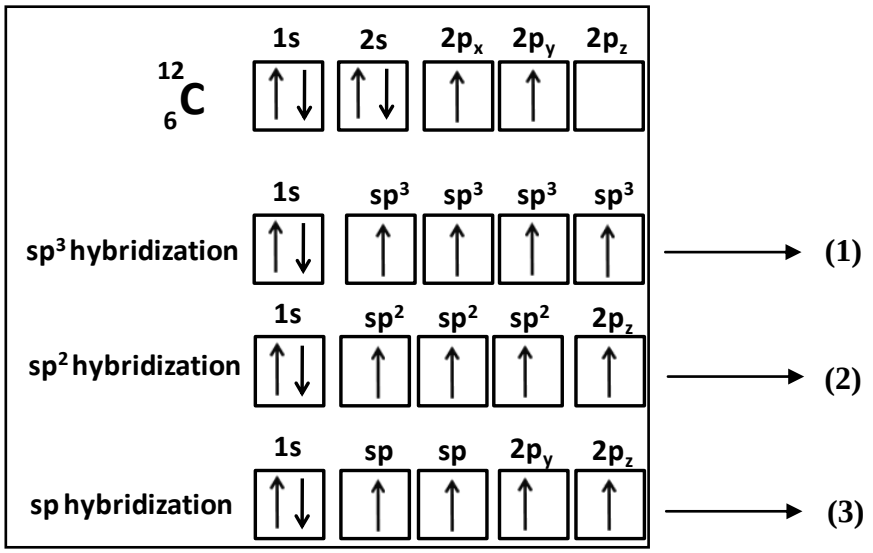

Figure 1.2 *Electronic configuration of carbon atom and its various hybridization states*

Figure 1.2 shows the electronic configuration of carbon atom. Depending on the condition and the type of compound formed by the element, carbon exhibits various hybridization states. These are (1) **sp^3** (tetrahedral structure with a bond angle of 109^o 28') eg. CH_4, CCl_4 (2) **sp^2** (planar trigonal with a bond angle of 120°) eg. –C=C–alkenes (3) **sp** (linear with a bond angle of 180^o) eg. -C≡C- acetylenes.

The unique property of catenation (covalent linkage of similar atoms into long chains) and existence of different hybridization states causes the carbon to exist in different allotropic forms ranging from diamond to graphite and exhibit a plethora of physical and chemical properties. Due to the formation of different polymorphs with varying microstructures by the carbon atom building block, several interesting properties can be attributed to each carbon structure. Carbon materials exhibit a wide variety of applications like catalysis/catalytic supports, super-adsorbents, gas storage, electrochemical charge storage etc. In addition to the carbon structures there are numerous compounds of carbon with elements like H, N and O which form the building block of life and form an entire branch of chemistry called organic chemistry.

The global carbon industry which includes diamond, graphite, carbon fibers is a multi-billion dollar industry (~5.5-7.5 billion dollars) for variety of applications.[2, 3]

Some of the important carbon polymorphs/allotropes along with their applications are described herein:

1.1 Different types of Carbon

1.1.1 Crystalline Allotropes of Carbon:

A. Diamond:

Figure 1.3 *Diamond crystals (Image from Reference 4)*

Diamond is a crystalline, meta-stable allotrope of carbon containing carbon hybridized in the sp^3 state and forming strong covalent bonds with each other. Due to this structural arrangement, diamond is one of the hardest known materials. The atoms in carbon are arranged in a variation of the face-centred cubic lattice form called the diamond lattice. Natural diamonds are formed naturally deep in the earth's mantle under very high pressure and temperature and they are subsequently brought to the surface by volcanic eruptions. Similar conditions have also been created artificially to manufacture synthetic diamond. Another method called chemical vapour deposition (CVD) has been used to synthesize artificial diamond. Diamond is thermodynamically less stable than Graphite. However the kinetics of the diamond to graphite transition is very slow and so there is no noticeable change in the phase. Diamonds are

electronically insulating in nature, possess a very high thermal conductivity (900–2,320 $W \cdot m^{-1} \cdot K^{-1}$) and a wide optical band gap of 5.5 eV which makes it transparent to visible light. The occasional colour obtained in diamonds arises due to defects or impurities eg. Boron doping (blue), Nitrogen doping (yellow) and lattice defects (brown). The use of diamond is mainly for ornamental/jewellery purposes and also for industrial cutting tools.[2, 3]

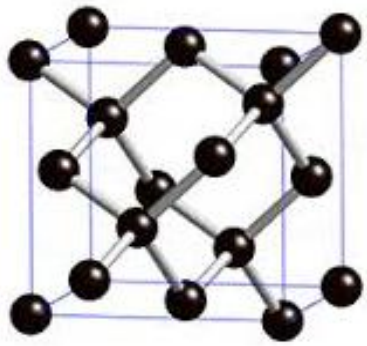

Figure 1.4 *Crystal structure of diamond (Image from Reference 2)*

B. Graphite:

Figure 1.5 *A block of Graphite (Image from Reference 2)*

The term Graphite originated from the greek term "Graphein" which means "to write". Graphite is the most stable (under standard conditions) naturally occurring crystalline form of carbon with a wide range of properties and applications. Graphite has a stack of carbon layers which are arranged in a hexagonal honeycomb like arrangement. The carbon atoms are sp^2 hybridized and form hexagonal covalent networks which constitute the planes. The electrons occupied in the p-orbital form a

delocalized electron cloud in the system. The distance between the carbon atoms in the plane is 0.142 nm and the distance between the carbon layers is 0.334 nm. The carbon layers are held together by weak Van der waal's forces and hence are loosely bound. The covalent in-plane carbon bonds have high bond energy of 524 kJ/mol and the interplanar bonds have a weak bond energy of 7 kJ/mol. Graphite is a semi-metal which exhibits anisotropic electronic conductivity. Graphite can conduct electricity in-plane (of the carbon layers) due electron delocalization. The material however does not conduct electricity vertical to the carbon planes. The Graphite layer stacking occurs in two different ways: hexagonal and rhombohedral. The hexagonal system has an –ABABAB- type stacking whereas the rhombohedral system has –ABCABC- type of stacking. These layers can slide over each other. Therefore Graphite can be used as a lubricant in various applications. Highly Oriented Pyrolytic Graphite (HOPG) is obtained by heating to temperatures above 2200^{o}C. Graphite is used a wide variety of applications like pencils, refractories, batteries, lubricants, brake linings etc. [2, 3]

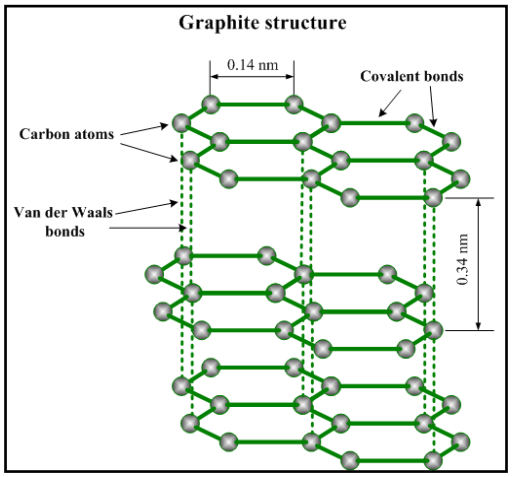

Figure 1.6 *Crystal structure of Graphite (Image from Reference 5)*

1.1.2 Different types of amorphous carbons:

A. Glassy carbon: This is a type of vitreous, non graphitizing, highly conducting carbon which combines ceramic properties with carbon. Glassy carbon is a hard carbon which is extremely resistant/inert to chemicals. It is generally derived from polymer/plastic precursor. It is widely used as electrodes in electrochemical systems.

B. Carbon black: Carbon black is a form of high surface area carbon (lesser than activated carbon). It is produced from the partial combustion of petroleum products. Carbon black is chiefly used as additive for structural reinforcement of materials.

C. Charcoal: Charcoal is a carbonaceous residue along with the ash formed by the partial pyrolysis of vegetable/animal substances like wood in the absence of air. Charcoal is chiefly used as a fuel in industries/cooking etc.

D. Coal: Coal is a fossilized carbon widely used as a fossil fuel. Coal is a combustible sedimentary rock formed inside the rock strata of earth under high temperature and pressure. It is mainly formed from organic precursors.[2]

E. Activated/Porous Carbon:

Activated carbon or porous carbon is a high surface area carbon material (surface are >500 m^2/g) that is being actively researched and commercially applied. Activated carbon consists of a large volume of pores in the range of 0.5-30 nm, termed as micro, meso and macropores. Activated carbon can be derived from any natural products/wastes after their charcoal formation or during the carbonization process itself. There are two kinds of activation processes:

Physical Activation: This process involves the treatment of precursors/pyrolyzed product at high temperatures in an oxidizing atmosphere i.e. in the presence of oxygen or steam. This physical activation process generates a lot of differently sized pores in the carbon product.

Chemical Activation: This process involves the addition of pore creating chemicals into the precursors before their carbonization process. The chemicals typically used are acids, strong bases and salts eg. KOH, H_3PO_4, NaOH, $CaCl_2$ etc. Chemical activation is a widely used process to generate activated carbon.

$6KOH + 2C \text{ ----> } 2K + 3H_2 + 2K_2CO_3$..... (1)

Equation 1 shows the activation reaction wherein the potassium hydroxide reacts with carbon to generate pores.[6]

Another strategy to generate porous carbon structures is commonly referred to as a templating strategy. Different kinds of templating; namely hard and soft template strategies have been used to generate porous carbon. Carbon has been synthesized from chemical, polymer or natural precursors by incorporating the precursors along with hard templates like SiO_2 nanoparticles, mesoporous silica

(SBA 15) or calcium carbonate ($CaCO_3$). These templates are removed post carbonization by treatment with strong acids or base and the porous carbon is thus generated. Soft templating strategies like synthesis of co-polymers wherein one unit generates carbon and the other unit decomposes giving rise to pores during the pyrolysis process have also been explored in literature. [2, 3, 7, 8]

Activated/porous carbon is used in several applications like water purification, gas adsorption/storage, air purification, catalysis, electrochemical energy storage etc.

Figure 1.7 *(A) Blocks of coal (image from Reference 9) (B) Charcoal blocks (image from Reference 2) (C) Porous activated carbon*

1.1.3 Carbon Nanomaterials:

Along with the well established and studied carbon structures describes previously, there are several carbon nanostructures which have been discovered, synthesized, studied and applied in the last 10-20 years giving a strong impetus to the rise in the field of nanotechnology. Some of the important carbon nanostructures are:

A. Fullerenes: Fullerenes were discovered and explained first in 1995 by Curl, Kroto and Smalley. They were also termed as bucky-balls. Fullerenes are nano-meter sized carbon balls made from the graphitic structure of sp^2 carbon hexagonal rings. There are also pentagonal rings/defects present in these

structures which assist in the curvature. The van der Waals diameter of fullerene is ~ 1.1 nm. Fullerenes with number of carbon atoms 60 and 70 are fairly common, but those with 72, 76, 84 and 100 are reported. Fullerenes are stable but react chemically to some extent. Some atomic species are known to be trapped inside fullerenes giving rise to what is known as endohedral fullerenes eg. K intercalated C_{60}. Fullerenes are used in several applications like biology and superconductivity.[2, 3]

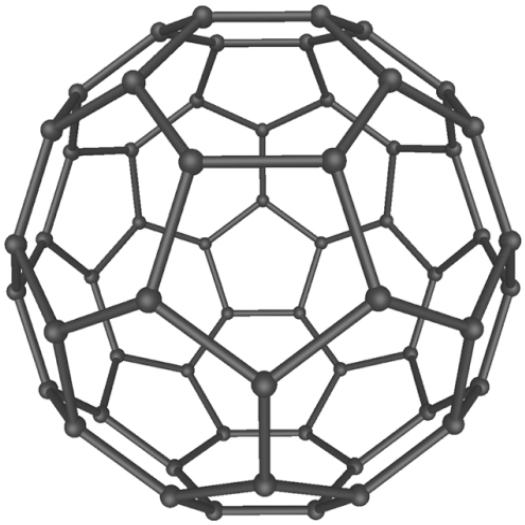

Figure 1.8 *Fullerene structure (Image from Reference 2)*

B. Carbon Nanotubes: Carbon nanotubes are open/closed ended cylinders of carbon formed by the rolling of graphene like sheets. CNTs can be classified into single layer boundary called single-walled carbon nanotubes (SWNTs). When cylinders are formed from multiple layers to form a hollow concentric assembly, these structures are called Multi-walled carbon nanotubes (MWNTs). The precise distance between these layers is the graphitic distance of 0.334 nm. MWNTs form in the range of 2-25 nm. Depending on the chirality or configuration the 'armchair' tubes are metallic in nature and the zigzag/helical tubes could possess either metallic or semiconducting properties. Carbon nanotubes present a unique and very high electronic conductance because the electrons are confined only to the graphene sheet in the radial direction. They can carry a very high amount of electronic current (theoretically $4*10^9$ $A.cm^{-2}$). The band gap of CNTs is inversely proportional to their diameter i.e. as the diameter of the tubes increases the band gap tends to zero. In addition to these carbon nanotubes possess properties like high tensile strength. They are known to be the strongest and stiffest materials known. A tensile strength of 63 G-Pa is recorded in CNTs. CNTs are also known to be biologically toxic in nature. CNTs can be synthesized by several methods like chemical vapour deposition (CVD), laser ablation, arc discharge etc. using metal catalysts like Fe/Ni. CNTs have been used for a very large number of applications like devices and electronics, for structural reinforcements in materials, textiles, batteries, supercapacitors, hydrogen storage etc.[2, 3, 10]

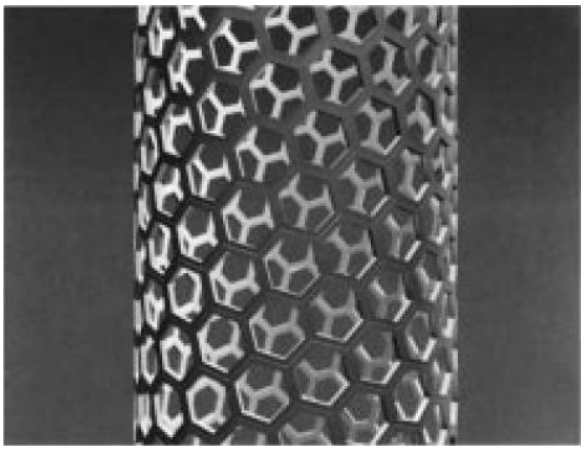

Figure 1.9 *Carbon Nanotubes (Reprinted with permission from P. M. Ajayan, Chem. Rev. 1999, 99, 1787−1799, Copyright (1999) American Chemical Society)*

C. Graphene: Graphene is the recent phenomenon; a 0D single layer of sp^2 carbon which forms a basic building block of several extended honeycomb graphitic structures. Graphene was first isolated in 2004 at the University of Manchester by Geim and co-workers using a novel scotch tape based top-down extraction from a highly oriented pyrolytic graphite (HOPG) precursor. Several synthetic strategies have been subsequently developed to generate graphene eg. chemical vapour deposition, laser ablation, bottom-up synthesis from organic molecules and chemical oxidation/exfoliation of graphite to graphene oxide followed by its reduction to few layers of reduced graphene oxide. Graphene possesses a very high theoretical surface area of 2600 m^2/g. This 2D crystal shows extraordinary electronic properties. Graphene exhibits a ballistic electron transport with a mobility of 200,000 $cm^2\ V^{-1}\ s^{-1}$. Graphene can be chemically functionalized to form composites with other systems like metal oxides and polymers. Graphene has a potential application in electrochemical energy storage systems, sensors, solar cells, electronics etc.[2, 3, 11]

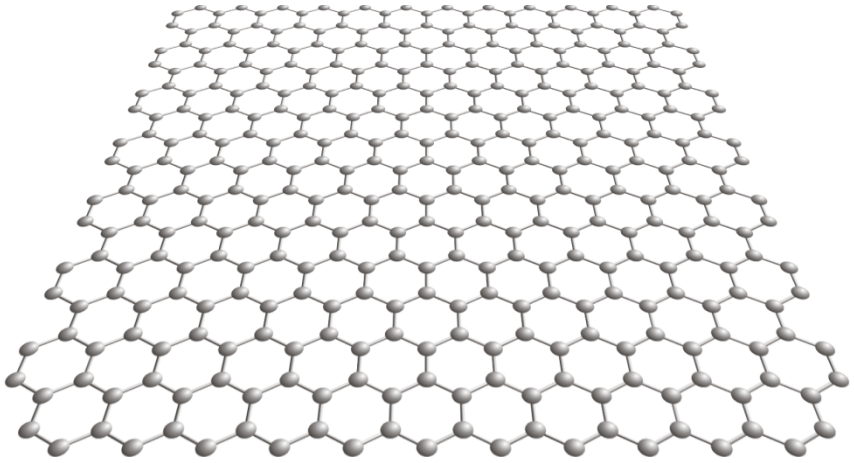

Figure 1.10 *Graphene sheets (Image from Reference 12)*

D. Graphene Quantum Dots: Graphene quantum dots (GQDs) are a newly discovered class of luminescent carbon nanoparticles which have found potential applications ranging from bio-imaging to sensors. GQDs are nanometer-sized fragments of graphene within the range of 1-100 nm. The electronic transport in GQDs is confined in all three dimensions. GQDs exhibit size dependent band gap variation. GQDs show luminescence in different ranges ranging from a quantum yield of 1-25%. GQDs can be synthesized in different ways; top-down approaches include hydrothermal, solvothermal and electrochemical cutting of bulk graphene. Bottom-up approaches include organic synthesis approaches from small aromatic molecules. GQDs can be functionalized to be made solution processible. GQDs have been used in several applications like photovoltaics, organic light emitting diodes, bio-imaging, biosensing, environmental monitoring.[13]

In addition to these materials, several other nanoforms of carbon exist and have been investigated till date. Eg. carbon nanohorns, carbon nanospheres, carbon nanofibers etc.

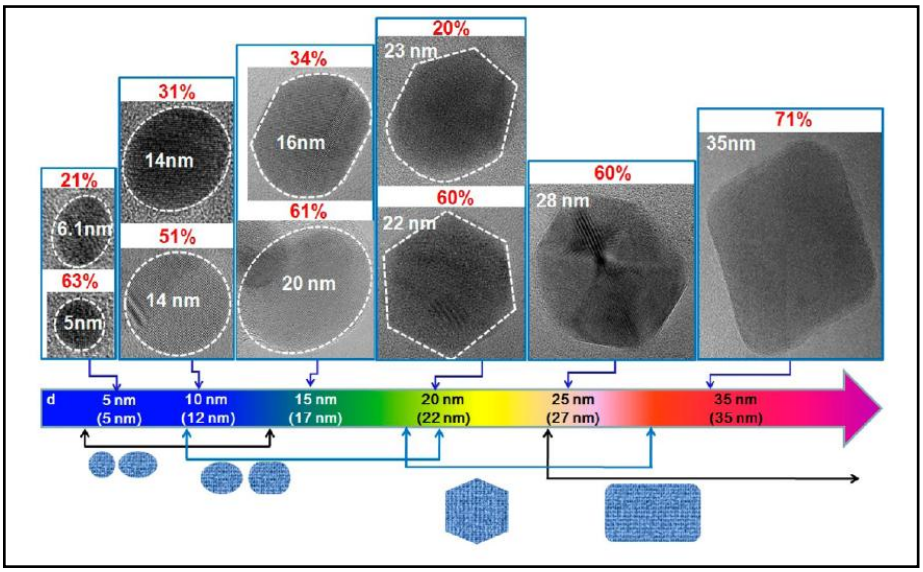

Figure 1.11 *Graphene quantum dots at different shapes and sizes (Reprinted with permission from Kim et al. ACS Nano 2012, 6, 8203, Copyright (2012) American Chemical Society*

1.2 General routes for carbon synthesis:

A. Chemical Vapour Deposition:

Chemical Vapour Deposition (CVD) is a technique which is widely used in industrial synthesis of carbon nanomaterials like CNTs, Graphene and bulk materials like Diamond. CVD involves the use of a substrate/catalytic substrate which is exposed to volatile organic compounds that react or decompose on its surface under specific conditions. A gas flow removes the by-products of the reaction. CVD can be classified into several categories that include pressure operated techniques like low pressure CVD, plasma methods like plasma- enhanced CVD, deposition methods like atomic layer CVD etc.[2, 14]

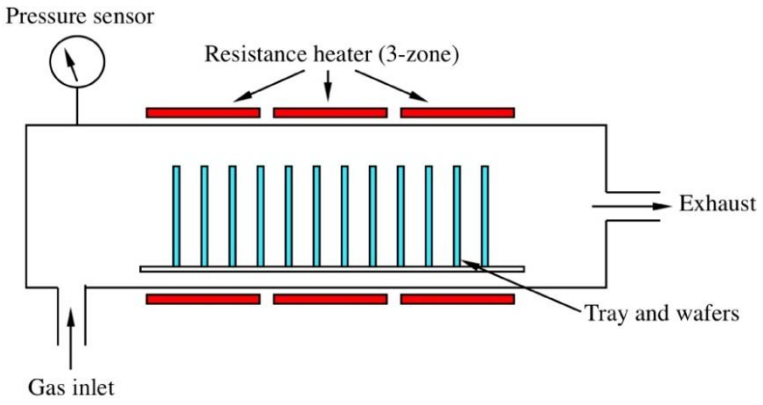

Figure 1.12 *Chemical Vapor Deposition (Image from Reference 15)*

B. Arc Discharge:

Carbon nanomaterials like Single Walled Carbon Nanotubes (SWNTs) have been synthesized by an electric arc based method. In the process, a helium atmosphere (660 mbar) is used in which an electric arc is generated between two electrodes in a reactor. A graphite rod is used as the cathode (16 mm diameter, 40 mm long) and another graphite rod (6 mm diameter, 100 mm long) with a hole (3.5 mm diameter, 40 mm deep) in between containing a catalyst with graphite powder is used as the anode. An arc of 100 A current and a voltage drop of 30 V between these two electrodes is

observed. Co and Ni catalyst were used in the process. Similar arc discharge processes have been used for synthesis of carbon materials. [16]

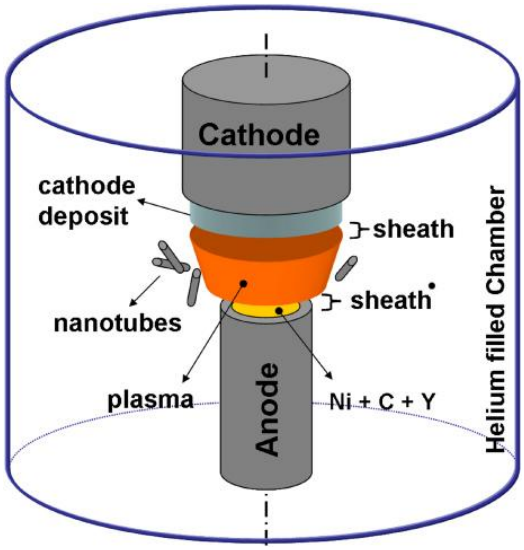

Figure 1.13 *Arc Discharge setup (Image from Reference 17)*

C. Hydrothermal carbonization:

The term 'hydrothermal' is of geologic origin. Hydrothermal treatment involves the high pressure and high temperature treatment of precursor materials in an aqueous environment. Hydothermal carbonization is a technique of carbon formation by such a method from different precursors especially natural precursors and chemicals. A steel pressure vessel along with a Teflon container called Autoclave is used for the process. A temperature of 180-200 ^{o}C is used normally during the synthesis. Several rapid and random chemical reactions like hydrolysis, dehydration, decarboxylation, polymerization and aromatization lead to the carbon formation process from the precursor in this type of process.[18]

Figure 1.14 *Hydrothermal bomb and autoclave (Image from Reference 19)*

D. Pyrolysis:

Pyrolysis is the high temperature treatment (generally > 500 C) of materials in the absence of oxygen in an inert atmosphere (Ar, N_2 etc.). Pyrolysis leads to a process called graphitization at high temperatures. Soft carbon sources yield graphite-like conducting carbons at lower temperatures, whereas hard carbon sources yield graphite like materials only at a very high temperature. A split tube furnace with a constant Argon or N_2 flow is generally used for the pyrolysis process. A ceramic tube and boat is used as the apparatus. Carbon has been synthesized by pyrolysis from several precursors like natural wastes, biomass, polymers, chemicals etc.

In addition to this, carbon nanomaterials have also been synthesized by different chemical methods like organic synthetic techniques, exfoliation of graphites, electrochemical methods etc.

1.3 Important Energy Applications of Carbon

A. Electrochemical Double Layer Capacitors:

Out of the various energy storage systems, supercapacitors are one of the most important devices because of their rapid charging and discharging properties. Supercapacitors are rendered as an excellent and more attractive energy storage option compared to conventional capacitors because of important characteristics like long cycle life and high energy density. EDLCs have higher power density as compared to lithium ion batteries (LIBs). Owing to their high energy storage capacity and durability, EDLCs can be used in various applications such as electric/hybrid vehicles, factory power back ups, cell phones etc. A supercapacitor is a device that stores charge electrostatically through the reversible adsorption of electrolyte ions onto the high surface area electrodes. In general, an EDLC consists of two electrodes with a very high surface area, an electrolyte (aqueous or organic) and a separator which allows the passage of ions through it but not electrons. During the charging process, anions are attracted towards the positive electrode while cations towards the negative electrode. These ions get accumulated on the electrode surfaces. High surface area and porosity are responsible for high charge-discharge rates. The capacitance is assumed to follow that of a parallel plate capacitor:

$$C = \varepsilon_r \varepsilon_0 A/d$$

where, ε_r is the electrolyte dielectric constant, ε_0 is the dielectric constant of vacuum, A is the specific surface area of the electrodes and d is the effective thickness of the double layer.

Energy storage in carbon-based materials such as activated carbon (AC), carbon nanotubes (CNTs) and graphene is through the accumulation of charges at electrode-electrolyte interface. Out of the various carbon nanostructures, graphene exhibits some of the best properties in the electrical double layer capacitor due to important properties like high specific surface area, high electrical conductivity, and mechanical/chemical stability.[20]

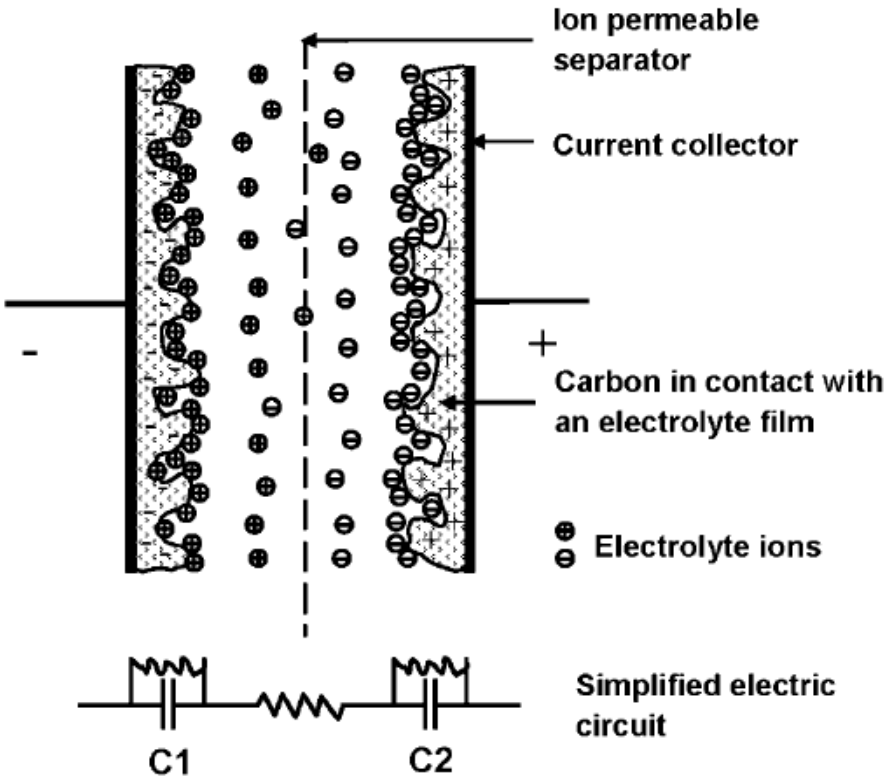

Figure 1.15 *Electrochemical double layer capacitor schematic (Reprinted with permission from Su et al. ChemSusChem 2010, 3, 136, Copyright (2010) Wiley-VCH)*

B. Lithium ion battery:

Li-ion batteries (LIBs) possess the advantaged of high energy density and long cyclability promising energy storage devices for future electric/hybrid vehicles application. The examples for LIB anode are carbon based materials, transition metal oxides and alloying materials like Si. The cathode material generally used is a lithiated metal oxide eg. $LiCoO_2$ (Lithium Cobalt Oxide). LIB cathode and an anode are separated by a microporous glass fiber separator and 1M $LiPF_6$ dissolved in 1:1 wt.% ethylene carbonate (EC) and diethyl carbonate (DEC). The energy storage mechanism in a Li-ion cell occurs by the intercalation and de-intercalation of lithium ions in anodes. Commercially, graphite is the most commonly used LIB anode material. The reversible capacity for graphite electrodes is ~372 mAh g^{-1}. As an alternative, several other carbon based materials are being explored as LIB anode materials due to the reason that the two sides of 2D graphene are available for efficient Li ions adsorption.

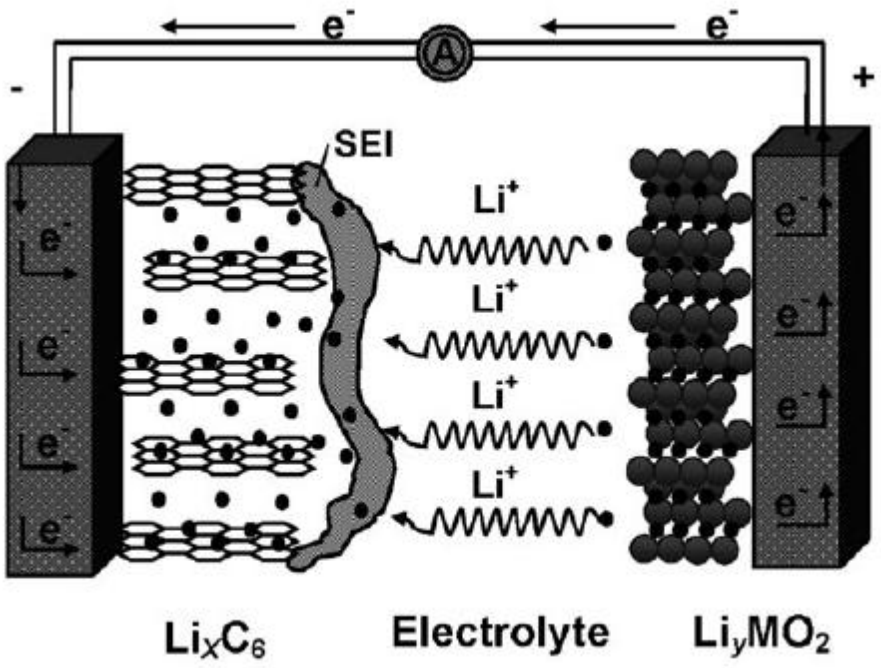

Figure 1.16 *Lithium ion battery schematic (Reprinted with permission from Su et al. ChemSusChem 2010, 3, 136, Copyright (2010) Wiley-VCH)*

C. Dye Sensitized Solar cells:

Dye sensitized solar cells (DSSCs) is a class of low cost solar cells based on the semiconductor thin film technology. The cell consists of a layer of titanium dioxide nanoparticles which is covered by a layer of organic dye. This film is dipped in a liquid electrolyte (I_2/I_3^-) and above it a counter-electrode (cathode) is placed, which is usually platinum based system. The substrates used in these systems are usually Fluorine doped Tin Oxide (FTO) coated glass. The working of DSSCs occurs in the following way: a) photon is absorbed by the dye and an electron is excited and then further pumped into the conduction band of the semiconductor oxide b) The oxide conducts the electrons to the counter-electrode c) The electron lost by the dye is re-obtained from I^-, a redox mediator in the electrolyte, which itself gets oxidized to I^{3-} d) The I^{3-} system moves to the counter electrode and is reconverted into I^- by the catalytic reduction process. Thus the circuit is completed. Usually Platinum based films on FTO have been used as counter-electrodes in DSSCs. This causes the solar

cells to become expensive. In order to replace platinum, extensive research has been carried out to prove that carbon counter-electrodes are effective alternatives. Carbon materials like graphite, carbon cloth, graphene, carbon black etc. show high performance in solar cells.

In addition to this application, highly conducting transparent carbon films have also been used as window electrodes in organic and dye-sensitized solar cells (in place of transparent conducting oxides). Additionally carbon materials like fullerenes have been used as n-type electron acceptor materials in organic/hybrid solar cells.[2]

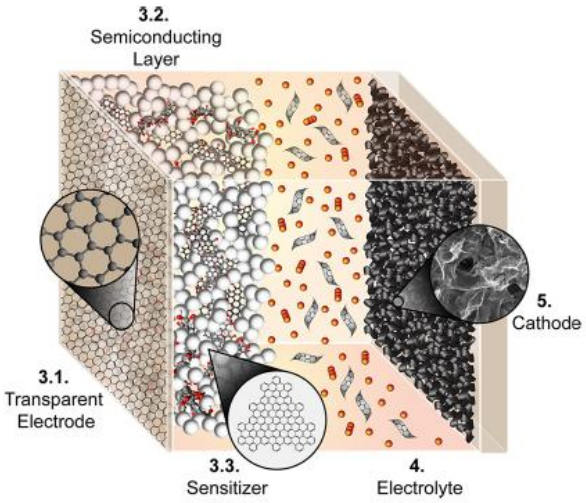

Figure 1.17 *Dye sensitized solar cell schematic (Reprinted with permission from Roy-Mayhew et al. Chem. Rev. 2014, 114, 6323−6348, Copyright (2014) American Chemical Society).*

D. Fuel Cells

Proton Exchange Membrane Fuel Cell (PEMFC) is one of the most important forms of fuel cells that have been applied to various applications globally. The working of PEMFCs involves the use of hydrogen gas (H_2) as the fuel. H_2 gas is catalyzed by platinum at the anode and undergoes oxidation to form protons (H^+). An aqueous acidic solution is used as the electrolyte. The electrons released post the oxidation process flow through an external circuit towards the cathode. The H^+ ions flow in the electrolyte towards the cathode through an ion selective membrane which is selectively permeable to the passage of protons only.[2]

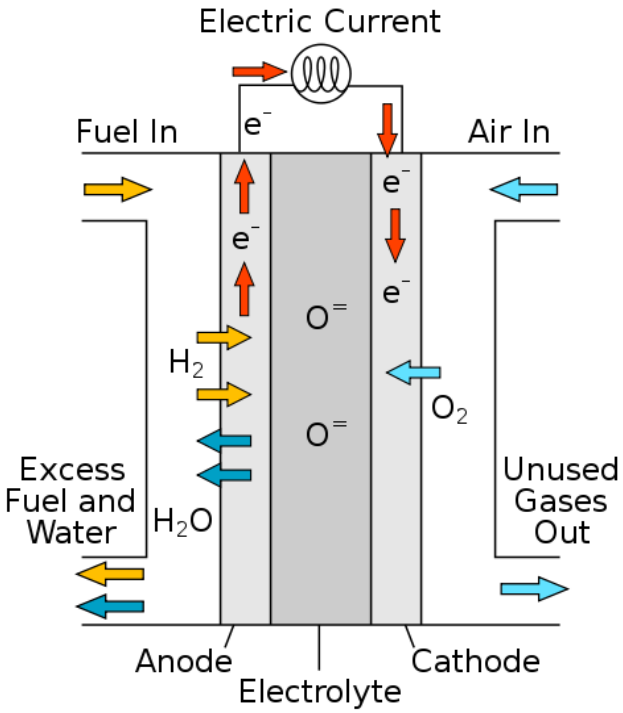

Figure 1.18 *Fuel Cell schematic (Image from Reference 2)*

At the cathode O_2 is pumped in and it gets reduced in presence of the electrons and H^+ ions. This is commonly called the oxygen reduction reaction which is very sluggish in nature and requires a large amount of catalyst for the purpose. Platinum based catalysts are the most widely used cathodic catalysts for the oxygen reduction reaction. The thermodynamic potential of the overall reaction in acidic medium is 1.229 V.

Reaction at the anode: $H_2 \rightarrow 2H^+ + 2e^-$

Reaction at the cathode: $\frac{1}{2} O_2 + 2H^+ + 2e^- \rightarrow H_2O$

In many cases an alkaline electrolyte is used wherein the device is called Anion Exchange Membrane Fuel Cell (AEMFC). The overall reaction in this system is:

$$O_2 + 2H_2O + 4e^- \rightarrow OH^-$$

The thermodynamic potential of this reaction in alkaline medium is 0.4 V. The mechanism of oxygen reduction in alkaline medium is not yet completely understood but a lot of research is being carried out.[21]

Since the use of platinum as a catalyst gives rise to cost issues in the large scale deployment of fuel cells, several alternative materials have been explored. Hetero-atom doped carbon materials and their composites with transition metal nanoparticles are some of the most effective ORR catalysts that have been researched. The dopant heteroatom/transition metal centers give rise to a change in the charge/spin density. This assists in the effective surface adsorption of the gaseous O_2 molecule. Reduction mechanisms take place on the catalytic surface based on a 4 electron or 2 electron transfer process. Each mechanism could be an associative or a dissociative mechanism.

Eg. Electron transfer mechanisms in S-doped Graphene:

	sub-reactions
two-electron transfer pathway	$O_2 + H^+ + e^- \rightarrow *OOH$
path I	$O_2 + H^+ + e^- \rightarrow OOH$
	$OOH + * \rightarrow *OOH$
path II	$O_2 + * \rightarrow *O_2$
	$*O{-}O + H^+ + e^- \rightarrow *O{-}O{-}H$
	$*OOH + H^+ + e^- \rightarrow H_2O_2$
	$O_2 + 2H^+ + e^- \rightarrow H_2O_2$
four-electron transfer pathway	$O_2 + H^+ + e^- \rightarrow *OOH$
path I	$O_2 + H^+ + e^- \rightarrow OOH$
	$OOH + * \rightarrow *OOH$
path II	$O_2 + * \rightarrow *O_2$
	$*O{-}O + H^+ + e^- \rightarrow *O{-}O{-}H$
	$*OOH + H^+ + e^- \rightarrow *O + H_2O$
	$*O + H_2O + H^+ + e^- \rightarrow *OH + H_2O$
	$*OH + H_2O + H^+ + e^- \rightarrow 2H_2O$
	$O_2 + 4H^+ + 4e^- \rightarrow 2H_2O$

Figure 1.19 *Reaction mechanisms for the oxygen reduction reaction on carbon surfaces (Reprinted with permission from Zhang et al. J. Phys. Chem. C, 2014, 118, 3545–3553, Copyright (2014) American Chemical Society).*

Scope and Nature of Present Work

During the course of my PhD work, I have worked on novel/atypical routes to the synthesis of carbon systems and used them for important energy applications like energy generation and storage devices.

In the context of the described background, several interesting problems were worked upon in the same research area on designing carbon materials for specific applications:

1. A novel photochemical route employing UV laser pulses (KrF Excimer, 248 nm) to cleave small aromatic molecules and stitch the generated free radicals into functional nanostructured forms of carbon is introduced. The process differs distinctly from any strategies wherein the aromatic rings are broken in the primary process. It is demonstrated that this pulsed laser-induced photochemical stitching (PLPS) process when applied to routine laboratory solvents Chlorobenzene and o-Dichlorobenzene yields Carbon Nanospheres (CNSs) comprising of graphene-like sheets assembled in onion-like configurations. This room temperature process implemented under normal laboratory conditions is versatile and clearly applicable to the whole family of haloaromatic compounds without and with additions of precursors or other nanomaterials. The applicability for synthesis of metal-oxide based carbon nanocomposites is further brought about.

2. PLPS is used to realize superhydrophobic conducting carbon coatings with broccoli-type hierarchical morphology for use as a metal-free counter electrode in a dye sensitized solar cell. The process involves pulsed excimer laser irradiation of a thin layer of liquid haloaromatic organic solvent o-Dichlorobenzene (DCB). The coating reflects a carbon nanoparticle self-assembled and process-controlled morphology that yields solar to electric power conversion efficiency of 5.1% as opposed to 6.2% obtained with the conventional Pt-based electrode.

3. Development of a highly durable, fuel-tolerant, metal-free electro-catalyst for oxygen reduction reaction (ORR) is essential for robust and cost-effective Anion

Exchange Membrane Fuel Cells (AEMFCs). Work is carried out on the development of a nitrogen-doped (N-doped) hierarchically porous carbon-based efficient ORR electrocatalyst from protein-rich pulses. The process involves 3D silica nanoparticle templating of the pulse flour(s) followed by their double pyrolysis. The detailed experiments are performed on gram flour (derived from chickpeas) without any in situ/ex situ addition of dopants. The N-doped porous carbon thus generated shows remarkable electrocatalytic activity towards ORR in the alkaline medium. The oxygen reduction on this material follows the desired 4-electron transfer mechanism involving the direct reduction pathway. Additionally, the synthesized carbon catalyst also exhibits good electrochemical stability and fuel tolerance. The results are also obtained and compared with the case of soybean flour having higher nitrogen content to highlight the significance of different parameters in the ORR catalyst performance.

4. 3D high surface area n-layer graphene cages are seen to form via self assembly of porous graphene sheets by direct pyrolysis of an oligomer salt tailored for the realization of molecular level activation. The oligomer salt was derived from 4-amino benzoic acid as the monomer by a facile free radical polymerization process. Incorporation of the functional groups (-COONa) eliminate the need for any external activating agents (KOH, $ZnCl_2$ etc.) and also render high degree of sub-nanoscale homogeneity. This oligomer derived carbon (ODC) exhibits efficient performance in non-aqueous charge storage application namely Li-ion hybrid electrochemical capacitor (Li-HEC) owing to its high surface area, 3D interconnectivity and an appropriate pore size distribution. The Li-HEC fabricated with ODC based electrodes delivered a maximum energy density of ~63 W h kg^{-1} with spinel $Li_4Ti_5O_{12}$ as the anode.

References

1. sphweb.bumc.bu.edu
2. en.wikipedia.org
3. HANDBOOK OF CARBON, GRAPHITE, DIAMOND AND FULLERENES: Properties, Processing and Applications by Hugh O. Pierson, Noyes Publications
4. www.telegraph.co.uk
5. www.substech.com
6. J. Wang, S. Kaskel, J. Mater. Chem., 2012, 22, 23710
7. A. Sayari, Y. Yang, Chem. Mater. 2005, 17, 6108-6113
8. H.-J. Liu, X.-M. Wang, W.-J. Cui, Y.-Q. Dou, D.-Y. Zhao, Y.-Y Xia, J. Mater. Chem., 2010, 20, 4223–4230
9. www.scientificamerican.com
10. P. Ajayan, Chem. Rev. 1999, 99, 1787−1799
11. M. Allen, V. Tung, R. Kaner, Chem. Rev. 2010, 110, 132–145
12. www.nanocarbon.cz
13. M. Bacon, S. Bradley, T. Nann, Part. Part. Syst. Charact. 2014, 31, 415–428
14. C. Mattevi, H. Kim, J. Mater. Chem., 2011, 21, 3324–3334
15. www.cnx.org
16. C. Journet, W. Maser, P. Bernier, A. Loiseau, M. Lamyde la Chapelle, S. Lefrant, P. Deniard, R. Lee, J. Fischer, Nature 1997, 388, 756
17. m.iopscience.iop.org
18. A. Funke, F. Zeigler, Biofuels, Bioprod. Bioref. 2010, 4, 160–177
19. www.unf.edu
20. D. Su, R. Schlogl, ChemSusChem 2010, 3, 136
21. Q. Li, R. Cao, J. Cho, G. Wu, Adv. Energy Mater. 2014, 1301415

Chapter 2

Synthesis and Characterization techniques

This chapter briefly describes the experimental procedures and the characterization equipments used in the research that is represented in the thesis. Basic concepts and principles have been discussed herein.

2.1 General Synthesis Techniques

A. High Temperature Pyrolysis

Pyrolysis is a thermo-chemical decomposition of organic material at elevated temperatures in the absence of oxygen (or any halogen). It is an irreversible process that involves the simultaneous change of chemical composition and physical nature. The word is coined from the Greek-derived elements pyro "fire" and lysis "separating". The process is used to a large extent in chemical industry, for example, to produce charcoal, activated carbon, methanol, and other chemicals from wood, to convert ethylene dichloride into vinyl chloride to make Poly Vinyl Chloride (PVC), to produce coke from coal, to convert biomass into syngas and biochar, to turn waste into safely disposable substances, and for transforming medium-weight hydrocarbons from oil into lighter ones like gasoline.

Figure 2.1 *Split tube furnace*

This is one of the most widely used methods for the synthesis of carbon. For many years now this method has been widely extensively applied for the synthesis of activated carbon and porous materials from natural or manmade by-products. The process involves treatment of samples to very high temperature (~1000^{o}C) for certain time in a split tube furnace (Figure 2.1) under continuous flow of argon gas. At high temperature the materials burn and form carbonized products with some degree of

graphitization. This method is mostly used to synthesize valuable products from waste materials, organic molecules etc.

B. Pulsed Laser Synthesis Method

Laser irradiation is a novel and unique technique to synthesize nanostructures from liquid/solid precursors. In this method high energy laser pulses are allowed to interact with the precursor samples present either in solid or liquid medium for certain time period. It is a very unique method for the synthesis of nanoparticles because of heat or photochemical mechanisms which result in molecular level changes. Several transient reactions can be manipulated with the laser irradiation by adding some external reagents which can construct totally new compounds after initial photochemical mechanisms.

Figure 2.2 *Pulsed UV Laser (KrF excimer)*

2.2 Characterization techniques

A. UV Visible Absorption Spectroscopy

UV-Vis spectroscopy is a form of electronic spectroscopy. Reflected and transmitted light from the sample is measured and information about the electronic transitions is possible through the interpretation of the absorption signals.[1]

The perceived colour of the chemicals involved is affected by the absorption or reflectance in the visible region. In this region of the electromagnetic spectrum, molecules undergo electronic transitions. This spectroscopy is complementary to fluorescence spectroscopy. Fluorescence deals with transitions from the excited state to the ground state and absorption measures the reverse transitions. When the incident photon energy exceeds the band gap energy of the material in semiconductors, absorption occurs and signal is recorded by the spectrometer whereas in metals resonant absorption takes place as the surface free electrons vibrate coherently with the incident frequency.

This spectrometer can operate in two modes (i) transmission and (ii) reflection mode. In transmission mode usually thin films and colloidal NPs, well-dispersed in solvent are used. While in reflectance mode, opaque thin films and NPs which are not dispersible in solvents is analyzed.

In UV-Visible absorption spectroscopy, light from a source is transmitted through a monochromator to obtain the light of desired wavelength. The emerging light is then passed through the sample under study and then into a detector (Figure 2.3). Typically, a chopper splits the light from the source two equivalent beams; one beam passes through the sample and the other through the reference. The photodiode detector alternates between measuring the sample beam and the reference beam. In many cases the double beam instruments have two detectors, where the sample and reference beams are measured at the same time. Sometimes though in some instruments, the two beams are recombined in a single optical path via the use chopper which blocks one beam at a time.

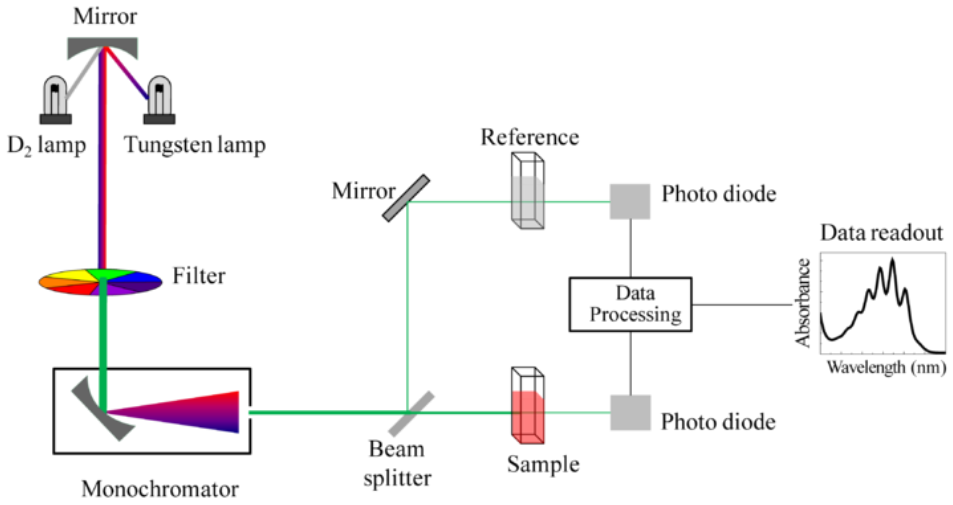

Figure 2.3 *UV Visible spectrophotometer (Ref: en.wikipedia.org)*

B. X-ray Diffraction

X-ray diffraction (XRD) is a widely used, quick, non-destructive technique helpful in determination and identification of structure in crystalline materials. The technique has been conventionally applied for phase identification and study. A large variety of materials such as metals, minerals, catalyst and inorganic compounds can be characterized by XRD. It is one of the most applicable and efficient general techniques of science.[2-4]

Figure 2.4 shows the schematics of X-ray diffractometer. Diffraction in general occurs only when the wavelength of the wave motion is of the same order of magnitude as the repeat distance between scattering centers. This condition of diffraction is nothing but Bragg's law and is given as,

$n\lambda = 2d\sin\Theta$

where,

d = inter-planer spacing, Θ = diffraction angle, λ = wavelength of X-ray, n = order of diffraction

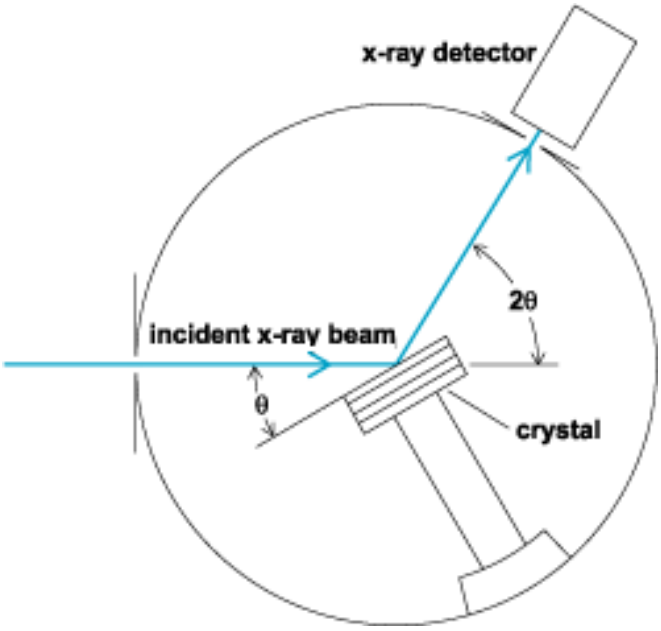

Figure 2.4 *XRD machine schematic (Ref: www.ehs.columbia.edu)*

In powder XRD method the crystal to be examined is reduced to a fine powder and placed in a beam of a monochromatic X-rays. Each particle of the powder is the tiny crystal, or assemblage of smaller crystals, oriented at random with respect to incident beam. Some of the crystals will be correctly oriented so that their (100) planes, for example, can reflect the incident beam. Other crystals will be correctly oriented for (110) reflections and so on. The result is that every set of lattice planes will be capable of reflection. This is the principle of a powder diffractometer. Ideally, according to Bragg's law, for the particular d value, the constructive interference of X-rays should occur only at particular Θ value i.e Bragg's angle and for all other angles there should be destructive interference and intensity of diffracted beam will be minimum there.

Identification of Phases

From the d-spacings, phases can be identified in a film using the standard JCPDS powder diffraction file and the reflections can be indexed with Miller indices. However, if the size of the diffracting tiny crystal is small, there is no complete destructive interference at Θ±dΘ, which broadens the peak corresponding to diffracted beam in proportion to the size of the tiny crystal. This can be used to calculate the particle size.

The relation for the same is given by Debye Scherrer formula as,

$$t = \frac{0.9\lambda}{\beta cos\theta}$$

where, t = particle size, Θ = diffraction angle, λ = wavelength of X-rays and β line broadening at Full Width at Half Maxima (FWHM). Further, the powder diffractometer can also be used for X-ray diffraction from thin films. Epitaxial or polycrystalline (may or may not be oriented) thin films can be considered as single crystal or powder (crystals or assembly of crystals spread on substrate) respectively. Hence, a typical epitaxial or oriented film may not show all corresponding reflections and show only few reflections for example say, a c-axis oriented film will show only (hkl) for which h and k indices are zero and l is non zero. However, these hidden peaks can be detected by small angle X-ray diffraction technique.

C. Photoluminescence

Spontaneous emission of light on optical excitation of a material is called photoluminescence (PL). In order to probe the sample's discrete electronic states accurately, it is required to scan the required excitation energy and intensity appropriately. When a light of sufficient energy is incident on a material, electronic transitions arise due to absorption of photons within the allowed energy states of the material. Eventually, these excitations relax and the electrons return to the ground state. If radiative relaxation occurs, the emitted light is called PL. This light can be collected and analyzed to yield a wealth of information about the photo-excited material. The PL spectrum provides information on transition energies, which can be further used to determine electronic energy levels, defects and impurity states in the sample. The PL intensity also gives a measure of the relative rates of radiative and non-radiative recombination.

PL can be categorized into two: fluorescence and phosphorescence, depending upon the electronic configuration of the excited state and the emission pathway. Fluorescence is the property of some atoms and molecules to absorb light at a particular wavelength and to subsequently emit light of longer wavelength after a brief interval, which is characterized as the fluorescence lifetime. The process of

phosphorescence occurs in a manner similar to fluorescence, but with a much longer excited state lifetime. Hence Phosphorescence is a delayed emission process.

PL is a simple, versatile, and non-destructive measurement technique. Two essential features describe the PL signal: peak energy and intensity. The excitation energy and optical intensity can be carefully selected in order to yield additional accurate information on the energy levels available to electrons in the material. The PL signal often depends on the density of photo-excited electrons and the intensity of the incident beam. The intensity of the PL signal depends on the rate of radiative and nonradiative events, which depends in turn on the density of nonradiative interface. The bottom picture of Figure 2.5 shows of photograph of the photoluminescence set-up.

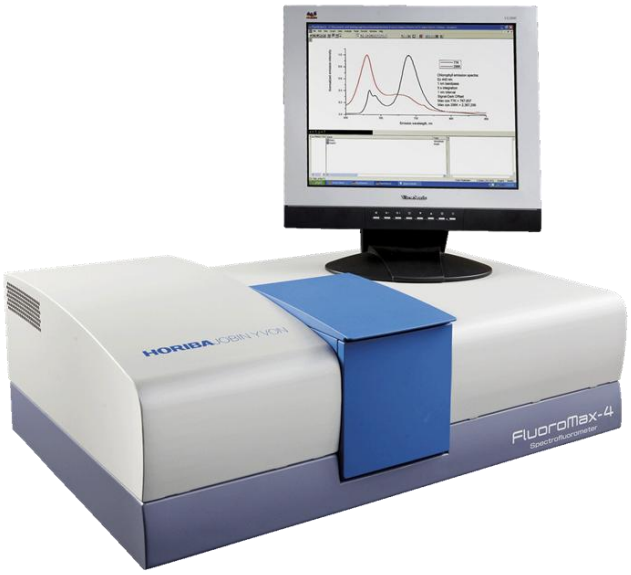

Figure 2.5 *PL spectrophotometer (Ref: www.fi.tartu.ee)*

D. X-ray Photoelectron Spectroscopy

X-ray photoelectron Spectroscopy (XPS) probes the binding energies of core electrons in an atom. Although such electrons play little part in chemical bonding, different chemical environments can induce small changes in their binding energies; this is because the formation of bonds changes the distribution of electrons in the

system and hence by modifying the nuclear shielding, produces changes in the effective nuclear charge of the bound atoms. XPS is also rarely called as electron spectroscopy for chemical analysis (ESCA). Since only the photoelectrons from the atoms near the surface escape the information obtained is typically from the surface layer of 2-5 nm with a typical sampling area of 1 cm^2. The actual depth varies with the materials and electron energy. This technique mainly gives information about the elemental composition of the surface of the materials and the information about the chemical state of elements. Usually Al and Mg source is used for producing X-rays to excite photoelectrons from the core levels of atoms in a specimen. When an atom or molecule is subjected to higher energy radiations, photons in the radiations colloid with and eject electrons from atoms, leaving behind ions. Ejected electrons depart with different velocities and photoelectron spectroscopy measures the velocity distribution of the released electrons. Each electron is held in place by nucleus with a characteristic binding energy.

The energy of the photon is imparted to the electron and, if this energy is greater than the B.E., the electron will leave the atom and carry with it an excess energy – thus it will have certain K.E. (and velocity). Clearly the total energy must conserve:

$h\upsilon$ = binding energy + Work Function + kinetic energy

Binding Energy = $h\upsilon$ – Kinetic Energy

Since the excitation energy is known and the kinetic energy is measured, the binding energies of electrons in the atom under examination can be determined. Main components of XPS are (i) X-ray source, (ii) Sample holder, (iii) electron energy analyzer. The (ii) and (iii) component must be in UHV. The X-ray source is a simple X-ray tube with double anodes (typically Al and Mg) incident radiation energy can be switched from one to the other. In both, XPS, the kinetic energy of the ejected electrons is measured using a hemispherical analyzer.

Monochromatic X-ray or UV radiation falls on the sample and ejected electrons pass between a pair of electrically charged hemispherical plates which act as an energy filter, allowing electrons of only a particular kinetic energy to pass through – the pass energy, Epass. The resulting electron current, measured by an electron multiplier, indicates the number of electrons ejected from the surface with that kinetic energy.

Epass can be systematically varied by changing the retarding voltage (VR) applied to the analyzer. XPS measurements of different samples were carried out on a VG MicroTech ESCA 3000 instrument at Center for Materials Characterizations (CMC), National Chemical Laboratory, Pune. The core level binding energies (BE) were corrected with the carbon binding energy of 285 eV.

.

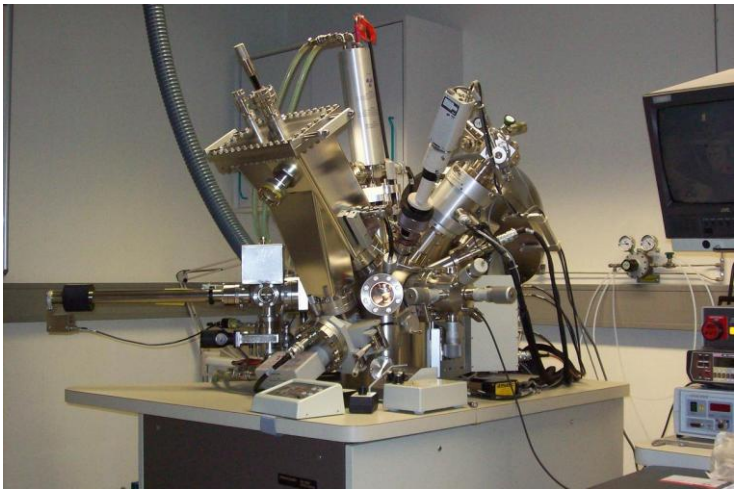

Figure 2.6 *XPS instrument (Ref: www.ine.kit.edu)*

E. Raman Spectroscopy

Raman spectroscopy is a powerful tool to analyze structural/morphological properties of solid oxides at a local or near surface level due to the strong sensitivity of the phonon characteristics to the crystalline nature of the materials. In Raman spectrometer, when a beam of visible light is passed through the sample a small amount of the radiation energy is scattered, the scattering persisting even if all other extraneous matter are rigorously excluded from the substance. If a monochromatic radiation is used and if the scattered energy is almost same as the incident frequency then it is called as Rayleigh scattering, however in addition, if some discrete frequencies above and below that of the incident beam are observed to scatter, it is referred to as Raman scattering. [5-6]

According to quantum theory of radiation, when photons having energy 'hυ' undergo collisions with molecules, if the collision is perfectly elastic, they will be deflected unchanged. A detector placed to collect energy at right angles to an incident beam will thus receive photons of energy 'hυ', i.e. radiation of frequency 'υ'. However, it may happen that energy is exchanged between photon and a molecule during the collision (such collisions are called inelastic). The molecule can gain or lose amounts of energy only in accordance with the quantum laws; i.e. its energy change, ΔE (joules) must be the difference in energy between two of its allowed states and it must represent a change in the vibrational and/or rotational energy of the molecule. If the molecule gains energy ΔE, the photon will be scattered with the energy hυ- ΔE and the equivalent radiation will have a frequency υ- ΔE/h. Conversely, if the molecule loses energy ΔE, the scattered frequency will be υ+ ΔE/h. Radiations scattered with a frequency lower than that of the incident beam is referred to as Stokes' radiation, while that at higher frequency is called anti-stokes' radiation. Stokes' radiation is accompanied by an increases in molecular energy, which is very common (subject to certain selection rules) while anti-stokes' radiation involves a decrease in molecular energy (which can only occur when the molecule is originally in an excited vibrational/rotational state), stokes' radiation is generally more intense than anti-Stokes' radiation.

Figure 2.7 shows the schematic of Raman spectrometer. Raman Spectrometer consists of Laser beam (very narrow, monochromatic, coherent and powerful) which when passed through the cell, usually a narrow glass or quartz tube filled with the sample, light get scattered sideways from the sample, which is collected by a lens and passed into a grating monochromator. The signal is measured by a sensitive PMT and after amplification; it is usually processed by a computer which plots the Raman spectrum.

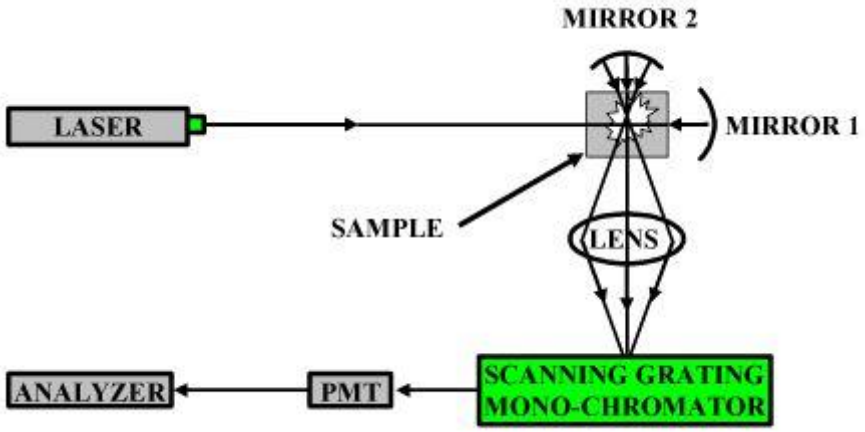

Figure 2.7 *of Raman Spectroscopy (Ref: wasatchphotonics.com)*

F. Fourier Transform Infrared Spectroscopy

Every compound having covalent bonds absorbs various frequencies of electromagnetic radiation in the infrared region of electromagnetic spectrum. The region lies in between visible (longer and microwaves wavelengths. Similar to other spectroscopy techniques, on absorption of the radiation, molecules are excited to a higher energy state. This absorption process corresponds to energy changes in the order of 8 to 40 kJ/mol. As there is a very important requirement for a molecule to show IR spectrum, all the bonds in the molecule are not IR active. Only those bonds, which have a dipole moment that changes as a function of time are capable of absorbing IR radiation. Symmetric/Homonuclear diatomic molecules such as H_2, O_2, Cl_2 etc., do not absorb IR radiation as do not have permanent dipole moment. On the other hand heteronuclear diatomic molecules such as CO, HCl, NO do possess permanent dipole moment and hence are IR active. IR spectra occur in the frequency range of 500 - 4000 cm-1. Two types of IR spectrometers are in common use i) Dispersive and ii) Fourier transform (FT) infrared spectrometer. These instruments give nearly similar spectra for a sample under study of 4000 - 400 cm-1. only the FTIR spectrometers provide the spectrum much more quickly than the dispersive IR spectrometer. Schematic of FTIR spectrometer is shown in Figure 2.8. [1]

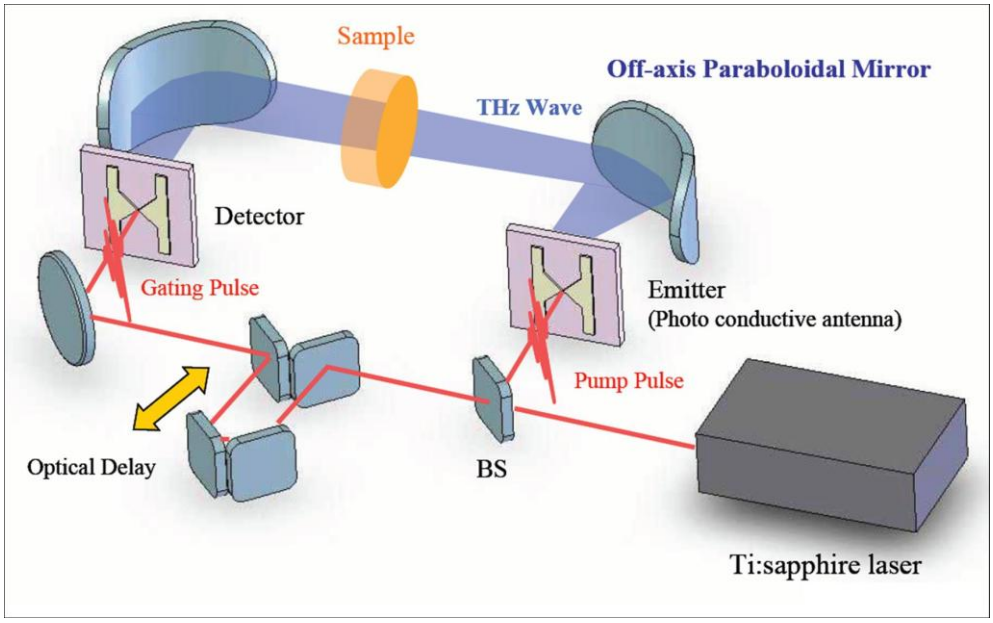

Figure 2.8 *FTIR spectrophotometer schematic (Ref: www.riken.jp)*

G. Transmission Electron Microscopy (TEM)

Transmission electron microscopy (TEM) is an imaging technique whereby a beam of electrons is focused onto a specimen causing an enlarged version to appear on a fluorescent screen or a layer of photographic film, or to be detected by a CCD camera. TEM operates on the same basic principles as the light microscope but uses electrons instead of light. The line diagram of a typical TEM column is shown in Fig. 2.9. The column consists of a source of electrons, electrodes for electron acceleration, electromagnetic focusing and deflecting lenses and the electron detection system such as a CCD array. By using electron energy of several hundred kilovolts the de Broglie wavelength associated with the electron can be reduced to a small fraction of nanometer and hence atomic resolution imaging becomes feasible. [7-9]

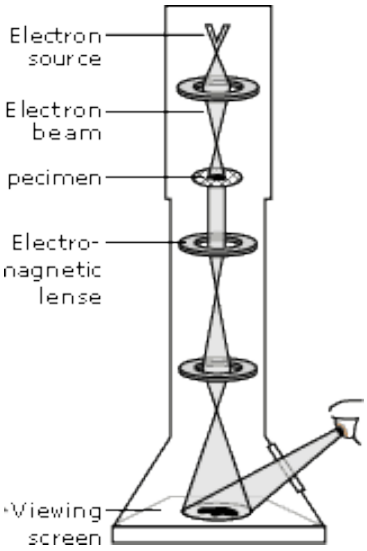

Figure 2.9 *Schematic of Transmission Electron Microscopy (Ref: www.nobelprize.org)*

Virtually, TEM is useful for determining size, shape and arrangement of the particles which make up the specimen. Moreover, it is highly useful for the determination of the lattice planes and the detection of atomic-scale defects localized in areas of few nanometers in diameter with the help of selected area electron diffraction (SAED) technique. The d- spacing between lattice planes of crystalline materials can be calculated from a SAED pattern using the relationship:

$dr = \lambda L$

where, L is the distance between the specimen and the photographic plate, λL is known as the camera constant and r is the radius of diffracted rings. It is easy to measure r directly from the photographic plate, and λL can be established from the instrument by calibrating it with a standard material (usually Ag), and hence one can easily get d values. Since, each d value corresponds to a specific lattice plane for a specific crystal structure; description of the crystal structure of a crystalline specimen can be obtained from SAED pattern. In some cases SAED pattern is more helpful as compared to XRD, due to the limited detection limit of XRD instrument. Also, the XRD generally gives global information.

H. Scanning Electron Microscopy

It uses a beam of electrons focused to a diameter spot of approximately 1nm in diameter on the surface of the specimen and scanned back and forth across the surface. The surface topography of a specimen is revealed either by the reflected (backscattered) electrons generated or by electrons ejected from the specimen as the incident electrons decelerate secondary electrons. A visual image, corresponding to the signal produced by the interaction between the beam spot and the specimen at each point along each scan line, is simultaneously built up on the face of a cathode ray tube similar to the way that a television picture is generated. The best spatial resolution currently achieved is of the order of 1nm.

The scanning electron microscope (SEM) is a very useful instrument to get information about topography, morphology and composition information of materials. A typical schematic of a SEM is shown in Fig. 2.10. It is a type of electron microscope capable of producing high resolution images of a sample surface. Due to the manner in which the image is created, SEM images have a characteristic three-dimensional appearance and are useful for judging the surface morphology of the sample. The SEM has an ability to image a comparatively large area of a specimen and also to image bulk materials. Topology of the powder samples in the present study was carried out using a Leica Stereoscan – 440 scanning electron microscope.

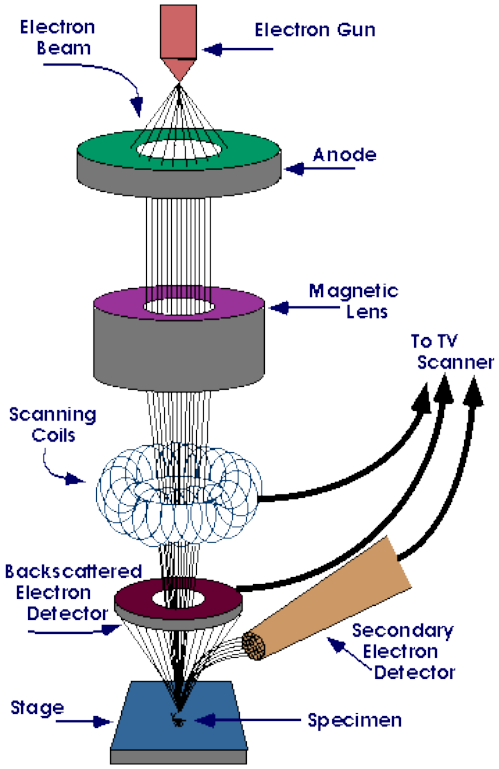

Figure 2.10 *Schematic of Scanning Electron Microscopy (Ref: www.purdue.edu)*

I. Cyclic Voltammetry and Charge Discharge measurements

Cyclic voltammetry (CV) is the most widely employed tool for obtaining qualitative information about electrochemical reactions. It is known to give information about the redox potentials of electrochemically active species. CV is a potentio-dynamic electrochemical measurement. In a cyclic voltammetry experiment, the potential of working electrode is ramped linearly vs. time. CV is in fact an increment to linear sweep voltammetry which generally ends when it reaches a set potential. In this measurement, the current at the working electrode is plotted versus the applied voltage to give the cyclic voltammogram trace. The voltage is swept between two values (V1 and V2) at a fixed scan rate (mV/s) in a cycle. When the voltage reaches V2 the scan is reversed and the voltage is swept back to V1. When the scan is reversed, the equilibrium position is reset.

Galvanostatic Charge Discharge for capacitance and stability measurement Cyclic charge discharge is a standard galvanostatic technique that is used to test the performance and cycle-life of supercapacitors and batteries. A repetitive loop of charging and discharging is called a cycle. Charge and discharge analysis are conducted at a constant current rate until a set value of potential is attained. Generally a potential window of 0-1 V is used for an aqueous electrolyte. The potential window varies with different organic solvents. The capacitance and stability of the device and material is calculated from the charge-discharge curve. Typical CV and charge discharge curves are shown in Figure 2.1 a and b respectively.

J. Rotating disk electrode measurement (RDE)

A rotating disk electrode is a hydrodynamic working electrode which is generally used in a three-electrode setup. During the experiment, this electrode controlled undergoes rotational movement which causes a flux or rapid movement in the electrolyte or the analyte. A continous flow of the analyte on the working electrode is obtained. A RDE is used for investigating reaction mechanisms of redox reactions. The rotation of the RDE is measured in terms of angular velocity. Different electrochemical measurements are carried out using this setup. The RDE is genereally made up of a noble metal or glassy carbon.

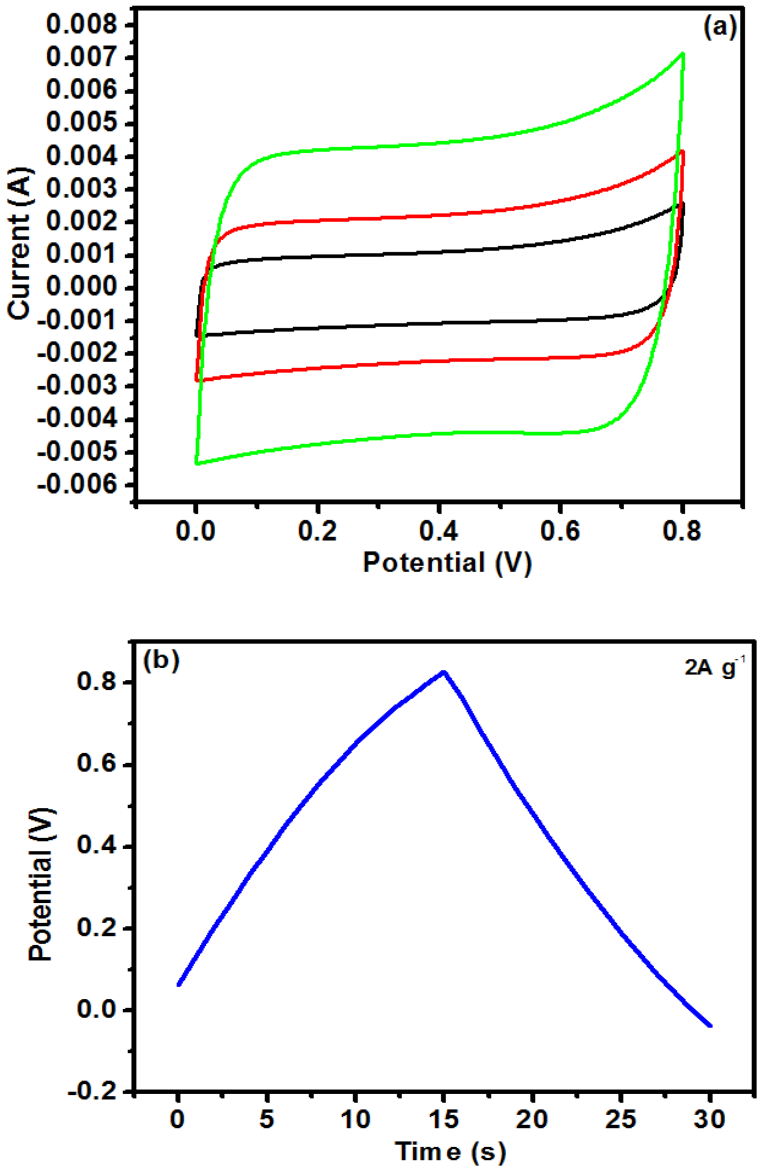

Figure 2.11 *a) CV curves for electrochemical double layer capacitance in carbon material b) charge discharge curve for carbon material.*

References

1. C. N. Banwell, E. M. McCash, A Book: Fundamentals of Molecular Spectroscopy, 4th Edition.
2. M. J. Buerger, “X-ray Crystallography”, Wiley, New York, (1942)
3. H. P. Klug and L. E. Alexander, “X-ray Diffraction Procedures”, Wiley, New York, (1954).
4. B. D. Cullity, “Elements of X-ray Diffraction”, Addison Wesley, Massachusetts (1956)
5. D. A. Long, Raman Scattering, Mcgraw Hill Book Company, New York, 1977
6. A. C. Ferrari and J. Robertson, Phys. Rev. B, 2000, 61, 14095.
7. J. Morgan, L. J Allen, A Hashimoto, M. Takeguch, K. Mitsuishi, M.Shimojo, Ultramicroscopy, 2011, 111, 877. 10
8. Williams, D.B., Carter, C.B., 2009. Transmission Electron Microscopy- A Textbook for Materials Science. Springer.
9. Y. Hernandez, V. Nicolosi, M. Lotya, F. M. Blighe, Z. Sun, S. De, I. T. McGovern, B. Holland M. Byrne Y. K. Gun'Ko J. J. Boland P. Niraj G. Duesberg S. Krishnamurthy, R. Goodhue, J. Hutchison, V. Scardaci, A. C. Ferrari and J. N. Coleman, Nat. Nanotechnol., 2008, 3, 563.

Chapter 3

From small aromatic molecules to functional nanostructured carbon by pulsed laser-induced photochemical stitching

A novel route employing UV laser pulses (KrF Excimer, 248 nm) to cleave small aromatic molecules and stitch the generated free radicals into functional nanostructured forms of carbon is introduced. The process differs distinctly from any strategies wherein the aromatic rings are broken in the primary process. It is demonstrated that this pulsed laser-induced photochemical stitching (PLPS) process when applied to routine laboratory solvents (or toxic chemical wastes when discarded) Chlorobenzene and o-Dichlorobenzene yields Carbon Nanospheres (CNSs) comprising of graphene-like sheets assembled in onion-like configurations. This room temperature process implemented under normal laboratory conditions is versatile and clearly applicable to the whole family of haloaromatic compounds without and with additions of precursors or other nanomaterials. We further bring out its applicability for synthesis of metal-oxide based carbon nanocomposites.

3.1 Introduction

Carbon is the most abundant naturally occurring element exhibiting an amazing variety of molecular and structural formulations which find numerous applications in material technology. The principle crystalline forms of pure carbon are Diamond and Graphite. Carbon also exists in amorphous forms like a-C, a-C:H and tetrahedral amorphous carbon (ta:C). 'Carbon nanomaterials' is a widely explored research area in recent times owing to the diverse new applications of these novel materials attributable to their interesting mechanical, electrical, catalytic and optical properties. A variety of intriguing nanostructures of carbon such as carbon nanotubes (CNTs), nanocrystalline graphite, graphene, fullerenes, nano-spheres, nano-onions, and nano-diamonds have been synthesized by established techniques of carbon synthesis such as carbonization of organic/polymeric precursors,[1,2] chemical/autoclave synthesis from small halogenated aromatic molecules,[3-9] chemical vapor deposition,[10-12] excimer laser ablation of graphitic targets,[13,14] sputtering/plasma methods,[15] arc discharge methods[16] etc. Sphere-like nanoparticles of carbon or carbon nano-spheres (CNSs) have also been synthesized by several methods ranging from catalytic CVD,[17-19] hydrothermal methods[20] and template based chemical synthesis.[21] However, to the best of our knowledge, an efficient, low temperature and high purity (without by-products) synthesis process is yet to be established in the context of CNS preparation.[17] Synthesis of unique and functional carbon nanoforms at low temperature and mild conditions is indeed a real challenge. A pulsed laser represents an interesting source of controlled optical energy transfer to any chemical system at room temperature and hence can be envisaged to offer new solutions in this context. Herein, we report a novel method of nano-carbon synthesis by laser photochemistry; a process that involves pulsed UV laser irradiation of liquid halobenzenes, (chlorobenzene (CB) and o-dichlorobenzene (DCB)) resulting in the photo-cleavage of the carbon-halogen bond, generating a large number of free radicals and their stitching into nanospheres of carbon. We term this as the "Pulsed Laser-induced Photochemical Stitching (PLPS)" technique. In terms of the basic nature of the primary process, this is to be clearly distinguished from laser induced direct photochemical breaking of C-C bonds of the aromatic rings or laser induced indirect thermal breaking of the C-C bonds, which can also lead to different forms of carbon.

We show clear evidence that in our case primarily we get layered (onion-like) intermediates formed by the stitching process which can lead to other forms through secondary absorption.

3.2 Experimental

3.2.1 Materials & Equipment

High purity (GR grade) routine organic solvents Chlorobenzene (CB) and o-Dichlorobenzene (DCB) were obtained from Merck Chemicals and were used as received. A 248 nm KrF excimer laser (Lambda Physic – Germany) with a maximum average power of 40 watts (pulse energy = 150 mJ) and a pulse-width of 20 ns was used in the irradiation process.

3.2.2 The Process

50 ml of transparent liquid DCB was irradiated by laser pulse train (10 Hz) for 10 minutes in a quartz beaker under constant stirring (Figure 3.1, schematic). The solution gradually turned black due to the formation of optically absorbing solid state material (Figure 3.2, photo). The black solution formed was then filtered through 0.2 µm (pore size) Polytetrafluoroethylene (PTFE) membrane. A black carbonaceous solid was obtained, which was thoroughly characterized. Similarly, 50 ml of liquid CB was irradiated for 30 minutes. Interestingly, CB was noted to take a longer time for the product formation, presumably due to the availability of a single reaction site (C-Cl bond) in comparison with the two sites on DCB, as discussed later in the context of the mechanism.

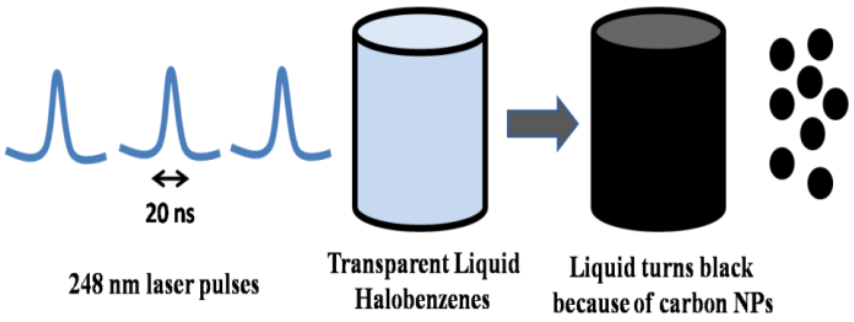

Figure 3.1 *Figurative depiction of the experimental process*

Figure 3.2 *Actual image of liquid before and after irradiation*

3.2.3 Characterization

Scanning electron microscopy with Energy-dispersive X-ray spectroscopy (EDX) (FEI Quanta 200 3D) was used for the determination of morphology and elemental composition. X-ray photoelectron spectroscopy (XPS) (ESCA-3000, VG Scientific Ltd. UK, with a 9 channeltron CLAM4 analyzer under vacuum better than $1* 10^{-8}$ Torr, Al Ka radiation (1486.6 eV) and a constant pass energy of 50 eV) was employed to study the chemical state of carbon in the materials respectively. X-ray Diffraction (XRD, Philips X'Pert PRO) and Raman spectroscopy (a confocal micro-Raman spectrometer LabRAM ARAMIS Horiba JobinYvon, with laser excitation wavelength of 532 nm) were also used to examine the characteristics of the carbonaceous compounds. Thermogravimetric analysis (TGA) was performed to determine the thermal stability. We also obtained images of the graphitic CNSs by techniques of Field Emission Scanning Electron Microscopy (FESEM, Hitachi S-4200) and High Resolution-Transmission Electron Microscopy (HR-TEM, FEI Tecnai 300). Conductivity measurement was carried out on a pellet by a two probe method. The surface area of carbon was obtained from BET surface area measurements (Quantachrome Quadrasorb automatic volumetric instrument).

3.3 Results and Discussion

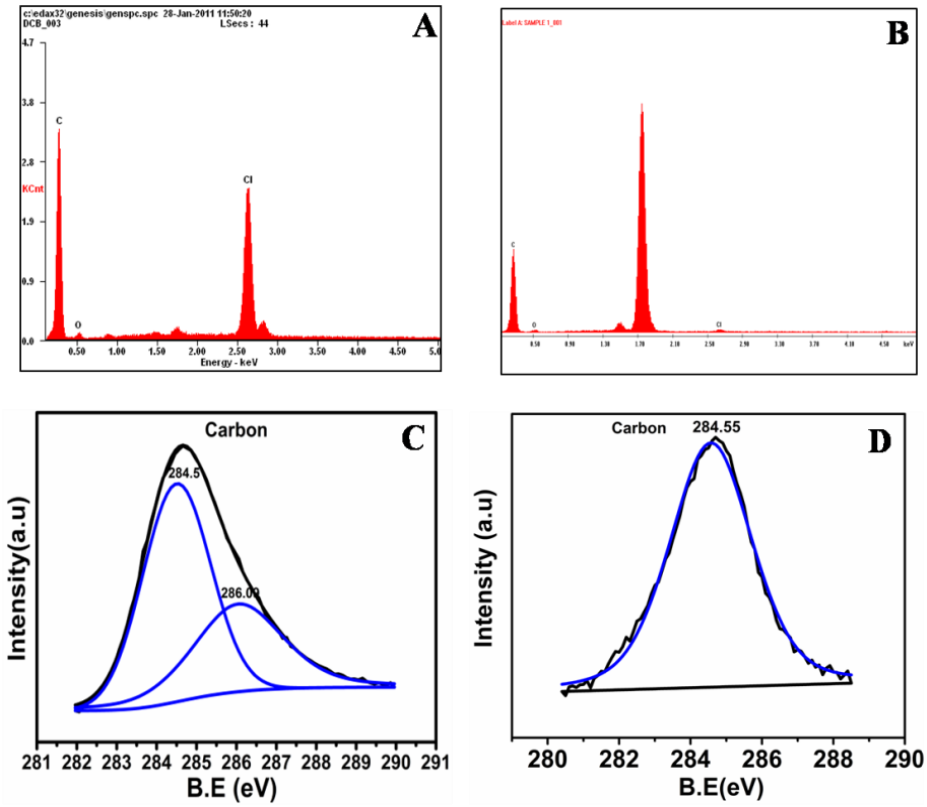

Figure 3.3 (A) *EDAX analysis of carbon obtained from DCB,* ***(B)*** *EDAX of carbon from CB,* ***(C)*** *XPS analysis of carbon from DCB,* ***(D)*** *XPS of carbon from CB*

The composition and elemental bonding state of the carbonaceous materials obtained from CB and DCB were investigated using Energy-dispersive Analysis of X-rays (EDAX) and X-ray photoelectron spectroscopy (XPS) techniques, respectively (Figure 3.3). The solid material acquired from DCB was seen to consist mostly of carbon (93-95 %) with some residual chlorine groups from the starting material (Cl- 2-3 at. %) and oxygenated carbons (O-2-3 at %) (Figure 3.3A). The carbon from CB was observed to contain lesser amount of residual -Cl groups (Cl- 0.25 at %) (Figure 3.3B). This can be attributed to the single reactive C-Cl site on each molecule of CB as compared to DCB. The extra tallest peak in the same figure is attributed to the Si substrate, which shows up when the film thickness is small. XPS analysis brings out that carbon from DCB exists in the usual sp^2 C=C form as confirmed by the fitted C 1s peak at 284.5 eV. The peak at 286.09 may be attributed to the residual C-Cl bonds

in the compound (Figure 3.3C). Further, the XPS of carbon compound obtained from CB confirms the presence of the sp^2 carbon (Figure 3.3D).

EDAX Data (Table 3.1):

Composition of Carbon from CB:

Element	Wt %	At %
C	94.17	95.86
Cl	0.75	0.26
O	5.08	3.88
Total	100	100

Composition of Carbon from DCB:

Element	Wt %	At %
C	89.53	95.25
Cl	8.24	2.97
O	2.23	1.78
Total	100	100

These carbonaceous materials obtained from both CB and DCB were characterized by x-ray diffraction (XRD). In each case, one main very broad peak attributable to the (002) plane of graphite at $2\theta = 24.45^o$ was observed along with a small hump at $2\theta = 43.47^o$ corresponding to (100) plane (Figure 3.4A) (JCPDS-ICDD Card No.41–1487). The XRD data reveals the disordered graphitic nature of the material. The greater the deviation from the ideal graphitic (002) peak position at 26.6^o the greater is the disordered nature of the system. The broad peaks indicate that there is no long range order and point to the presence of graphitic nanoparticles in the system.

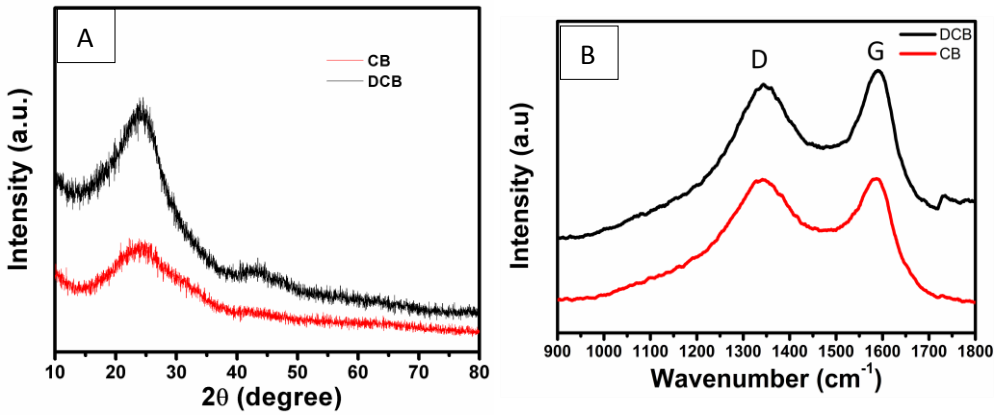

Figure 3.4 (A) *XRD of carbon (CB and DCB case)* ***(B)*** *Raman Spectroscopy studies on Carbon from CB and DCB (D and G bands labelled inset)*

In both the cases Raman spectroscopy (Figure 3.4B.) exhibits the usual 'G Band' at 1590 cm^{-}attributed to the E_{2g} symmetry mode of the sp^2 carbon in carbon compounds. A 'D Band' also exists at 1345 cm^{-1}. The D band arises due to hexagonal ring systems in the compound and is a forbidden transition. It becomes an allowed transition due to defects in the system. In crystalline compounds like pure graphite, there are very few defects and hence the D band is absent. However with decreasing particle size and increasing defect concentration, the intensity of the D band increases. An intense D band also indicates a larger presence of hexagonal ring systems. In pure amorphous carbon an intense D band does not exist. A shoulder to the G band appears in such systems. It is also clear that decreasing particle size and increasing defects contribute to a greater I_D/I_G ratio. Since the carbon compounds obtained in our case show a high I_D/I_G ratio (1 in the case of CB and 0.95 in the case of DCB) presence of nanoparticles is clearly suggested, which is evidenced later by other techniques.[17, 22]

HRTEM images (Figure 3.5 A-F) clearly demonstrate the presence of CNSs obtained from both the starting materials. CNSs are known to possess a strong tendency for agglomeration.[17, 23] This happens because most of the CNSs are not completely closed spheres. They possess open edges and the outer graphitic layer encloses more such spherical particles. CNSs with sizes ranging from 30-40 nm to about 200 nm have been observed in this process. Presence of a large number of hollow CNSs was also detected (Fig. 4A, 4F). In the laser synthesis of CNSs in our case, the nanospheres assemble into micron sized porous flakes which is quite evident from the SEM images (Figure 3.6 A-D).

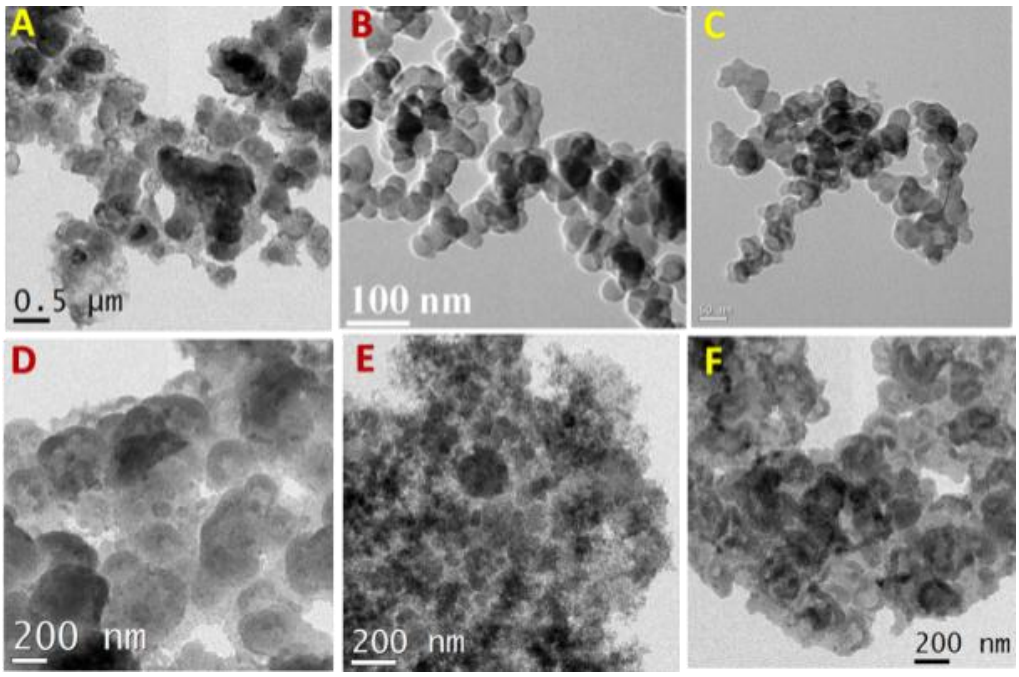

Figure 3.5 (A-D) *TEM images of CNSs obtained by irradiation of DCB* ***(E-F)*** *TEM images of CNSs obtained similarly from CB*

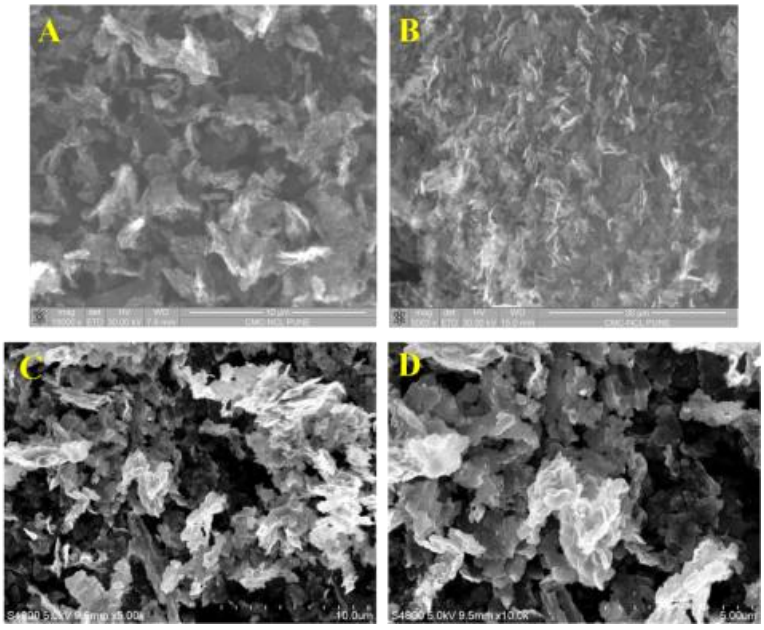

Figure 3.6 (A-B) *SEM images of porous flake like structures formed by the assembly of CNSs obtained from DCB* ***(C-D)*** *FE-SEM images of similar structures from CB*

The BET surface area measurement yielded the surface area for CNSs synthesized from CB and DCB to be 38 m^2 /g and 108 m^2 /g respectively. The exact reason behind the difference in the surface area of carbon acquired from these nominally similar precursors remains unclear, although the extra chlorine in DCB may have a role to play in the much larger surface area obtained in that case.

We made frequency dependent conductivity measurements on pellets made from the carbon synthesized by using CB and DCB to explore whether the carbon formed is electrically functional and therefore potentially useful for several applications. We expected it to have good conductivity in view of the fact that due to the suggested ring-stitching nature discussed in more details below, the synthesized carbon is configured as an assembly of graphene like sheets. The results of conductivity measurements shown in Figure 3.7 clearly testify to this picture and expectation. The frequency independence of conductivity over the low frequency range shown clearly establishes the conducting nature of carbon obtained. The conductivity values for carbon synthesized from CB and DCB are about 7.5 * 10^{-3} and 5.5 * 10^{-3} S cm^{-1}.

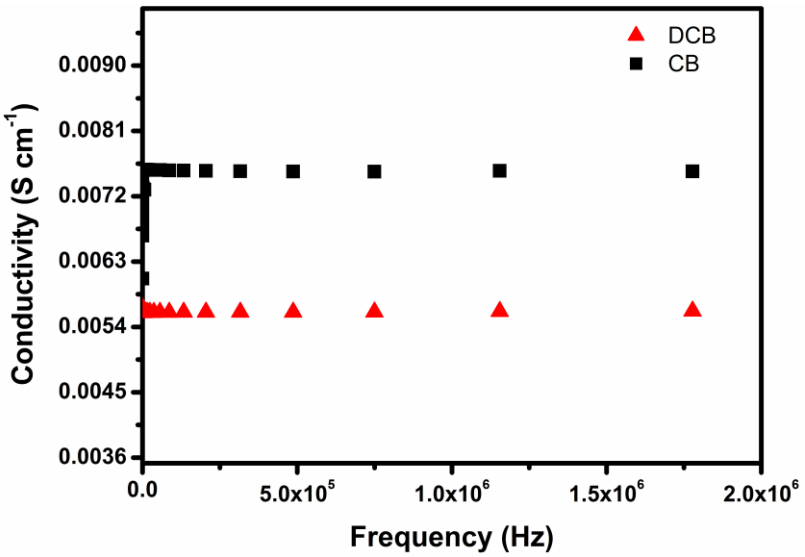

Figure 3.7 *Conductivity of the CNSs obtained in both cases*

3.4 Mechanism

Pulsed laser photochemical synthesis of carbon nanomaterials appears to be a relatively unexplored area as compared to many other techniques used to form carbon. Carbon formation by laser pyrolysis of organic compounds by laser heating of an immersed graphitic target is a more explored technique with respect to laser processing of liquid materials. [24,25] Separately, a mixture of graphitic and polymeric carbon is shown to result along with gaseous and low volatile hydrocarbons by photolysis of liquid Benzene and Toluene at high photon energy (193 nm from ArF laser).[26] The wavelength at 193 nm provides intense energy amounting to an approximate value of 620 kJ/mol in a molecular system. This clearly exceeds the bond dissociation energies of C=C (611-632 kJ/mol), phenyl C-H (473 kJ/mol) and C-C bond energies of all systems and a breakdown of the aromatic ring also entails. Hence a complete photolytic cleavage of all types of bonds will occur in an ArF laser system as previously described. A 248 nm KrF laser system does not provide such high energy, but enough energy (~482.3 kJ/mole) to dissociate the readily photolabile carbon-halogen bond. The energy required to dissociate the C-Cl bond is ~311 kJ/mole. The C=C bonds of the benzene ring require a bond dissociation energy of ~566.5 kJ/mole. Hence the 248 nm laser pulses cannot breakdown the aromatic ring. There have been some previous theoretical investigations of dissociation of halobenzenes in UV laser.[27-29] DCB dissociation mechanism into phenyl and halogen radicals at 266 nm has been studied by time of flight measurements.[30] It has also been discussed that in the absence of water, CB dissociates to form a polyaromatic hydrocarbon like structure (smaller graphite-like networks) in solid ice cavities in the presence of a non-laser UV source.[31] Also, gaseous CB has been reported to dissociate to form phenyl radicals at 248 nm by KrF excimer laser source.[32]

Consequently, we can conclude that an intense laser irradiation of liquid DCB and CB at 248 nm can generate a large number of phenyl radicals because of the photo-cleavage of numerous reactive sites (C-Cl bonds). These radicals would then react with each other to form a graphitic network in the solution consisting of hexagonal rings. Increased surface energy of such graphitic networks in solution can cause them to curl around a pentagonal or heptagonal defect into the observed CNSs.[33]

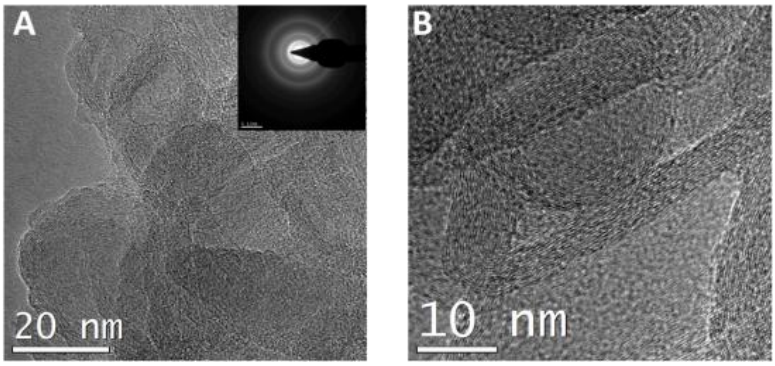

Figure 3.8 (*A-B) TEM images of Carbon Nano-onions obtained in the filtrate*

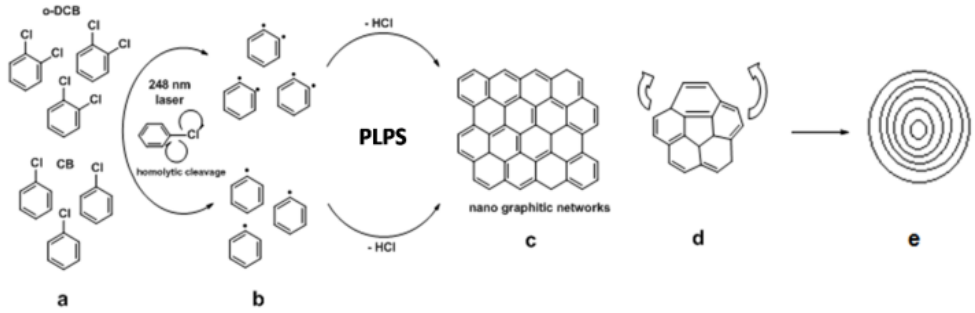

Figure 3.9 *The process of CNS formation (PLPS); (a) Reactant molecules (b) Photolytically generated free radicals (c) Graphitic networks (d) Curvature around defects (e) Carbon spheres*

This process of sphere formation will involve the initial formation of smaller spheres with sizes ranging from 2-10 nm. Such multilayered fullerene-like molecules are known as carbon nano-onions. Carbon nano-onions have a high degree of crystallinity as they are highly ordered in structure. Interestingly, the filtrate obtained after filtration of these irradiated liquids identified the presence of these carbon nano-onions corroborating our hypothesis (Pl. see Figure 3.8 and the inset which shows the Electron diffraction pattern). The larger spheres must grow around these carbon nano-onions. With increasing size the degree of disorder in the graphitic structure increases. We thus visualize this as a laser induced stitching process of aromatic free radicals

into carbon nanoparticles (Figure 3.9). The detailed mechanism (Figure 3.10) of the processes that can lead to the stitching of free radicals was confirmed by pH paper test of the solution. The pH paper turned pink confirming an acidic environment. Hence we can confirm that HCl was formed in the process as described in the detailed mechanism.

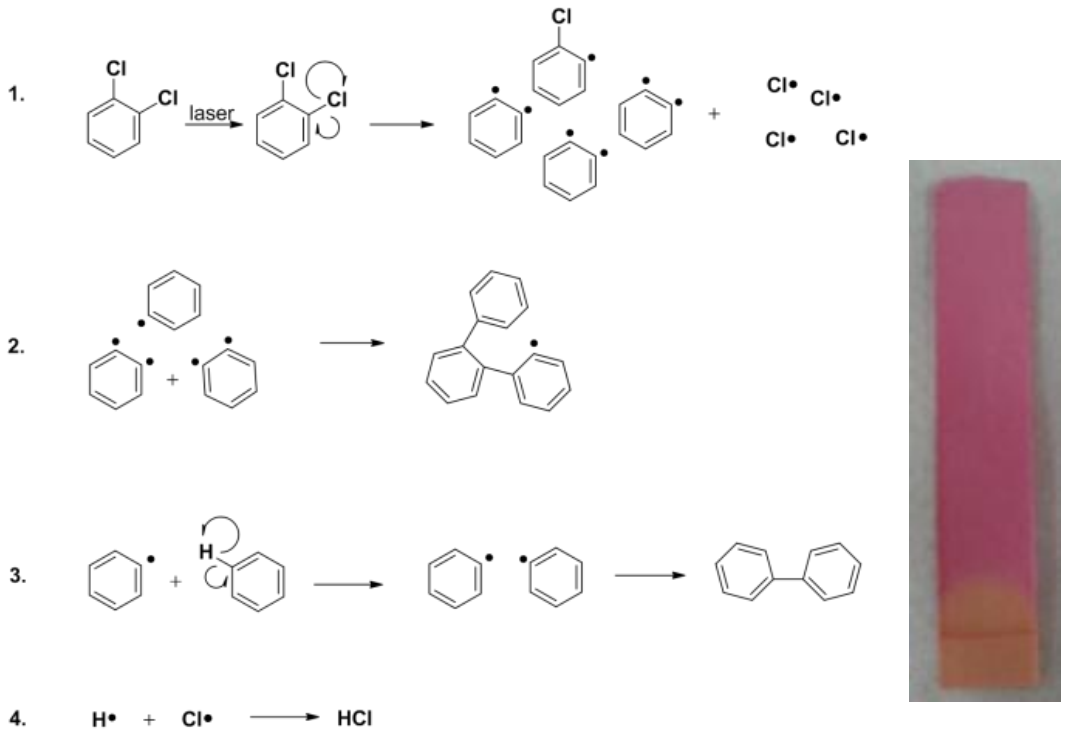

Figure 3.10 *Detailed mechanism of the processes involved in PLPS and the pH paper test.* ***1.*** *Laser induced photolysis* ***2.*** *Combination of the generated free radicals* ***3.*** *Abstraction of H free radicals to form the graphitic network* ***4.*** *H and Cl radicals combine to give an acidic environment*

The stitching process was further verified using time dependent UV-Visible spectroscopy. 25 ml of o- dichlorobenzene (DCB) was irradiated by pulsed excimer laser for different time durations such as 1 min, 4 mins, 10 mins and 30 mins separately in a quartz beaker. The black solutions obtained in each case were filtered through 0.2 μm PTFE membrane under vacuum. The filtrates obtained therein were studied by UV-visible spectroscopy (Figure 3.11).

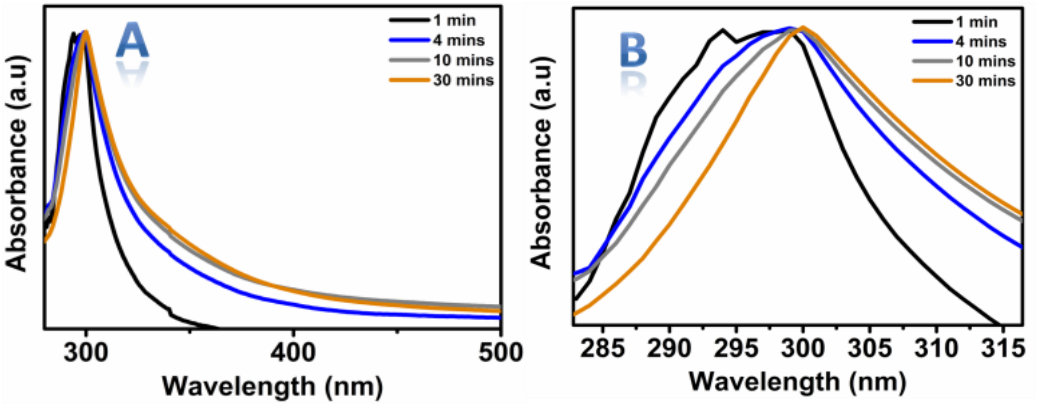

Figure 3.11 *Time dependent UV-Visible Absorption Spectroscopy*

Figure 3.11-A clearly shows an increased absorption in the visible region with increased time of irradiation. Figure 3.11-B brings out the red shift with increased time of irradiation. Thus, with increasing size of the graphitic/aromatic network a definite red shift and greater absorption in the visible region is observed. This occurs due to a gradual decrease in the HOMO-LUMO gap that accompanies the product formation by this process.

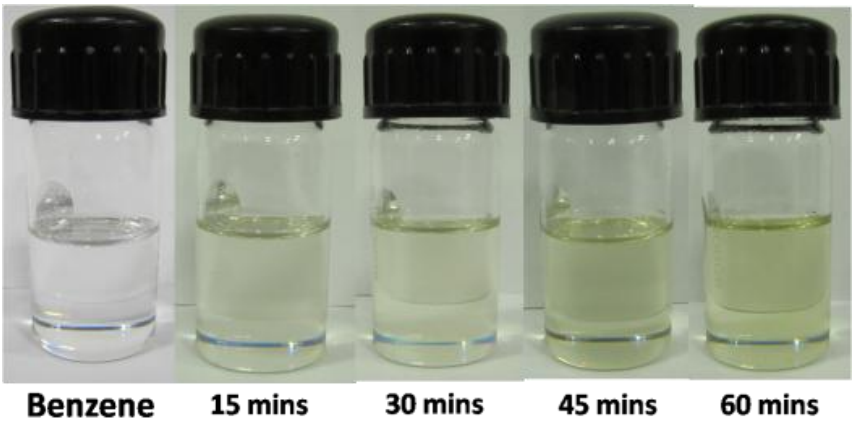

Figure 3.12 *Actual images of benzene irradiation (control experiment). Benzene was laser irradiated for different times. No carbon formation was observed.*

In order to further establish that the nano-carbon formation by stitching process is exclusive to the C-Cl bond and not due to the breakdown of the aromatic ring in the haloaromatic compounds used, a control experiment was performed with benzene

(Figure 3.12). No optically absorbing (black) compound formation was observed in the irradiation of benzene at 248 nm even after 1 h. This clearly proves that the carbon formed with haloaromatics does not involve the breakage of the carbon bonds in the aromatic ring.

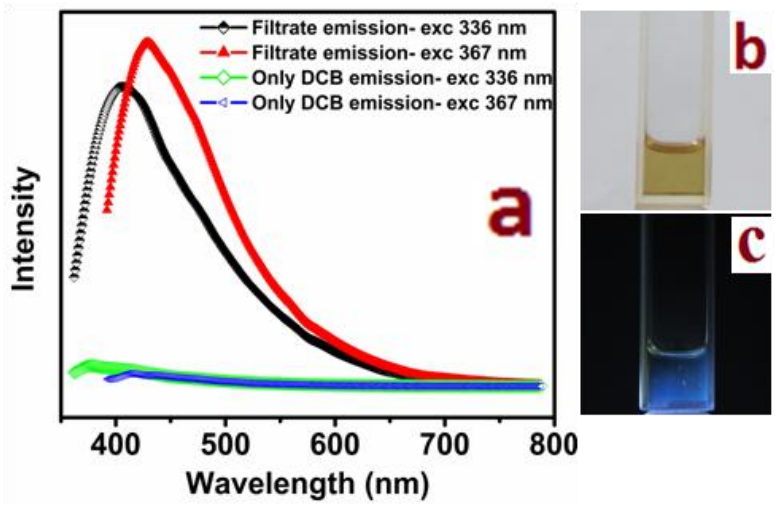

Figure 3.13 (a) *Photoluminescence spectra of filtrate obtained in case of DCB in comparison with that of only DCB itself* ***(b)*** *Image of the filtrate* ***(c)*** *Image of the blue luminescence in the filtrate*

The filtrate obtained during the separation process is found to contain nano-onions and stitched graphite like networks which have relatively smaller dimensions. A very interesting phenomenon is observed in the filtrate obtained from DCB. The filtrate shows a strong blue luminescence (Figure 3.13) which is absent in pure DCB. Since Polycyclic Aromatic Hydrocarbons (PAH) and Graphene Quantum Dots (GQDs) are known to exhibit blue luminescence, this evidence further establishes our case.[34, 35]

To establish the generic nature of PLPS process we studied the case of bicyclic 1-chloro naphthalene. Interestingly, when 1-chloro naphthalene was similarly irradiated with UV laser pulses functional carbon was obtained [Raman Spectra and I-V curve shown in Figure 3.14], verifying our claim of PLPS as a broad approach involving haloaromatics.

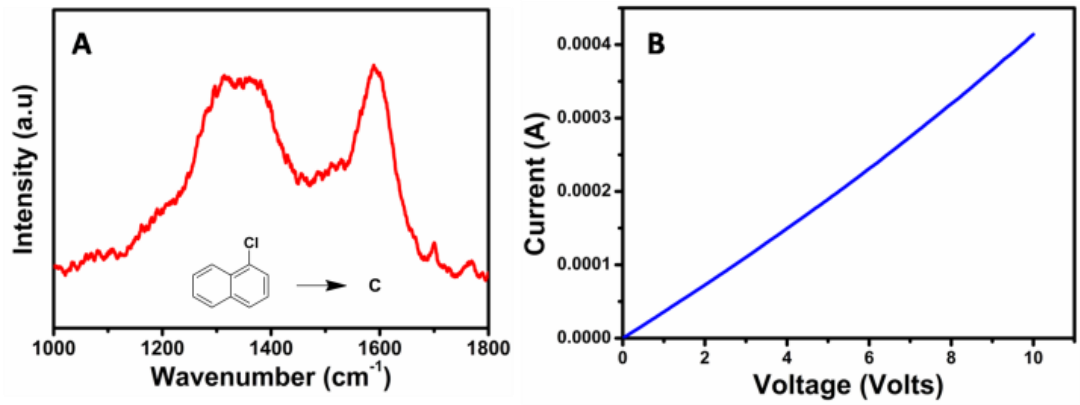

Figure 3.14 (A) *Raman spectra of the carbon obtained from 1-Chloro Naphthalene (1-CN) PLPS [structure of 1-CN and reaction to carbon form depicted inset]* ***(B)*** *I-V curve of carbon from 1-CN*

3.5 Laser irradiation studies with variation of time of irradiation, energy flux of the laser pulses and temperature

In addition to our moderate energy flux condition of 150 mJ laser energy and a standardized time period of 10 minutes of irradiation, we further irradiated 50 ml of o-DCB (similar to our original experimental procedure in the main paper) at different energy flux values of 80 mJ, 150 mJ and 200 mJ. The increase in this energy signifies an increase in the number of photons per laser pulse. The irradiation under every energy case was carried out for time intervals of 5 mins, 10 mins and 20 mins. We used UV-Visible spectroscopy, Raman Spectroscopy and Transmission Electron Microscopy for analysis of these systems.

It was clearly observed that 80 mJ being a very low energy flux, the product formation is very slow in this case since the number of photons per pulse is less as compared to the other cases. Hence no observable product was obtained at any of the time intervals for this energy case. However since the wavelength of the photon (248 nm) is constant for this UV laser, there is a certain onset of the dissociation process and product formation as indicated by the UV-Vis spectra (Figure 3.15). Figure 3.15

shows the UV-Vis absorption of the irradiated liquid at 80 mJ for 5, 10 and 20 mins in comparison with pure o-DCB. This spectrum clearly indicates product formation.

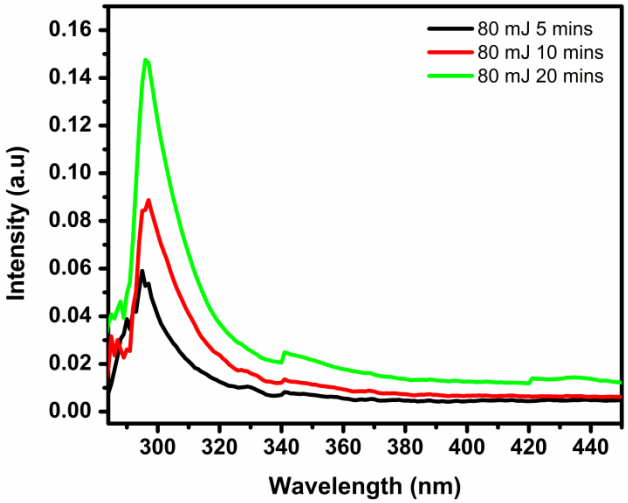

Figure 3.15 *UV-Vis Abs spectra at 80 mJ laser energy for different time intervals*

Similar process was repeated for energy flux of 150 mJ. The UV-Visible spectra for this case is shown in Figure 3.16

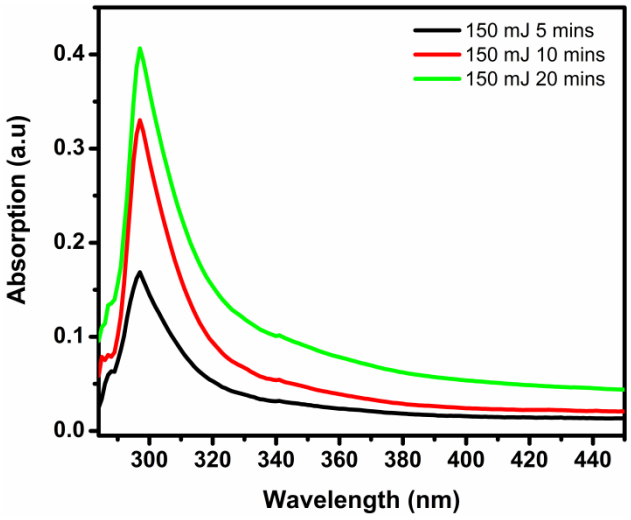

Figure 3.16 *UV-Visible Absorption spectra at 150 mJ for different time intervals*

Figure 3.16 demonstrates that with increase in energy flux (150 mJ), the number of photons increases and in turn the rate of product formation also increases. This is clear from the increased intensity of absorption in this case. Isolable carbon product can be obtained after 10 mins and 20 mins in this case.

Figure 3.17 shows the similar case of irradiation at 200 mJ laser energy flux

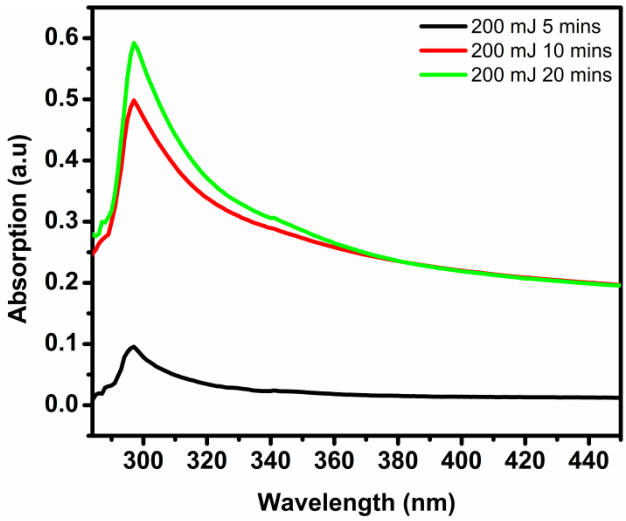

Figure 3.17 UV-Vis Abs spectra at 200 mJ laser energy for different time intervals

Figure 3.17 shows a proportionate increase in product formation due to a much higher energy of 200 mJ. The rate of product formation increases further because of a large number of photons per pulse.

It has been observed that after a certain initial time period of product formation the rate of the reaction decreases. This will occur naturally because of the formation of a black optically absorbing compound which will absorb all the incoming photons.

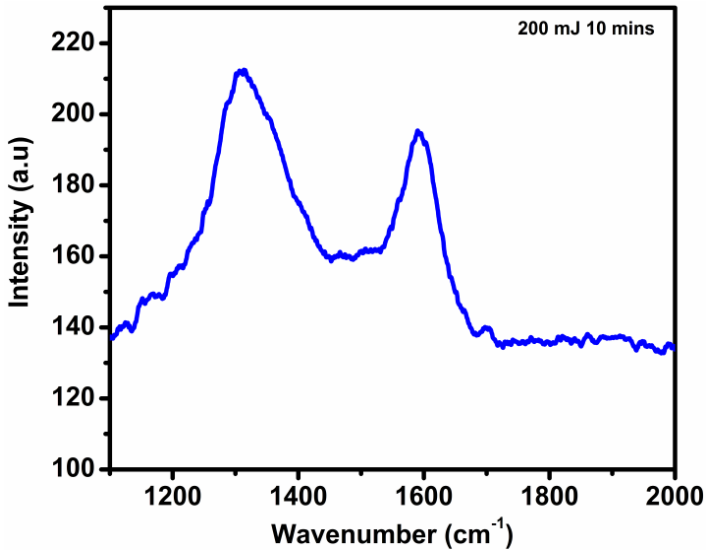

Figure 3.18 *Raman spectra of carbon obtained by irradiation of DCB at 200 mJ for 10 mins*

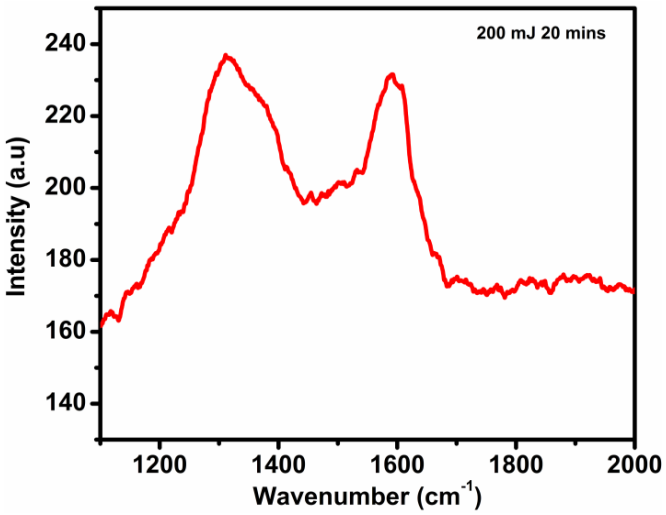

Figure 3.19 *Raman spectra of carbon obtained by irradiation of DCB at 200 mJ for 20 mins*

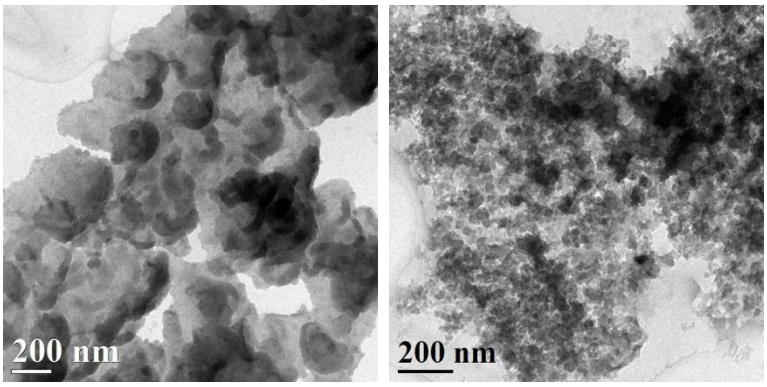

Figure 3.20 *TEM images of the Carbon Nanospheres for the 200 mJ-20 mins case*

High Temperature Case

We also irradiated o-DCB at higher temperature (100 degree Celsius) for 10 mins to observe the effect of heat during the photochemical process. No appreciable difference was observed

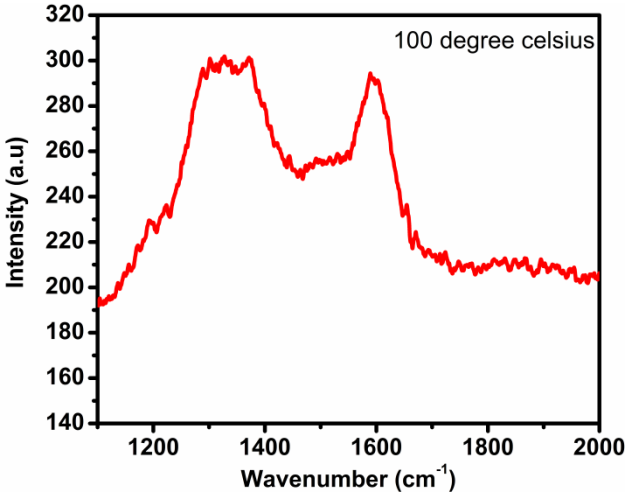

Figure 3.21 *Raman spectra of carbon obtained by irradiation of DCB at 100 degree for 10 mins*

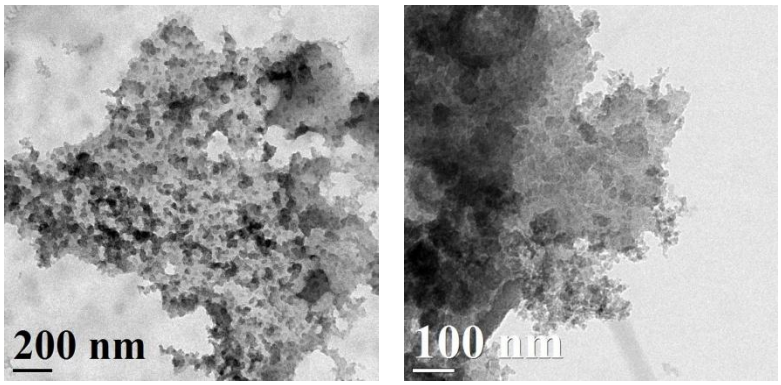

Figure 3.22 *TEM images of CNSs obtained at high temperature irradiation of DCB*

Finally, to establish even broader applicability of the method, we attempted *in-situ* synthesis of carbon based inorganic nanocomposite TiO_2-Carbon by the PLPS process. In this experiment TiO_2 (Degussa P25) powder was added to DCB and sonicated. The mixture was then irradiated by 248 nm UV laser pulses with constant

stirring. The compound obtained was filtered and then washed by centrifugation by water and acetone (3 times). We obtained clear evidence of nanocomposite formation of carbon and TiO_2 (Please see the Raman Spectra and TEM images in Figure 3.23). Such metal oxide-conducting carbon composite systems have tremendous potential for energy storage applications (ultra-capacitors and Li-ion battery). These cases however are under further investigation.

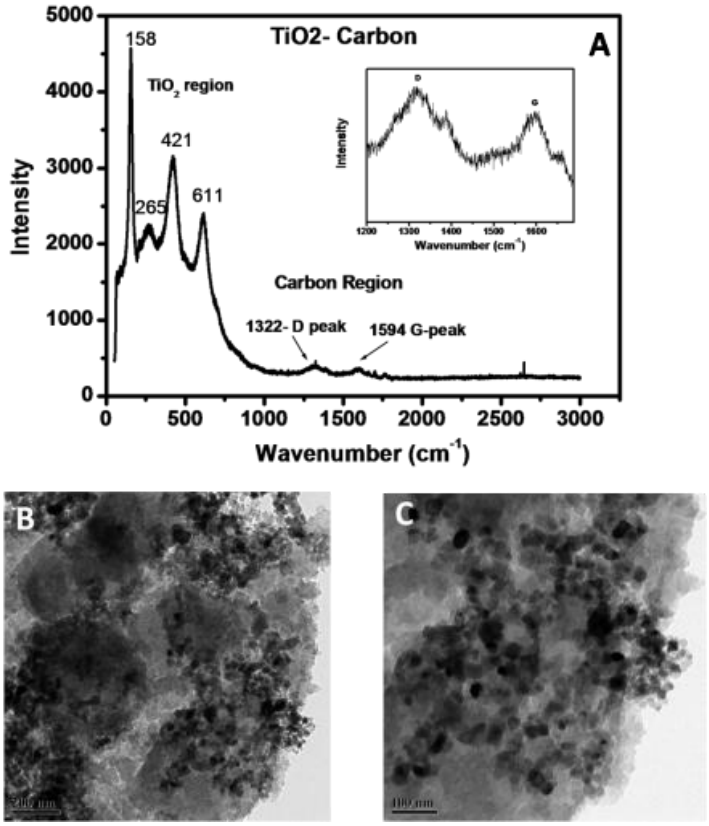

Figure 3.23(A) *Raman spectra of TiO_2- Carbon composite, inset magnified image of carbon region* ***(B-C)*** *TEM images of Carbon spheres decorated by TiO_2 nanoparticles. TiO_2 nanoparticles in a conducting carbon matrix.*

3.6 Conclusion

A novel PLPS process is introduced to engineer solid carbon nanoparticles from liquid halobenzenes by laser photochemistry at room temperature and laboratory environment. Electrically conducting high surface area carbon nano-spheres (CNSs) have thus been directly synthesized from routine laboratory solvents (which if discarded would be simply a toxic waste). Furthermore, in principle, a complete conversion of liquid materials (CB & DCB) to solid carbon can be achieved by a cyclic process of solvent irradiation and distillation to recycle the solvent followed by further irradiation, which we have confirmed. PLPS can thus prove to be a highly efficient route of nano-carbon synthesis.

It can also be foreseen that the demonstrated technique would be a generic pathway for generating a variety of carbon nanomaterials from halogen containing reactants at variable irradiation conditions as well as carbon-based nanocomposites by in-situ synthesis involving concurrent presence of other precursors, organic molecules, polymers or nanoparticles in the solvent. Laser photochemical synthesis does not require high temperature that is usually associated with the synthesis of carbon-based materials facilitating the synthesis of carbon nanocomposites with polymers and other organic compounds. Moreover, being a laser process it is applicable for direct-write schemes of localized synthesis.

It is clear that the outcome of any such laser synthesis experiment will certainly depend on the frequency of the laser through its connection with the ability of the photon energy to break specific bonds and also the pulsed (with specific pulse width) or CW character of the laser. The higher frequency laser photons will break a more diverse set of bonds and lead to more complex or possibly more amorphous and defected configurations. Lower frequency lasers, especially those in the near-infrared and infrared regions will cause thermal dissociation with different consequences for the final properties.

References

1. S. Shanmugam, A. Gedanken. J. Phys. Chem. B 2006, 110, 2037.
2. D.-C Li, L. Dai, S. Huang, A. Mau, Z. Wang, Chem. Phys. Lett. 2000, 316, 349.
3. Y. Jiang, Y. Wu, S. Zhang, C. Xu, W. Yu, Y. Xie, Y. Qian, J. Am. Chem. Soc. 2000, 122, 12383
4. C. Wu, X. Zhu, L. Ye, C. OuYang, S. Hu, L. Lei, Y. Xie, Inorg. Chem. 2006, 45, 8543
5. G. Hu, D. Ma, M. Cheng, L. Liu, X. Bao, Chem. Commun. 2002, 17, 1948.
6. X. Wu, Y. Tao, C. Mao, L. Wen, J. Zhu, Carbon 2007, 45, 2253.
7. C. Lee, H. Chiu, C. Peng, M. Yen, Y. Chang, C. Liu, Adv. Mater. 2001, 13, 1105.
8. L. Scott, M. Boorum, B. McMahon, S. Hagen, J. Mack, J. Blank, H. Wegner, A. Meijere, Science 2002, 295, 1500
9. J. Zheng, T. Ekström, S. Gordeev, M. Jacob, J. Mater.Chem. 2000, 10, 1039
10. Y. Li, I. Kinloch, A. Windle, Science 2004, 304, 276.
11. G. Che, B. Lakshmi, C. Martin, E. Fisher, Chem. Mater. 1998, 10, 260.
12. A. Reina, X. Jia, J. Ho, D. Nezich, H. Son, V. Bulovic, M. Dresselhaus, J. Kong, Nano Lett. 2009, 9, 30
13. S. Iijima, M. Yudasaka, R. Yamada, S. Bandow, K. Suenaga, F. Kokai, K. Takahashi, Chem. Phys. Lett. 1999, 309, 165
14. Y. Zhang, S. Iijima, Appl. Phys. Lett. 1999, 75, 3087.
15. E. Salonen, K. Nordlund, J. Keinonen, C. Wu. Phys. Rev. B 2001, 63, 195415
16. C. Journet, W. Maser, P. Bernier, A. Loiseau, M. de la Chapelle, S. Lefrant, P. Deniard, R. Leek, J. Fischerk, Nature 1997, 388, 756
17. A. Nieto-Marquez, R. Romero, A. Romero, J. Valverde, J. Mater. Chem. 2001, 21, 1664
18. P. Serp, R. Feurer, P. Kalck, Y. Kihn, J. Faria, J. Figueiredo, Carbon 2001, 39, 621
19. P. Wang, J. Wei, B. Huang, X. Qin, S. Yao, Q Zhang, Z Wang, G. Xu, X. Jing, Mater. Lett. 2007, 61, 4854
20. M. Li, Q. Wu, M. Wen, Nanoscale Res. Lett. 2009, 4, 1365

21. W. Li, D. Chen, Z. Li, Y. Shi, Y. Wan, G. Wang, Z. Jiang D. Zhao, Carbon 2007, 45, 1757
22. A. Ferrari, J. Robertson, Philos. Trans. R. Soc. London. Ser. A 2004, 362, 2477.
23. Y. Xie, Q. Huang, B. Huang, Carbon 2009, 47, 2290
24. S Ogale, A. Malshe, S. Kanetkar, S. Kshirsagar, Solid State Communications 1992, 84, 371
25. D. Amans, A. Chenus, G. Ledoux, C. Dujardin, C. Reynaud, O. Sublemontier, K. Masenelli-Varlot, O. Guillois, Diamond and Related Materials 2009, 18, 177
26. J. Pola, M. Urbanova, Z. Bastl, Z. Plzak, J. Subrt, V. Vorlicek, I. Gregorac, C. Crowley, R. Taylor. Carbon 1997, 35, 605
27. T. Ichimura, Y. Mori, H. Shinohara, N. Nishi, Chem. Phys. 1994, 189, 117
28. T. Ichimura, Y. Mori, H. Shinohara, N. Nishi, Chem. Phys. Lett. 1985, 122, 55
29. H. Zhang, R. Zhu, G. Wang, K. Han, G. He, N. Lou, J. Chem. Phys. 1999, 110, 2922
30. R. Zhu, H. Zhang, G. Wang, X. Gu, K. Han, G. He, N. Lou, Chem. Phys. 1999, 248, 285
31. P. Klán, A. Ansorgova, D. Favero, I. Holoubek, Tetrahedron Lett. 2000, 41, 7785
32. K. Nakayama, K. Fukatsu, K. Maruyama, K. Ogawa, T. Hasegawa, T. Morohashi, N. Fujii, Analytical Sciences 2002, 18, 907
33. A. Deshmukh, S. Mhlanga, N. Coville, J. Mater. Sci. Eng. R Rep. 2010, 70, 1
34. U. Vijh, A. Witt, K. Gordon, The Astrophysical Journal 2005, 633, 262.
35. D. Pan, J. Zhang, Z. Li, M. Wu, Adv. Mater. 2010, 22, 734.

Chapter 4

Laser synthesized super-hydrophobic conducting carbon with broccoli- type morphology as a counter-electrode for dye sensitized solar cells

A laser photochemical process is introduced to realize superhydrophobic conducting carbon coatings with broccoli-type hierarchical morphology for use as metal-free counter electrode in a dye sensitized solar cell. The process involves pulsed excimer laser irradiation of a thin layer of liquid haloaromatic organic solvent o-Dichlorobenzene (DCB). The coating reflects a carbon nanoparticle-self assembled and process-controlled morphology that yields solar to electric power conversion efficiency of 5.1 % as against 6.2 % obtained with the conventional Pt-based electrode.

4.1 Introduction

Owing to the diversity of functional forms and commensurately broad range of physical properties, carbon is now beginning to make inroads into the domain of advanced device systems. Indeed it holds a great promise as a material replacement for the currently used rare and expensive materials in the context of the emergent and next generation technologies. In recent years functional nanostructured carbon films have been examined for applications such as smart windows, sensitized solar cells, super-hydrophobic coatings, porous charge-storing networks in ultracapacitors etc.[1-4] Such films are grown by several techniques such as chemical vapour deposition (CVD), pulsed laser deposition (PLD), arc discharge, and solution processing methods such as drop casting, electrophoretic deposition, spraying etc.[2, 5-9] Most of these methods necessitate use of graphitic carbon precursors, high temperatures and chemicals such as binders and surfactants.

In the present work we apply the recently introduced concept of UV-laser photochemical stitching to obtain conducting superhydrophobic carbon coatings on FTO-coated glass substrates with unique, hierarchical and process-tunable broccoli-type morphology. We demonstrate that these unique features and properties yield excellent results for solar conversion efficiency in dye sensitized solar cells (DSSC) with such laser grown metal-free carbon films as a counter electrode.

4.2 Experimental

4.2.1 Synthesis of the carbon films:

The synthetic experimental process involves a uniform spreading of a few drops (~ 0.125 ml) of liquid DCB with the help of a Pasteur pipette on a clean glass (0.5*0.5 cm area) or FTO coated glass substrates (2*2 cm area) followed by irradiation of the liquid film by UV laser pulses (KrF excimer, λ = 248 nm, energy density ~ 170 mJ/cm^2, pulse duration 20 ns, pulse repetition rate =10 Hz) for specific time periods

up to 15 minutes. The film growth and formation process are studied at periodic intervals ranging from 15 seconds to 5 minutes. Figure 4.1 a depicts the photographic images of the process. The film morphology evolution was monitored by scanning electron microscopy (SEM), thickness measurement (Talystep) and Raman spectroscopy. The films were subsequently washed with acetone and dried in warm air flow. The carbon films were studied for their hydrophobic properties. The films grown on FTO-coated glass were used as counter-electrodes in DSSCs.

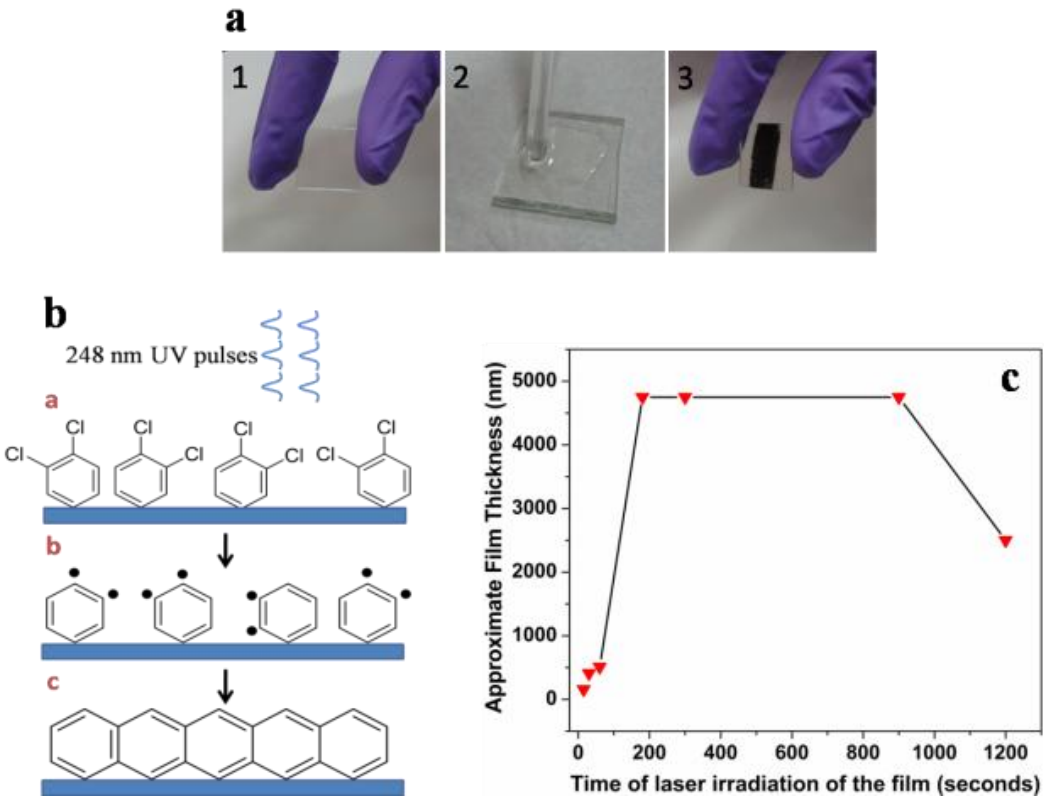

Figure 4.1 *(a) Photographic images of the synthesis steps (b) mechanism (c) time-dependent thickness measurement*

4.2.2 Materials and Equipment:

High purity (GR grade) routine organic solvent o-Dichlorobenzene (DCB) were obtained from Merck Chemicals and were used as received. A 248 nm KrF excimer laser (Lambda Physic – Germany) with a maximum average power of 40 watts (pulse energy = 150 mJ) and a pulse-width of 20 ns was used in the irradiation process. Field Emission Scanning Electron Microscopy (FESEM, Hitachi S-4200) was used for obtaining the images. Raman spectroscopy (a confocal micro-Raman spectrometer LabRAM ARAMIS Horiba JobinYvon, with laser excitation wavelength of 532 nm) was used to examine the characteristics of the carbon films. Scanning electron microscopy (FEI Quanta 200 3D) was also used for the determination of morphology. Sheet Resistance of the Films was measured on a Four-Probe system.

4.2.3 Fabrication of Solar Cells:

DSSC solar cells were made using doctor blading method using the commercially available P25 nanopowder (TiO_2). After making the films they were annealed at 450^{o}C for 60 min., the films were dipped in Ruthenium N719 dye for sensitization for 24 h at room temperature. The samples were then rinsed with ethanol to remove excess dye on the surface and air-dried at room temperature. This was followed by redox electrolyte addition and top contact of Pt coated FTO or carbon counter electrode. The electrolyte used was 0.6M 1-propyl-2, 3-dimethyl-imidazolium iodide, 0.1 M LiI, 0.05 M I_2, and 0.5 M 4-tert butylpyridine in acetonitrile/valeronitrile solution (v/v 1:1).

1.2.4 Electrolyte spreading time measurement:

The spreading time of the liquid (electrolyte) on the surface was measured by recording series of images (with 40 msec interval between two successive images) from the time of contact of liquid droplet with the substrate with a CCD camera attached with the Digidrop contact angle meter. Later, each image was analyzed using WinDrop software to get the contact angle values with time. This was done until the contact angle value reached zero, i.e., complete spreading. Care was taken to minimize the error due to evaporation of the liquid during recording. This gave the time of spreading of the electrolyte for each substrate.

4.3 Results and Discussions

4.3.1 Growth of carbon broccoli forest-like morphology

Liquid halobenzenes (eg. Chlorobenzene and o-Dichlorobenzene) when irradiated by UV laser pulses, show a unique ability to generate pure carbon nanostructures. The 248 nm photons possess enough energy to homolytically cleave the carbon-halogen bonds in such compounds generating free radicals in the process. These free radicals are then 'stitched up' together to form carbon nanoparticles by a process which we term as Pulsed Laser-induced Photochemical Stitching (PLPS).[10]

When the liquid coated substrates are irradiated by UV laser pulses the excess liquid is initially ablated and immediately decomposed. A bottom-up growth of the carbon film is then observed with an increased time of irradiation. The mechanism is depicted in Figure 4.1 b. With the substrate offering a solid support, a network of self assembled carbon nanoparticles is gradually observed to grow in to unique broccoli-like carbon morphology. The UV laser substrate surface excitation apparently provides the adequate adhesion of the carbon film to the glass or FTO:glass substrate surface (the usual role played by binders and chemicals in films). The thickness evolution of the carbon film as a function of irradiation time is shown in Figure 4.1c. It is observed that there is an increase in the film thickness up to 3 minutes of laser irradiation after which its growth saturates. This can be attributed to the exhausted supply of the reactant (dichlorobenzene molecules) which could be trapped in the developing solid architecture. However morphological changes continue to appear with time. This sequence of events is summarized in Figure 4.2.

Figure 4.2a shows the morphology features of the initial formation of the carbon film after UV irradiation for 15 seconds. We observe that primarily carbon sheet like structures are formed as a result of the initial free radical photochemical stitching [10] obtained by primary irradiation of a very thin layer of dichlorobenzene molecules supported on the substrate. As may be noted, this primary process is also accompanied by nucleation of small carbon nanoparticles. Further laser irradiation up to 30 seconds results in a significant increase in the thickness of the film and a patterned growth of carbon nanoparticles is observed (Figure 4.2b).

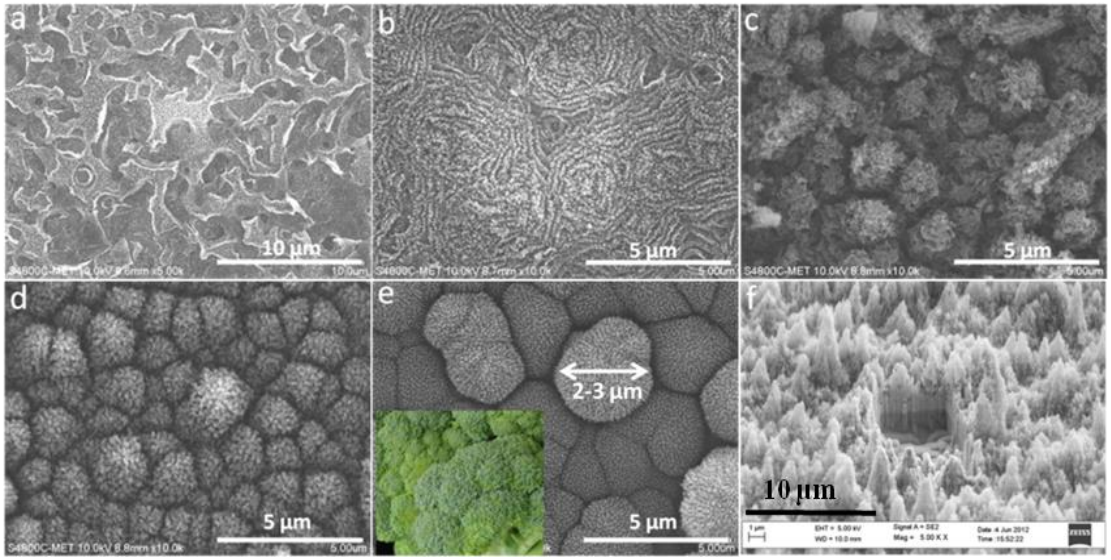

Figure 4.2 *Time evolving growth and morphology of carbon films (a) 15 seconds (b) 30 seconds (c) 1 min (d) 3 min (e) 5 min (inset broccoli) (f) cross section image of 3 min film*

Irradiation up to 1 minute is accompanied not only by an increase in the thickness of the film and the amount of carbon content, but also by a change in the morphology. Interestingly, the carbon nanoparticles agglomerate into sponge like carbon balls (Figure 4.2 c). Continued laser irradiation of the film up to 3 minutes results in a phenomenal increase in its thickness (4.5-5 micron). This certainly appears to be due to an increasingly ordered vertical growth of the carbon microballs. A rapid reaction of the dichlorobenzene wetted surface leads to the buildup of this carbon assembly during the initial time period of the laser irradiation process. Interestingly the thickness growth of carbon saturates at this stage, because the supply of the reactant molecules is now depleted. The entire organization of the film gives it an appearance of a carbon broccoli-like structure (Figure 4.2 d). Further irradiation up to 5 minutes yields a film with similar thickness but a modified morphology that clearly resembles a denser broccoli (Figure 4.2 e). Figure 4.2 e reveals a more ordered and denser arrangement in the carbon assembly.

This broccoli-like film morphology is formed together by an arrangement of numerous units (highlighted in Figure 4.2 e). Each unit of the carbon broccoli like arrangement has an approximate size of 2-3 µm. The nanoparticles that comprise each

such unit of the broccoli like structure have an approximate size of 40-50 nm (Figure 4.3) Additional evidence of the vertical alignment of these carbon forests was obtained by focused ion beam (FIB) images of the cross-section (Figure 4.4 and Figure 4.5 b, d).

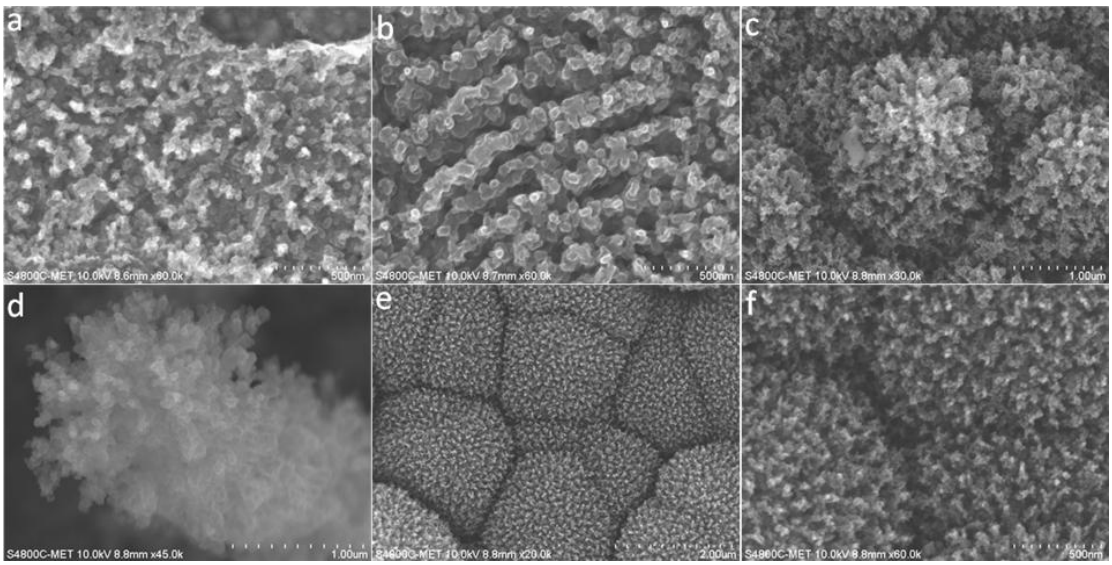

Figure 4.3 *FESEM images of the carbon films during growth. Evidence of assembly of carbon nanoparticles (a) 15 seconds (b) 30 seconds (c-d) 3 min (e-f) 5 min*

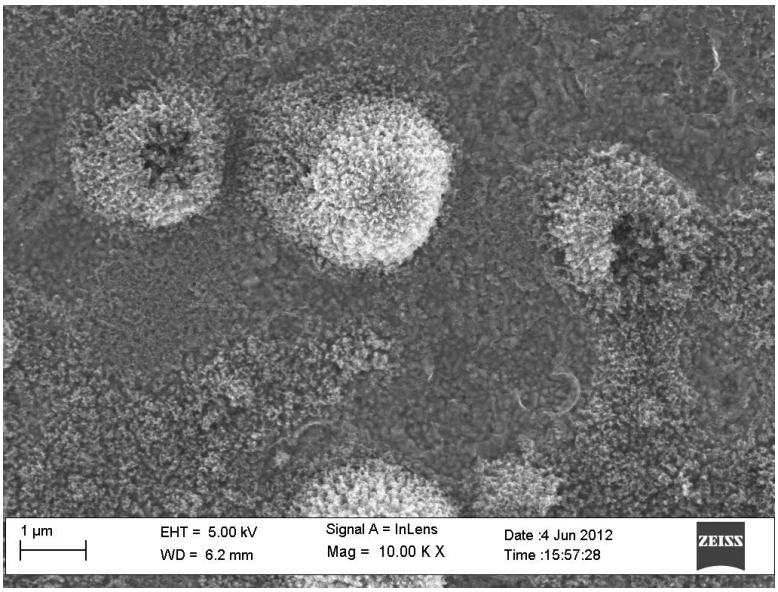

Figure 4.4 *Ruptured peaks in the 15 minutes irradiated system*

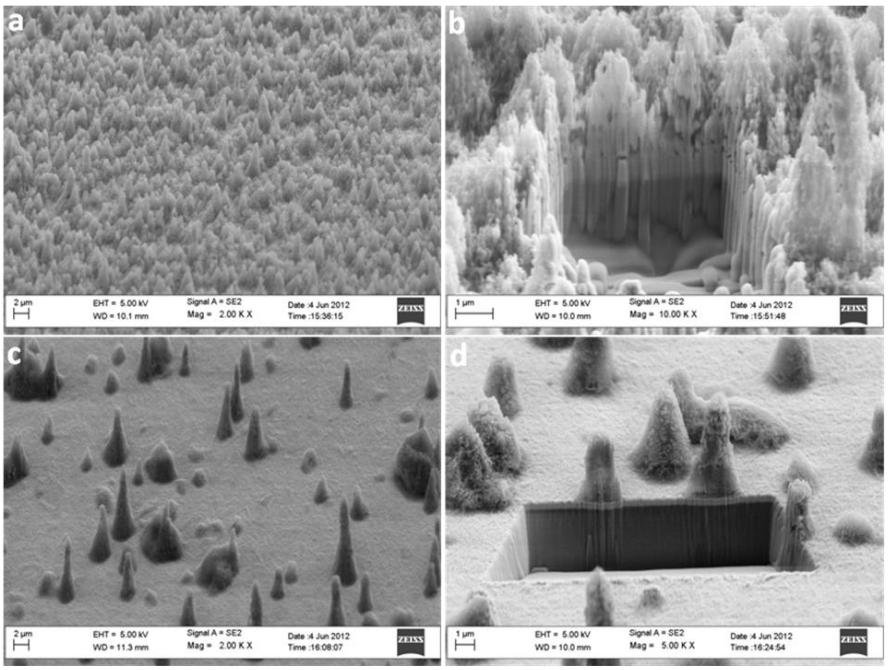

Figure 4.5. *Cross section FE SEM images of the obtained for (a-b) 3 mins film (c-d) 15 mins film*

Continued irradiation beyond 5 minutes leads to gradual changes in the morphology of the carbon structures which yield some interesting results as far as the application study is concerned. It is observed that exposure of the carbon film to excessive laser photons beyond the 15 minutes window studied in this work, results in total loss of carbon by laser ablation. Once the reactant molecules completely form carbon nanostructures by the photochemical stitching process which we have described, additional UV photons continue to strike the carbon material. The laser induced heat causes carbon loss by ablation of the target. The carbon film becomes more porous, accessible, accompanied by a decreasing film thickness. As is visible from Figure 4.5 the carbon broccoli structures formed up to 5 minutes gradually becomes less dense with more exposure to UV photons. Figure 4.5 c-d show the case of the 15 minutes laser irradiated carbon film which demonstrates a much less dense film as compared to the 3 minutes case (Figure S3-b). This structural change also leads to a significant decrease in the surface roughness leading to a less hydrophobic character as discussed later. The SEM images of the 15 minutes case also reveals systemic ruptures in the vertically aligned forests due to excessive laser treatment (Figure 4.4).

X-ray photoelectron measurements (XPS) demonstrate an increased oxygen content in the carbon film that is laser irradiated for a longer time interval (Figure 4.6). It is also observed that exposure of the carbon film to excessive laser photons beyond the 15 minutes window results in a gradual loss of carbon by laser ablation.

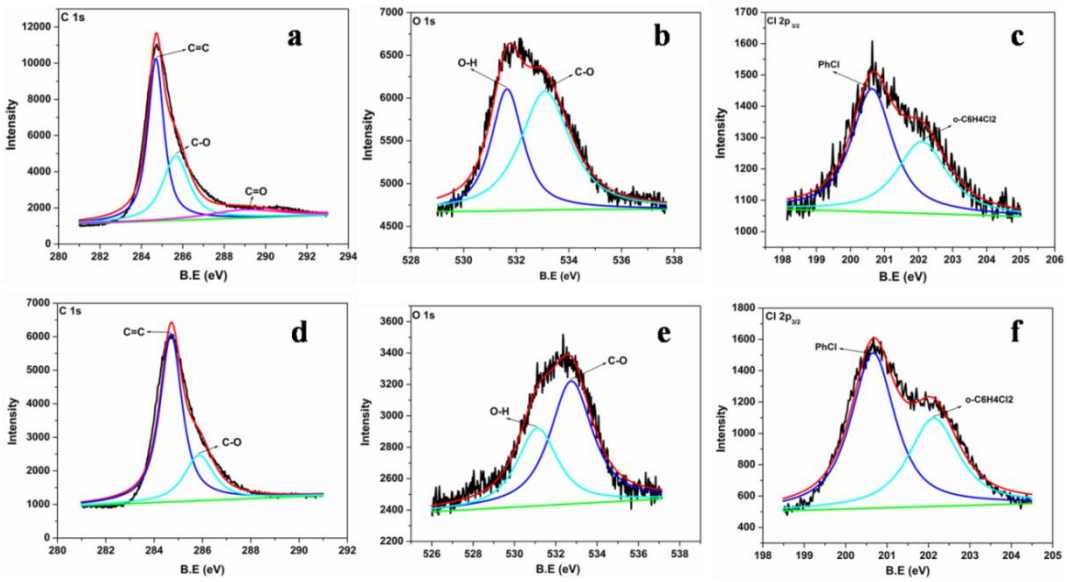

Figure 4.6. *(a-c). XPS spectra for the 3 mins case of laser carbon film (d-f). XPS spectra for the 15 mins laser carbon film.* ***a.*** *C1s* ***b.*** *O1s* ***c.*** *Cl* $2p_{3/2}$ ***d.*** *C1s* ***e.*** *O1s* ***f.*** *Cl* $2p_{3/2}$

We carried out the X-ray photoelectron spectroscopy (XPS) of two cases of carbon films, the 3 min case and the best performing 15 minutes case. It was observed that the carbon material in both cases contained the elements, carbon, oxygen and residual chlorine. The carbon in both the films existed in sp^2 C=C form and the C-O form. Similarly there was also considerable oxygen content in both the films. The C-Cl bonds detected in the XPS of these films, probably arises due to residual content from the halogen containing reactant.

The Table 4.1 and Table 4.2 give the calculated atomic percentage of C, O and Cl from the XPS of both the carbon films.

Table 4.1 (3 min film)

Element	Atomic percentage
C	**64.15**
O	**30.84**
Cl	**4.99**

Table 4.2 (15 min film)

Element	Atomic percentage
C	**60.41**
O	**33.89**
Cl	**5.69**

From the XPS data, it was thus clearly observed that the 15 minutes laser irradiated case showed a greater percentage of oxygen content than the 3 minute case. The percentage of residual Chlorine was observed to be similar in both cases.

This data can also provide a suitable explanation for a systematically increasing efficiency. As the oxygen content gradually increases, the number of catalytic sites also increase in the counter-electrode resulting in a greater performance with increasing time of irradiation.

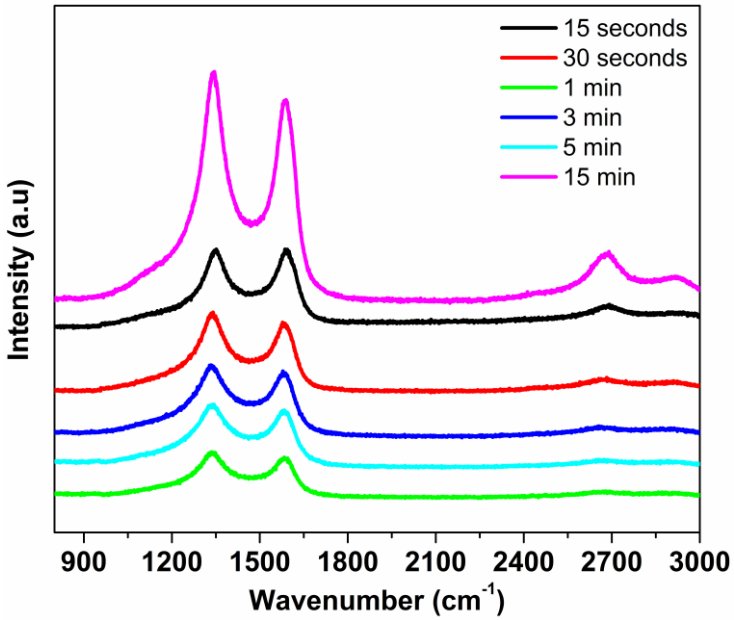

Figure 4.7 *Raman spectroscopy data of carbon films obtained by irradiation for 15 s, 30 s, 1 min, 3 min, 5 min and 15 mins.*

Raman Spectroscopy data (Figure 4.7) for all the film growth cases exhibit the usual D (defect) band (~1335 cm^{-1}) which arises due to the breathing mode of κ-point phonons of A_{1g} symmetry and the G band (~1580 cm^{-1}) that can be assigned to the E_{2g} phonon mode of sp^2 carbon atoms.[11] The I_D: I_G ratio (around ~1.1) does not appear to show a considerable change in its value with the time of laser irradiation i.e. it remains somewhat comparable during the entire growth process. The overall defect distribution remains constant over the entire range of processes. This clearly indicates that there is no basic structural change in the character of the carbon material which contributes to the process of film growth. The 2D peak obtained at ~2680 cm^{-1} arises in graphitic carbons due to the second order overtones.

Importantly, the laser synthesized carbon films are electronically conducting in nature with respect to the carbon structures formed, rendering them functional in the device context. A detailed study of the electronic properties of these films was also carried out.

4.3.2 Electronic properties of the carbon films

Measurements for electronic conductivity of all the carbon film cases were done by a two probe system using a probe station. Each film case was prepared on a non-conducting glass surface. Contacts at the two ends of the film in each case were obtained with the help of a conducting Aluminum tape. Current voltage curves were obtained across these films with Al contacts. The carbon I-V showed an ohmic behavior. The following table (Table 4.3) shows the observed and further calculated values for the electronic nature of these carbon films.

Film	**Approximate Thickness (nm)**	**Resistance (Ω)**	**Conductivity *10^2 ($S.m^{-1}$)**	**Resistivity *10^-2 (Ω. m)**
15 sec	155	709220	0.13	7.70
1 min	510	7485	3.75	0.27
3 min	4750	826	3.63	0.28
5 min	4750	558.6	5.40	0.19
10 min	4750	390.6	7.69	0.13
15 min	4750	1483.6	2.03	0.49

Table 4.3 *Electronic properties of the carbon films.*

The length of the film in each case was maintained at a constant value of l=1 cm =0.01 m

Conductivity calculation was done by the following way:

R=σ l/A; σ= RA/l; where σ is the resistivity, R is the resistance, l is the length of the film and A is the area of cross section of the conductor.

A= thickness of the film* width of the film; width in each case was a constant of 0.7 cm

It is clearly observed that the conductivity values gradually increase with time for the carbon films prepared. This also reflects in the correspondingly increasing efficiency

of the solar cells. The resistance for the 15 seconds film is very high because of the incomplete formation of the carbon film. The conductivity for the 1 min and 3 min case is nearly similar. The 5 min and 10 minutes cases show a further decreased resistance. Interestingly, the highest efficiency case (15 mins) however shows a decrease in conductivity. This may occur due to a decreased carbon content due to gradual ablation and more number of oxidized sites due to large exposure time to UV-photons. The efficiency however is high because of the larger porosity of the film and a more number of catalytic sites.

The sheet resistance (Table 4.4) of some cases (on non-conducting glass surface) obtained with a four-probe system also confirms a similar trend in the electronic properties of these carbon systems.

Carbon Film	**Sheet Resistance (kΩ/□)**
3 min	2.63
5 min	1.33
15 min	10.24

Table 4.4. *Sheet Resistance of the pure carbon films*

4.3.3 Superhydrophobic Properties

Having synthesized the films with a unique nano-assembled hierarchical morphology of pure and *conducting* carbon, we set out to explore its applicability in the domain of energy studies. There is considerable interest in replacing platinum and other precious metals from electrode systems of energy devices such as dye sensitized solar cells (DSSC). Carbon is considered to be a possible replacement material. We therefore decided to explore our coating for DSSC counter electrode application. The DSSC counter electrode must contact the electrolyte in organic solvent, hence it was necessary to first explore the properties of our coating for hydrophobicity and establish its expected superhydrophobic character based on the forest-like morphology. Needless to mention that such superhydrophobic conducting carbon

coatings can find use in several other application domains as well.

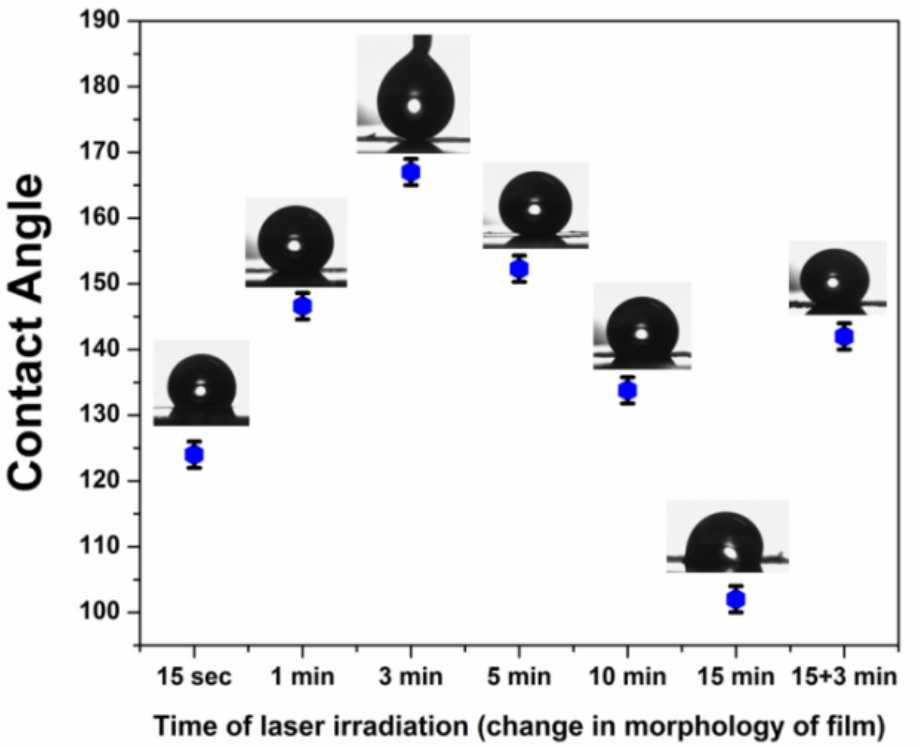

Figure 4.8 *Plot of contact angle v/s the time of laser irradiation of the films. In the last case (15+3) the film was prepared by adding DCB and irradiating for 3 mins on the original film that was irradiated for 15 mins. This process resets the hydrophobicity.*

There are several prior reports of superhydrophobic carbon coatings.[12-14] Some of the best surfaces are generated on vertically aligned carbon nanotube forests which are grown by CVD.[3,15] Since pure carbon systems do not show the desired nature under many circumstances, a fluorine containing compound/polymer (e. g. PTFE) or a semiconductor like ZnO are coated on such rough carbon surfaces.[3,16,17] Such hybrid systems offer very good results in this context. It must however be noted that most of the superhydrophobic systems reported till date have been prepared by fairly tedious procedures. The photochemically generated carbon films highlighted in our work exhibit remarkable superhydrophobicity with contact angle reaching up to a high value of 167 ± 2^{o}. Interestingly, as shown, the laser provides us with a tool to manipulate the hydrophobic character of this system.

As seen from **Figure 4.8** the hydrophobicity of the films increases initially with the time of irradiation because of the gradual formation of the carbon forest morphology

and an accompanying increase in the surface roughness. However, with increasing time of irradiation the vertical alignment begins to breakdown. This leads to a systematic decrease in the hydrophobicity. The best superhydrophobic behavior is shown by the 3 min irradiated film (contact angle = 167±2^{o}) with a very low sliding angle (< 4°) which implies the slippery nature of the surface according to Cassie-Baxter model.[18] Again, the 5 min irradiated film also shows superhydrophobicity (contact angle = 152±2^{o}) but the extent of hydrophobicity is less as compared to the 3 min film, as also revealed by a higher sliding angle (> 40°). This higher tilt angle can be attributed to the partial filling of pores on the sample surface by the water droplet according to Wenzel model. The surface energies of the 3 min and 5 min films are calculated using three different liquids (DMSO, Ethylene glycol and Glycerol). The calculation shows an increase in the surface energy from 3 min to 5 min irradiated film (44.8 mN/m to 47.1 mN/m, respectively). This surface energy is composed of two components namely dispersive or non-polar component and a polar component. The polar component of surface energy increases from 3 min to 5 min film (14 mN/m to 18 mN/m) whereas dispersive component decreases slightly (30.7 mN/m to 29.2 mN/m). This means that the 5 min film has more hydrophilic character than that of 3 min film. This fact is in accordance with the lower contact angle value for the 5 min film as compared to the 3 min film. Moreover, the enhanced polar character binds the water droplet on the surface and results in higher sliding angle for the 5 min film. When the film reaches a less hydrophobic state (eg. the 15 minute case) the hydrophobicity can be reset to higher values as shown in Figure 4.8. This can be done by adding 1-2 drops of additional DCB and re-irradiating the film for a period for 3 minutes. The contact angle suddenly increases to 142±2^{o}. This process can be repeated again for achieving a higher contact angle. This laser induced tunability of the hydrophobicity of carbon films is certainly an interesting scientific realm.

4.3.4 Application as counter-electrodes in solar cells

One of the most important parameters of the cost and functioning of a DSSC is the counter-electrode which is usually Platinum (Pt) coated on FTO-glass. However the high cost of Pt and the high temperature treatment necessitated by its use act as a barrier to the cost effective implementation of the DSSC technology. Since carbon possesses the required properties of low production cost,
good electronic conductivity and chemical stability, there have been several reports of use of Graphene, N-doped Graphene, CNTs, amorphous carbon which show good conversion efficiency [19-30]. In view of the interesting properties of our carbon films we examined their performance as counter electrodes for DSSC. We studied herein laser-formed films with irradiation time of 15 seconds (minimum) to 15 minutes (maximum). Cyclic Voltammetry (CV) (Figure 4.9) was performed on all the carbon electrodes and compared with Pt/FTO electrode to study the electrochemical catalytic activity of these electrodes.

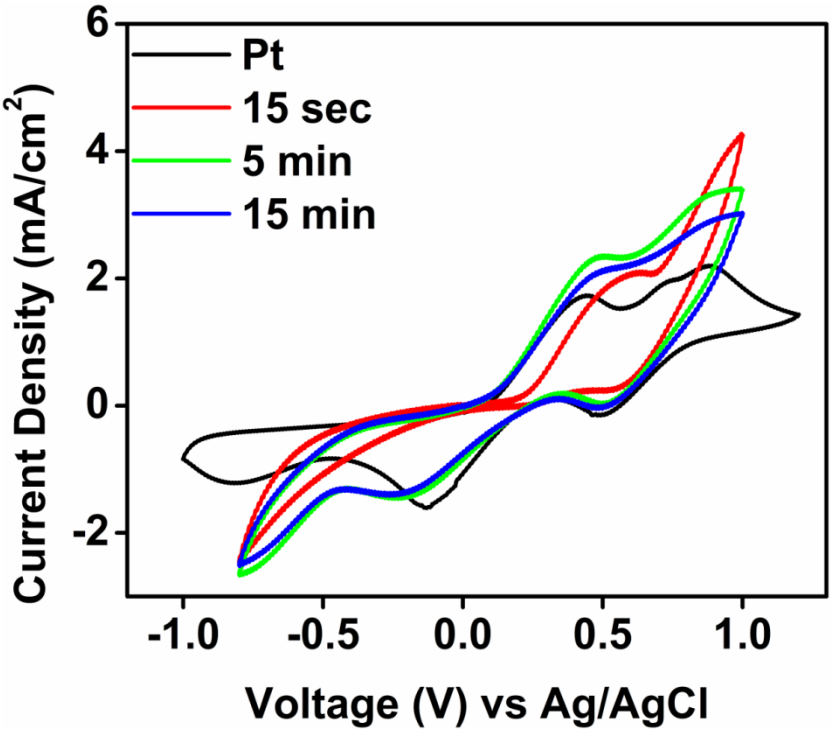

Figure 4.9 *Cyclic Voltametry studies of Pt and various carbon electrodes.*

CV was measured using a conventional three electrode system which consisted of Pt as counter electrode, Ag/AgCl as reference electrode and the synthesized carbon films

or Pt/FTO as a working electrode. Lithium perchlorate was used as supporting electrolyte and acetonitrile as solvent. Two pairs of peaks are observed for both materials, similar to what has been reported for comparable systems in the literature. The first pair of peaks represents the oxidation–reduction of I_2/I_3^- and the second present at more negative side represents oxidation–reduction of I^-/I_3^-.[26] The counter electrode in dye sensitized solar cells is responsible for catalyzing the reduction of I_3^- to I^-, hence the rate of this reaction is of prime importance in obtaining high efficiency in DSSCs. Carbon counter-electrodes (prepared by varying the irradiation time) show catalytic activity comparable to that of Pt counter electrode. The catalytic activity shows a systematically increasing trend with the increase in irradiation time. The electrochemical stability of the carbon film (best case- 15 min) was measured by CV over several cycles. A reasonable stability was exhibited by the carbon film (Figure. 4.10).

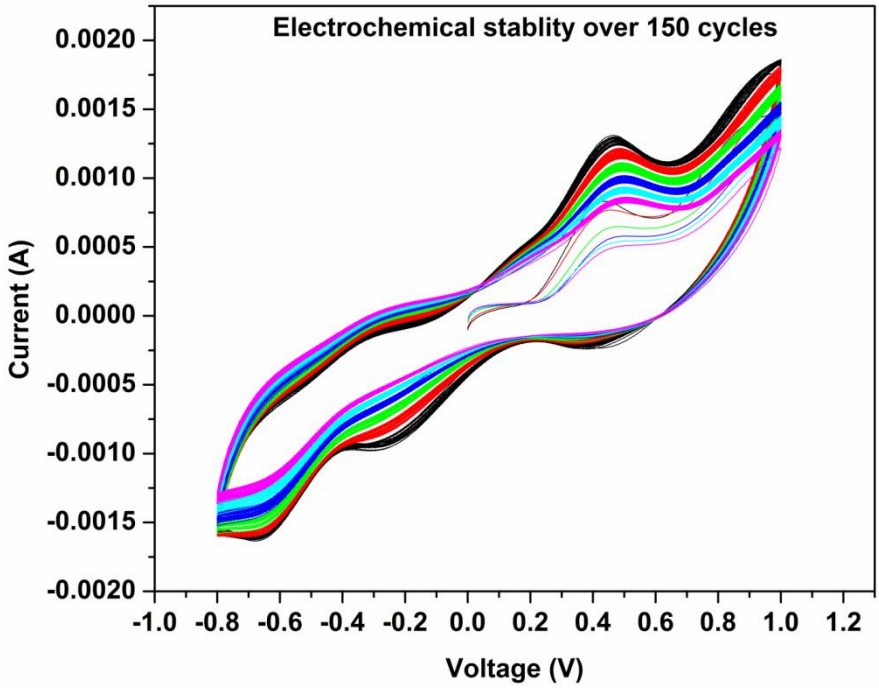

Figure 4.10. *Electrochemical stability of the 15 min laser formed electrode over 150 cycles*

Figure 4.11 and Table 4.5 compares the I-V characteristics of Pt/FTO counter electrode and those of laser formed carbon counter electrodes for different irradiation times. From the graph it is clear that as the irradiation time increases the fill factor of the DSSCs also increases. This can be attributed to decrease in catalytic charge transfer resistance (R_{ct}) which improves with irradiation time. [20] This was studied using electrochemical impedance measurements (Figure 4.12).

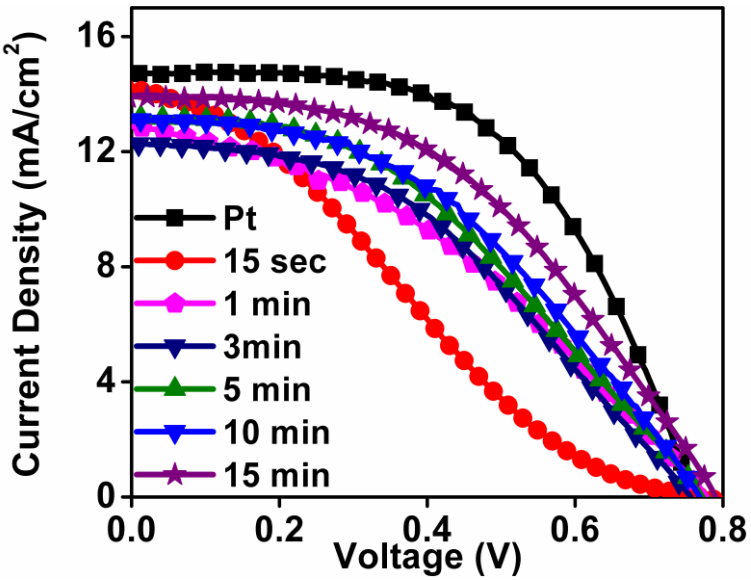

Figure 4.11 *IV curves for laser formed carbon counter electrode and the conventional Pt electrode*

Name	*V_{oc} (V)*	*J_{sc} (mA/cm^2)*	*FF (%)*	*η (%)*
Pt CE	**0.76**	**14.7**	**55.6**	**6.2**
15 sec	**0.77**	**14.11**	**25.39**	**2.8**
1 min	**0.78**	**12.82**	**37.7**	**3.8**
3 min	**0.75**	**12.22**	**42.5**	**3.9**
5 min	**0.77**	**13.14**	**41.4**	**4.2**
10 min	**0.77**	**13.02**	**44.3**	**4.4**
15 min	**0.79**	**13.86**	**46.1**	**5.1**
20 min	**0.66**	**8.37**	**53.7**	**2.9**

Table 4.5 *Photovoltaic performance using laser formed carbon counter electrode compared with conventional Pt electrode*

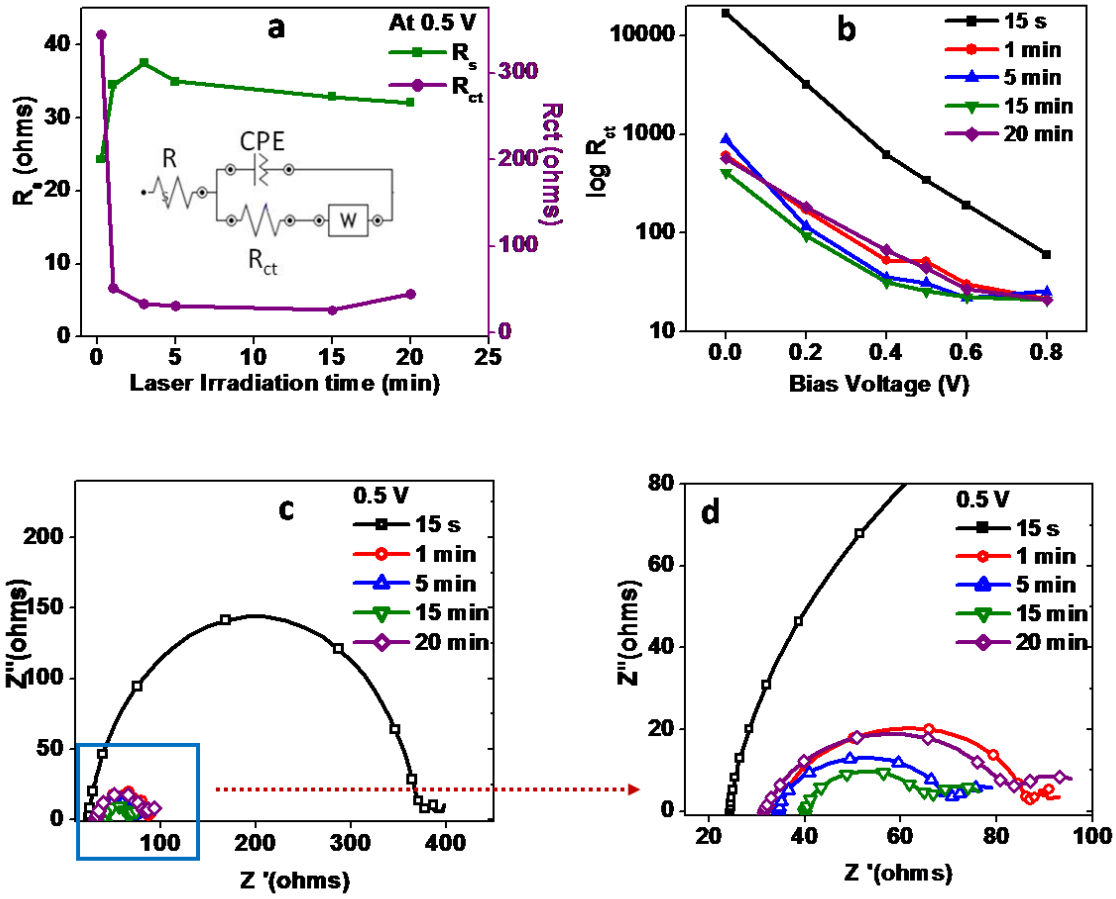

Figure 4.12 *a) Plot of Rs and Rct vs Laser irradiation time b) Plot of Log Rct vs bias voltage for 15 s, 1min , 5 min , 10 min and 20 min laser formed Counter electrode c) Nyquist plots for various C counter electrodes as bias voltage 0.5V d) zoomed version of (c)*

Impedance measurements were performed to determine the catalytic charge transfer resistance of all carbon counter electrodes. A Symmetric cell assembly was used to perform this measurement. The electrochemical cell consisted of two identical carbon counter electrodes with area 0.5 cm^2 each placed in a flip chip assembly. The space between the electrodes was filled with liquid electrolyte consisting of 0.5M LiI and 0.05 M I_2. The frequency range selected for the measurement was 0.1 Hz to 1 MHz with AC amplitude of 10 mV. Nyquist plots were obtained for all carbon counter electrodes by applying bias voltage varying from 0V to 0.8V. Nova 1.7 software was used to fit the above Nyquist plots. Figure 4.12a shows plot of R_s and R_{ct} versus laser irradiation time and inset is the equivalent circuit used to fit the Nyquist plots. Figure 4.12b shows the plot of log R_{ct} versus applied voltage for different laser formed

counter electrodes. $R_{s,}$ which is the serial ohmic resistance which reflects the adhesion of carbon film on substrate is between 25-35 Ω for all laser formed counter electrodes. This indicates that all laser formed counter electrodes have fairly good adhesion with the substrate. All the laser formed films follow proper trend where R_{ct} decreases with increase in applied bias voltage and the Nernst diffusion impedance starts increasing as seen in Figure 4.12b. From the Figure 4.12 a and b it is seen that catalytic charge transfer resistance, R_{ct} decreases with irradiation time and is lowest for 15 min laser formed film. It shows an increase for 20 min laser irradiated case. This matches well with the high efficiency performance of 15 min laser formed counter electrode compared to the other laser formed counter electrodes. 15 min laser formed counter electrode has shows good catalytic activity and better charge transfer properties at the electrode electrolyte interface. Figure 4.12c-d shows Nyquist plots of 15 min laser formed counter electrodes at different bias voltage.

An increasing porosity obtained with laser irradiation for higher irradiation time as described before, contributes to greater interaction between the electrolyte and the carbon. Evidence of the increasing access of the surface morphology of laser synthesized films to the electrolyte can be obtained from the spreading time evaluation with acetonitrile (electrolyte used in DSSC). Figure 4.13 shows that the spreading time of the electrolyte shows a systematic decline for films exposed to UV pulses for greater time durations. This increased wettability in less time allows the electrolyte to access the pores easily and rapidly resulting in facile charge transfer kinetics and supporting the improved efficiency for the 15 min film. Simultaneously, the ruptures created in the carbon forest structures (Figure 4.13) due to excess photons may create defects or catalytic sites which result in the gradually increasing efficiency with time of irradiation. Furthermore, as discussed previously, the XPS data reveals an increased oxygen content in films with a higher laser irradiation time. These oxygenated sites contribute to added catalytic centers in the carbon system additionally contributing to the systematically increasing efficiency.

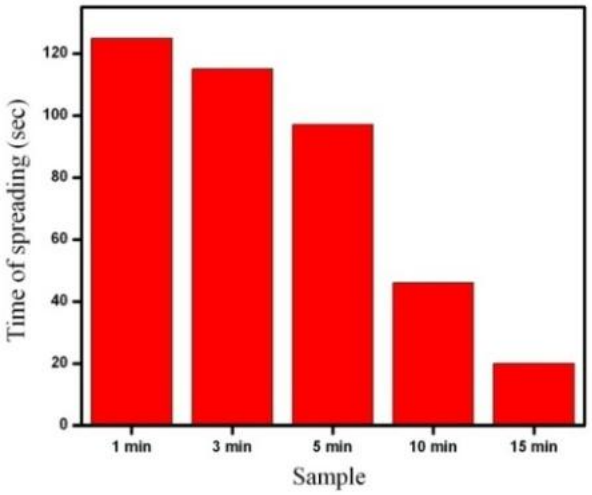

Figure 4.13 *Decreasing time of spreading of electrolyte over the carbon film over an increasing time of irradiation*

The efficiency for a carbon film prepared by irradiation for 20 minutes however decreases to 2.9%. This occurs due to loss of the generated carbon by laser ablation. Since the amount of carbon in the 20 min film is very less, there is a direct impact on its performance in the device.

To summarize the various properties of the carbon films, mainly electronic conductivity, hydrophobicity and photovoltaic performance, it would be useful to relate the three properties to the time dependent morphology evolution of the laser synthesized carbon films. It is quite clear that the carbon morphology does not completely take its form in the initial time period of formation namely the 15 sec case. Hence the conductivity, hydrophobicity and photovoltaic performance, all propertied exhibit low values at the beginning. With evolution of carbon film with irradiation time, the thickness of the film increases and conductivity values proportionally ascend. As the vertical orientation and thickness grows, the surface becomes rough, contributing to the increasing hydrophobicity. The hydrophobic behavior of the surface peaks at the 3 min case. With further irradiation, the surface morphology breaks down and the surface becomes more porous and accessible. The carbon density in the bottom layer of the electrode however remains high, as confirmed by the increasing conductivity of the films. Finally the contribution of the film to solar conversion efficiency depends on conductivity and the catalytic activity of the carbon.

The former increases systematically resulting in a corresponding rise in power conversion efficiency of the cells. The catalytic activity depends on the catalytic sites and access of the electrolyte. As we have discussed previously, the number of catalytic sites gradually increases (defects, oxygen content etc) and as the film surface becomes more porous and accessible to the electrolyte, the photovoltaic performance also shows an upward trend with time. The 15 min case shows higher performance in spite of a slightly lesser conductivity as compared to the 10 min case. This could be due to a higher degree of catalytic sites in this film.

We also investigated the films for their field emission properties and the preliminary results are encouraging (Please see appendix). We believe that the process can be fine tuned with added elemental inclusions to enhance these properties as well.

Before we conclude it is fruitful to comment on the possible technological utilization of such a process of making carbon film and the related cost issues. Towards this end, it is important to note that Laser processes are now fairly common in the semiconductor and device industries, and methods such as laser scribing, laser etching, laser patterning and even laser CVD are a common place. CW and pulsed lasers of different wavelengths are used for these tasks. An interesting thing about lasers is that they can deliver on different processing needs in an industry, hence their evaluation in terms of cost issues is somewhat complicated and depends on the specifics of the total processing involved. Even in solar cell industry lasers are used for scribing and patterning. Hence a process such as the one presented here could facilitate fabrication by direct writing in addition to the other functions a UV laser could perform. At this stage the work presented here emphasizes the science of growth and related possibilities. A full cost analysis and comparison with the ongoing use of precious metals is out of scope of this paper. Finally, it is also useful to state that given the localized character of the method, it should not be too complicated to control the dispensation of the products by suitable rapid evacuation protocols with chemical pumping to limit any environmental issues.

4.3.5 Adhesion test of the films

The carbon films are prepared by a room temperature, binder free process and not subjected to any thermal post treatment. Considering these parameters, the adhesion of the films onto FTO-glass is quite good. The films do not peel of easily. In fact, we tested the adhesion by sticking a scotch tape on the surface of the film and removing it. As can be seen from the figure below, the amount of carbon removed by the scotch tape is negligible except at the very edges, highlighting the good adhesion of these laser prepared carbon films.

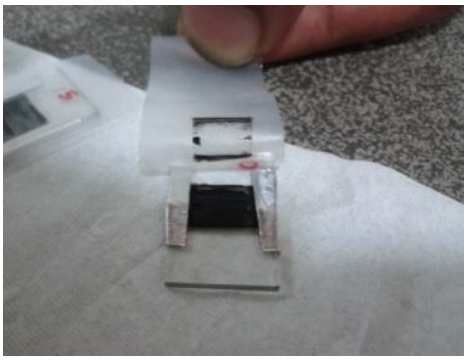

4.14 *Scotch tape after complete removal*

4.4 Conclusion

Unique vertically-aligned and hierarchically carbon nanoparticle-self assembled film morphology of conducting carbon with a broccoli-like structure is realized by a facile pulsed laser process involving irradiation of supported haloaromatic organic film. Such films exhibit remarkable superhydrophobicity that can be easily process-tuned. Given the electronically conducting and porous nature of the carbon films, we explored their application as counter-electrodes in dye sensitized solar cells. The laser generated carbon on FTO-glass surfaces demonstrates excellent catalytic activity, almost comparable to the established Pt-coated FTO counter-electrodes.

Furthermore this new laser induced photochemical deposition process can be implemented on several substrates to generate different morphologies of carbon.

References

1. X. Wang, L. Zhi, K. Mullen, Nano Lett, 2008, 8, 323-327.
2. G. Zhu, L. Pan, T. Lu, T. Xu, Z. Sun, J. Mater. Chem, 2011, 21, 14869.
3. K. K. S. Lau, J. Bico, K.B.K. Teo, M. Chhowalla, G.A.J. Amaratunga, W.I. Milne, McKinley, G.; Gleason, K.; Nano Lett, 2003, 3, 1701-05
4. Q. Wu, Y. Xu, Z. Yao, A. Liu, G. Shi, ACS Nano. 2010, 4, 1963
5. K. S. Kim, Y. Zhao, H. Jang, S. Y. Lee, J. M. Kim, K. S. Kim, J. H. Ahn, P. Kim, J. Y. Choi, B. H. Hong, Nature 2009, 457, 706-709
6. T. Friedmann, K. McCarty, J. Barbour, M. Siegal, D. Dibble, Appl. Phys. Lett. 1996, 68, 1643
7. C. Journet, W. Maser, P. Bernier, A. Loiseau, M. Lamyde la Chapelle, S. Lefrant, P. Deniard, R. Leek, J. Fischerk, Nature 1997, 388, 756
8. J. Bardecker, A. Afzali, G. Tulevski, T. Graham, J. B. Hannon, A. K. Y. Jen, J. Am. Chem. Soc. 2008, 130, 7226–7227
9. V. Pham, T. Cuong, S. Hur, E. Shin, J. Kim, J. Chung, E. Kim, Carbon 2010, 48, 1945-51.
10. R. Gokhale, V. Thakare, S. Warule, B. Lefez, B. Hannoyer, J. Jog, S. Ogale, AIP Advances, 2012, 2, 022130.
11. A. Ferrari, J. Robertson, Phil. Trans. R. Soc. Lond. A 2004, 362, 2477
12. L. Feng, Z. Yang, J. Zhai, Y. Song, B. Liu, Y. Ma, Z. Yang, L. Jiang, D. Zhu, Angew. Chem. 2003, 115, 4349 –4352
13. S. Li, H. Li, X. Wang, Y. Song, Y. Liu, L. Jiang, D. Zhu, J. Phys. Chem. B. 2002, 106, 9274-9276
14. L. Zhang, D. Resasco, Langmuir, 2009, 25,4792–4798
15. Z. Han, B. Tay, M. Shakerzadeh, K. Ostrikov, Appl. Phys. Lett. 2009, 94, 223106
16. C. T. Hsieh, W. Y. Chen, F. L. Wu, Carbon 2008, 46, 1218 -1224
17. L. Huang, S. Lau, H. Yang, E. Leong, S. Yu, S. Prawer, J. Phys. Chem. B 2005, 109, 7746-7748
18. A. Marmur, Langmuir 2003, 19, 8343-8348
19. J. Chen, K. Li, Y. Luo, X. Guo, D. Li, M. Deng, S. Huang, Q. Meng, Carbon 2009, 47, 2704-2708.

20. L. Brennan, M. Byrne, M. Bari, Y. Gun'ko, Adv. Energy Mater. 2011, 1, 472–485.

21. E. Ramasamy, W. Lee, D. Lee, J. Song, Appl. Phys. Lett. 2007, 90, 173103.

22. Z. Huang, X. Liu, K. Li, D. Li, Y. Luo, H. Li, W. Song, L. Chen, Q. Meng, Electrochemistry Communications, 2007, 9 ,596–598.

23. M. Wu, X. Lin, T. Wang, J. Qiu, T. Ma, Energy Environ. Sci, 2011, 4, 2308-2315.

24. A. Kay, M. Gratzel, Sol. Energy Mater. Sol. Cell 1996, 44, 99–117

25. J. Roy-Mayhew, D. Bozym, C. Punckt, I. Aksay, ACS Nano. 2010, 4, 6203

26. K. Imoto, K. Takahashi, T. Yamaguchi, T. Komura, J. Nakamura, K. Murata, Sol. Energy Mater. Sol. Cell 2003, 79, 459–469.

27. K. Huang, Y. Wang, R. Dong, W. C. Tsai, K. W. Tsai, C. C. Wang, Y. H. Chen, R. Vittal, J. J. Lin, K. C. Ho, J. Mater. Chem., 2010, 20, 4067–4073

28. G. Wang, W. Xing, S. Zhuo, Journal of Power Sources 2009, 194, 568–573

29. K. Li, Y. Luo, Z. Yu, M. Deng, D. Li, Q. Meng, Electrochem. Commun. 2009, 11, 1346

30. M. Yen, C. Hsieh, C. Teng, M. Hsiao, P. Liu, C. Ma, M. Tsai, C. Tsai, Y. Lin, T. Chou, RSC Advances 2012, 2, 2725–2728

Chapter 5

An efficient heteroatom-doped carbon electro-catalyst for oxygen reduction reaction by pyrolysis of protein-rich pulse flour cooked with SiO_2 nanoparticles

Development of a highly durable, fuel-tolerant, metal-free electro-catalyst for oxygen reduction reaction (ORR) is essential for robust and cost-effective Anion Exchange Membrane Fuel Cells (AEMFCs). Herein, we report the development of nitrogen-doped (N-doped) hierarchically porous carbon-based efficient ORR electrocatalyst from protein-rich pulses. The process involves 3D silica nanoparticle templating of the pulse flour(s) followed by their double pyrolysis. The detailed experiments are performed on gram flour (derived from chickpeas) without any *in-situ/ex-situ* addition of dopants. The N-doped porous carbon thus generated shows remarkable electrocatalytic activity towards ORR in the alkaline medium. The oxygen reduction on this material follows the desired 4-electron transfer mechanism involving the direct reduction pathway. Additionally, the synthesized carbon catalyst also exhibits good electrochemical stability and fuel tolerance. Results are also obtained and compared for the case of soyabean flour having higher nitrogen content to highlight the significance of different parameters in the ORR catalyst performance.

5.1 Introduction

Several efforts have been devoted to the search for high performance electrocatalyts for oxygen reduction reaction (ORR) in fuel cells to replace the current state-of-the-art Pt/C based system.[1-5] These explorations of new catalytic alternatives have brought out that nitrogen doped (N-doped) carbon materials are perhaps the best-performing, inexpensive, highly stable, and environmentally-friendly metal-free alternatives to Pt/C. Prior works report on the ORR performance of doped carbon electrocatalysts based on carbon nanofibers, CNTs, graphene, mesoporous carbons etc. [6-35] These materials have been synthesized by *in-situ* (addition of an organic compound in the precursor) or post-synthesis processing (eg. Post-synthesis anneal in NH_3 atmosphere etc.) techniques. The established synthetic routes towards such hetero-atom doped carbon systems include chemical vapor deposition, high temperature annealing, solvothermal synthesis, pyrolysis of organic compounds/polymers etc.

Recently, several interesting approaches have been adopted for the synthesis of highly effective doped carbon/composites as ORR catalysts. Silva *et al*. synthesized N and O doped mesoporous carbon catalysts by carbonization of polyaniline on silica support followed by acid etching of the framework.[36] N doped carbon nanocages have been synthesized by Chen *et al*. using MgO as a template and pyridine as the precursor.[37] A wet chemistry route followed by heat treatment strategy for the synthesis of doped graphene from GO was used by Liang *et al*. and Lin *et al*. [38, 39] Some of the recent efforts towards better hetero-atom doped carbon electrocatalysts are summarized in Table 5.1. [40-44] In spite of much work in this area, most of the catalysts, including graphene based systems, necessitate tedious synthetic protocols and expensive techniques/precursors, thereby restricting their applicability only to the small scale. The most important challenge in fuel cells remains the synthesis of high-performance and cost-effective catalytic replacements for ORR that can be manufactured potentially on large scale for a widespread technological deployment.

No.	Reference	Material	Onset Potential of Material (V) with loading	Onset Potential (V) of commer. Pt/C ref used with loading	Electrolyte used	Ave. No. of elec. transferred	Reference Electrode used
1	Jeon et al. *J. Am. Chem. Soc.* **2013**, 135, 1386−1393	Acid functionalized GNPs	-0.16 (5µl of 1mg/ml dispersion of catalyst)	0.5 (Similar procedure used to drop cast)	0.1 M KOH	2.6-3.6	Ag/AgCl
2	Li et al. *J. Am. Chem. Soc.* **2012**, 134, 18932−18935	N-doped colloidal graphene quantum dots	0.04, 0.10 and 0.14 V negative to reference Pt/C (15 µg on GCE)	Not mentioned (15 µg on GCE) 20% wt. Pt on Vulcan XC-72R	0.1 M KOH	3.9	SCE
3	Yang et al. *J. Am. Chem. Soc.* **2012**, 134, 16127−16130	Phosphorus doped ordered mesoporous carbon	-0.11	Not mentioned (20 wt % Pt supported on Vulcan XC72R carbon	0.1 M KOH	3.9	Ag/AgCl
4	Wohlgemuth et al. *J. Mater. Chem. A*, **2013**, 1, 4002–4009	N doped carbon aerogels	Not precisely defined but significantly negative to platinum. 5 µl of 5 mg/350 µl	Not mentioned 20 wt% Pt@C	0.1 M KOH	3.3	Ag/AgCl
5	Zhang et al. *Adv. Mater.* **2013**, *25*, 4932–4937	Phosphorus doped graphene	0.92 10 µ L of 1mg/mL solution	0.95 10 µ L of 1mg/mL solution	0.1 M KOH	3-3.8	RHE
6	Wang et al. *Angew. Chem. Int. Ed.* **2012**, 51, 4209 –4212	Boron and Nitrogen doped CNTs	Not precisely defined but shown to be comparable to platinum. 10 µ L of 1mg/mL solution	Not defined precisely 20% platinum on Vulcan XC-72R; E-TEK	0.1 M KOH	Close to 4	SCE
7	Silva et al. *J. Am. Chem. Soc.* **2013**, 135, 7823−7826	N and O doped mesoporous carbon	0.94 (100 µg/cm^2)	Not precisely mentioned but graph shows comparable behavior Pt/C (1% Pt)	0.1 M KOH	~4	RHE
8	Chen et al. *Adv. Mater.* **2012**, *24*, 5593–5597	N doped carbon nanocages	-0.13 10 µ L of 2mg/mL solution	-0.03 10 µ L of 2mg/mL solution Pt/C (with Pt loading of 20%,	0.1 M KOH	3.27	Ag/AgCl

9	Lin et al. *Adv. Energy Mater.* **2012**, *2*, 884–888	N doped Graphene	-0.1 141 μ g cm^{-2}	No comparison shown Pt/C (20 wt.% Pt)	0.1 M KOH	3.6	Ag/AgCl
10	Liang et al. *Angew. Chem. Int. Ed.* **2012**, 51, 11496 –11500	S,N doped mesoporous Graphene	-0.06 10 μ L of 2 mg/mL solution	-0.03 20 wt% Vulcan Pt/C	0.1 M KOH	3.6	Ag/AgCl
11	Liu et al. Nano Res. **2013** DOI 10.1007/s12274-013-0307-9	N doped nanoporous carbon	0.88 (0.1mg/cm^2)	- (0.1mg/cm^2) Pt/C (20 wt.% Pt loading	0.1 M KOH	~4	RHE
12	Yang et al. *J. Am. Chem. Soc.* 2011, *133*, 206–209	N doped mesoporous carbon	0.035	0.06 20 wt% Pt/C (130 μg loading)	0.1M KOH	~3-4	Ag/AgCl
14	**Our Work**	**N doped heirarchicall y porous carbon**	**0.949 (255μg/cm^2)**	**0.972 (25 μg/cm^2) Pt/C (20 wt.%)**	**0.1 M KOH**	**3.5**	**RHE**

Table 5.1 *Comparison of this work with recent literature*

Synthesis Protocols of the materials for the references given above:

1. *"Edge-selectively functionalized graphene nanoplatelets (EFGnPs) with different functional groups were efficiently prepared simply by dry ball milling graphite in the presence of hydrogen, carbon dioxide, sulfur trioxide, or carbon dioxide/sulfur trioxide mixture"- Jeon et al. J. Am. Chem. Soc.* ***2013****, 135, 1386−1393*

2. *"Solution chemistry approach to nitrogen-doped colloidal graphene quantum dots with well-defined structures" - Li et al. J. Am. Chem. Soc.* ***2012****, 134, 18932−18935*

3. *"Phosphorus-doped ordered mesoporous carbons (POMCs) with different lengths were synthesized using a metal-free nanocasting method of SBA-15 mesoporous silica with different sizes as template and triphenylphosphine and phenol as phosphorus and carbon sources, respectively". HF was used for etching subsequently. Yang et al. J. Am. Chem. Soc.* ***2012****, 134, 16127−16130*

4. *"A one pot hydrothermal synthesis towards nitrogen doped organic aerogels with tunable surface area and nitrogen content is presented. The gels were synthesized from a sustainable glucose carbon precursor with 2-pyrrol-carboxaldehyde (PCA) as the nitrogen source and borax mineral as the structure forming agent." Wohlgemuth et al. J. Mater. Chem. A,* ***2013****, 1, 4002–4009*

5. *"A facile, low-cost and scalable thermal annealing method for the synthesis of PG using graphite oxide (GO) and triphenylphosphine (TPP) as carbon and phosphorus sources, respectively"- Zhang et al. Adv. Mater.* ***2013****, 25, 4932–4937*

6. *"Developed a facile approach to metal-free BCN graphene of tunable B/N co-doping levels as efficient ORR electrocatalysts simply by thermal annealing GO in the presence of boric acid and ammonia" Wang et al. Angew. Chem. Int. Ed.* ***2012****, 51, 4209 –4212*

7. *"Mesoporous oxygen- and nitrogen-doped carbons were synthesized from in situ polymerized mesoporous silica-supported polyaniline (PANI) by carbonization of the latter, followed by etching away the mesoporous silica template from it." Silva et al. J. Am. Chem. Soc.* ***2013****, 135, 7823−7826*

8. *"NCNCs were prepared with pyridine as the precursor in this study". MgO was used as a template - Chen et al. Adv. Mater.* ***2012****, 24, 5593–5597*

9. *GO was treated with SiO_2 nanoparticle solution and then dual doped using chemicals like BDS/Melamine (heat treatment). HF was used for etching. Liang et al. Angew. Chem. Int. Ed.* ***2012****, 51, 11496 –11500*

10. *"N-doped porous carbon materials have been prepared by a simple one-step pyrolysis of ethylenediaminetetraacetic acid (EDTA) and melamine in the presence of KOH and Co(NO3)2·6H2O."- Liu et al. Nano Res.* ***2013,*** *DOI 10.1007/s12274-013-0307-9*

11. *"NG is successfully prepared from GO and a solid N precursor, urea, both of which are low-cost and being manufactured in large quantities." "Well-mixed*

GO and urea were pyrolyzed at 800 ° C in an inert environment" - Lin et al. Adv. Energy Mater. ***2012****, 2, 884–888*

13. *In our work, the protein enriched food grain powder (gram flour, soyabin) was cooked with SiO_2 nano-particle dispersion in water (Ludox). During swelling of the grain matrix SiO_2 nanoparticles were uniformly sucked-in and distributed. After SiO_2 etching by HF hierarchically porous nitrogen doped conducting carbon was obtained which gave a good ORR performance.*

In this work, we demonstrate a simple and potentially scalable pyrolysis route accompanied by a silica nanoparticle pre-uptake 3D-templating rocedure to generate nitrogen-doped mesoporous carbon exhibiting excellent electrocatalytic performance for ORR in the alkaline medium. Interestingly, this process does not involve any *in-situ* doping or complex post-synthetic protocols. The precursor constituents (especially high protein content) themselves contribute to the nitrogen doping in the final product. We experimentally demonstrate the synergistic effects of hierarchical porosity, high conductivity and heteroatom doping of the carbon systems that result in the high-performance of this electrocatalyst. To the best of our knowledge, there are scarce reports on nitrogen-doped carbon systems that exhibit such a wide range of highly desirable properties.

Interestingly, the precursors used for our process are the commonly available, protein-rich pulse grains (gram flour and soybean), which also happen to be a common high protein food waste source. A large amount of such protein rich precursors are available at negligible cost. This work thus represents one modest step towards finding out an interesting and concurrent solution to two critical problems namely efficient yet inexpensive energy materials and food waste management.

5.2 Experimental

5.2.1 Materials and Instrumentation:

Gram flour and soybean grains were obtained commercially and ground to a fine powder. Ludox [colloidal silica nanoparticle (size ~12 nm) dispersion in water- 40 wt%] and conc. hydrofluoric acid (HF) were obtained from Sigma Aldrich. Split tube furnace with alumina tube and argon atmosphere was used for the pyrolysis process.

5.2.2 Experimental Process:

Three carbon samples were prepared from gram flour powder. The samples were named as gram flour-derived mesoporous carbon (GFMC) and soybean-derived mesoporous carbon (SBMC).

Preparation of GFMC1: 5 g gram flour was heated to boiling in excess deionized (DI) water for 5 h. The slurry was filtered through a regular Whatman filter paper. The filtered product was pyrolyzed at 1000 ^{o}C for 4 h in flowing argon atmosphere. The sample was then treated with conc. HF solution to remove oxide impurities. The product was washed with DI water by centrifugation several times and then dried in an oven. The dried sample was again treated at 1000^{o}C for 4 h in argon atmosphere. This sample was then characterized.

Preparation of GFMC2: 5 g gram flour was boiled for 5 h in 50 ml Ludox solution to form dense slurry. The SiO_2-gram flour slurry obtained was pyrolyzed in argon atmosphere at 1000 ^{o}C in a split tube furnace for 4 h. The obtained product was treated with conc. HF to remove silica nanoparticles and generate porous carbon. The carbon was recovered and washed several times with DI water by centrifugation. It was dried overnight in an oven and then re-heated at 1000 ^{o}C for 4 h in argon atmosphere. The final material was used for characterization.

Preparation of GFMC3: This sample was prepared by the same procedure as for GFMC2 except for boiling 5 g gram flour in 200 ml Ludox solution (higher relative silica content).

In order to establish the generalized nature of the precursors and the process we also prepared carbon samples using soybean powder for comparison:

Preparation of SBMC1: 5 g soybean powder was boiled for 5h in 50 ml Ludox solution. The rest of the procedure was similar to that followed for GFMC1.

Four such cases of mesoporous carbon materials (GFMC1, GFMC2, GFMC3 and SBMC1) were then characterized fully for their physical properties and were also tested for electrocatalytic performance in ORR. The figurative description of the general synthesis protocol is shown in Figure 5.1.

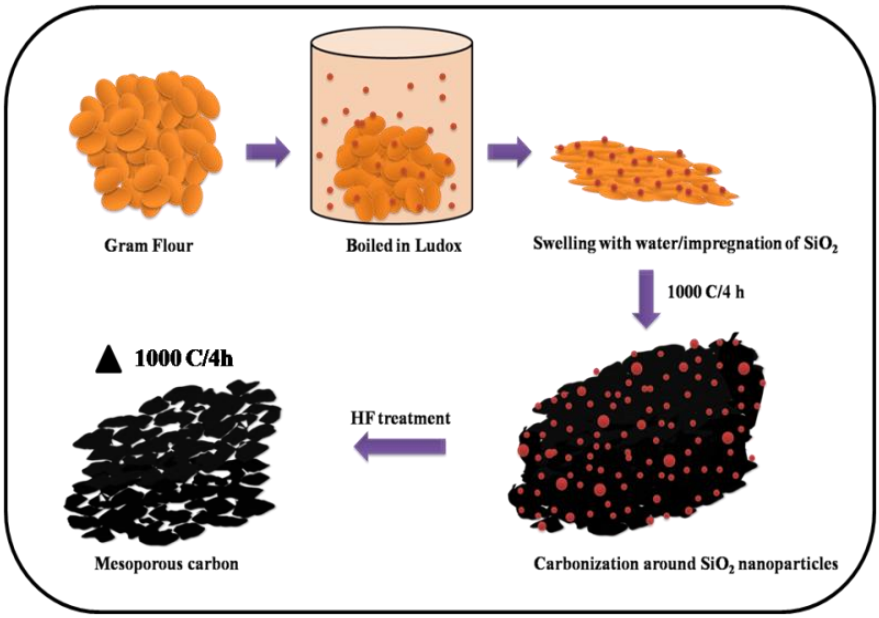

Figure 5.1 *Diagrammatic representation of the synthesis protocol.*

5.2.3 Characterization:

The materials were characterized for their physical properties using various techniques including BET surface area, Raman spectrometer, HR-TEM, FE SEM, X-ray Diffraction and X-ray Photoelectron Spectroscopy (XPS). The electro-catalytic activity of the N-doped porous carbon was analyzed using cyclic voltammetry and linear sweep voltammetry techniques in oxygen saturated 0.1 M KOH solution. Field Emission Scanning Electron Microscopy (FESEM, Nova NanoSEM 450) and High Resolution-Transmission Electron Microscopy (HR-TEM, FEI Tecnai 300) were used. The surface area of carbon was obtained from BET surface area measurements (Quantachrome Quadrasorb automatic volumetric instrument). X-ray photoelectron

spectroscopy (XPS) (ESCA-3000, VG Scientific Ltd. UK, with a 9 channeltron CLAM4 analyzer under vacuum better than 1* 10^{-8} Torr, Al Ka radiation (1486.6 eV) and a constant pass energy of 50 eV) was employed to study the chemical state of carbon in the materials respectively. X-ray Diffraction (XRD, Philips X'Pert PRO) and Raman spectroscopy (a confocal micro-Raman spectrometer LabRAM ARAMIS Horiba JobinYvon, with laser excitation wavelength of 612 nm) was also used.

Resistance Measurement:

5 mg of each carbon catalyst was mixed with 1 mg of binder (kiner). 1 ml NMP was added and the contents were ground in a mortar pestle to make a uniform thin paste. 7 µL of the paste was drop casted on 0.5* 0.5 cm of glass slide. Resistance was measured over a distance of 1 mm on a two-probe system.

Electrochemical studies: Biologic electrochemical workstation was used for all electrochemical analysis with conventional three- electrode test cell from Pine Instruments. Hg/HgO and graphite rode were used as the reference and counter electrodes, respectively. A glassy carbon (GC) electrode (5 mm diameter) embedded in Teflon was used as working electrode. Working electrode was polished using 0.3 μm alumina slurry and cleaned using water and alcohol. 10 mg of the catalyst was dispersed in 2 ml of dimethyl acetamide by ultrasonication. 10 μL from the prepared slurry was drop casted on the GC electrode followed by coating of 2 μL of 0.1 % Nafion® solution. Cyclic voltammetric (CV), chronoamperometric (CA) and rotating disc electrode (RDE) studies were carried in 0.1 M KOH (Aldrich). 5 mV s^{-1} scan rate was used for both RDE and cyclic voltammetric analysis. For RDE analysis, oxygen and nitrogen saturated 0.1 KOH was used respectively for oxygen saturated and oxygen free environment.

For Rotating ring disc electrode (RRDE), carbon samples (50µl) coated on 0.24 cm^2 glassy carbon disc surrounded by platinum ring were used as working electrode and Hg/HgO and graphite rode were used as reference and counter electrode respectively. Oxygen saturated 0.1 M KOH was used for RRDE analysis. All potentials were converted to RHE by calibrating Hg/HgO in hydrogen saturated 0.1 M KOH.

5.3 Results and Discussion

Gram flour (derived from chickpeas) was chosen as a precursor because of its specific constitution having high protein content (22 %) (Table 5.2) {from US agricultural research service nutrition database} since it is a natural source of heteroatom(s). Since the building block of a protein is a nitrogen-containing amino acid, the amount of nitrogen content in the precursor material is clearly very high. This eliminates the need for any *in-situ* or *ex-situ* addition of a dopant in the process. Most of the food-grain pulses (e.g. chickpeas used in our case) possess a permeable seed coat that assists in water-uptake. When the pulses are boiled, a softening of the seed-coat takes place resulting in large water uptake, and expansion of the grains. This process is normally used in the cooking of grains.[45]

In our work, we boiled the obtained gram flour (chickpea flour) in varying amounts of Ludox (12 nm SiO_2 nanoparticle dispersion in water, 40 wt. %). Since the size of the silica nanoparticles is around 12 nm, these particles penetrate the seed coat along with water. This results in the widespread uptake and distribution of SiO_2 nanoparticles in the expanded pulses framework. The pyrolysis of such boiled gram flour in argon atmosphere results in carbonization of these precursors around the 3D nanoscale SiO_2 templates. The HF treatment of this carbon removes SiO_2 as H_2SiF_6 in an exothermic reaction resulting in the generation of several mesopores. The random structure of the pure grain flour matrix is shown in Figure 5.2a. The penetration of the grain matrix and the simultaneous distribution of the SiO_2 nanoparticles in expanded gram flour framework after the boiling process are also depicted in Figure 5.2b.

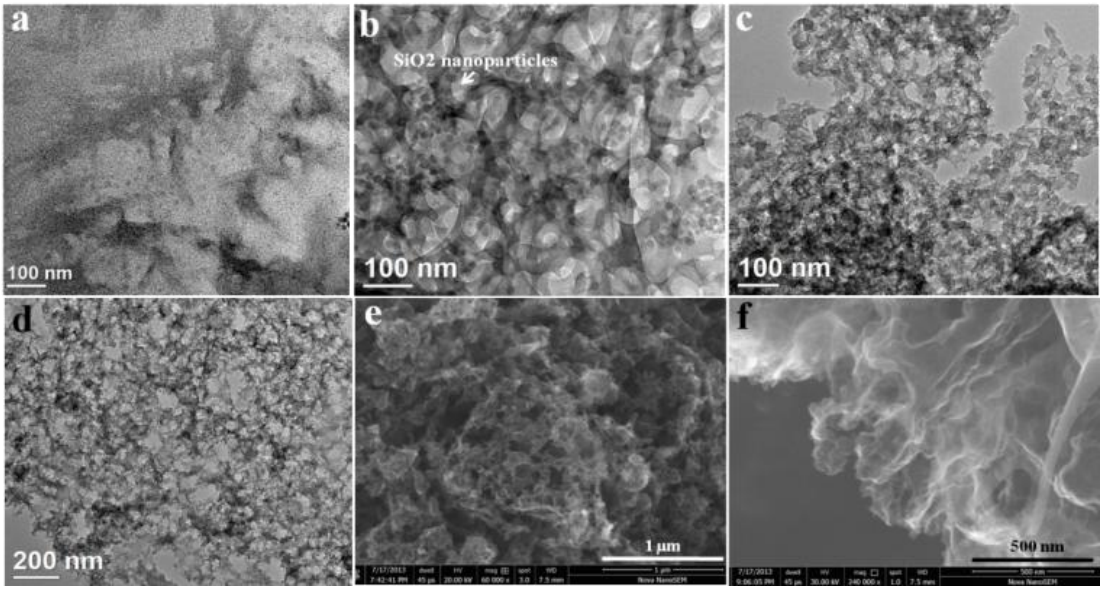

Figure 5.2 *TEM image of pure gram flour powder boiled in water, b) TEM image of SiO2 nanoparticle uptake in the expanded gram flour matrix, c, d) N-doped mesoporous carbon (GFMC3); the best performing catalyst, e) SEM image of the porous carbon (GFMC3), f) FE-SEM image of GFMC3 at higher resolution showing the sheet-like graphitic morphology.*

Total Nutrient Content	Gm (per 100 gm)
Carbohydrates	57
Fats	6
Proteins	**22**
Water	10

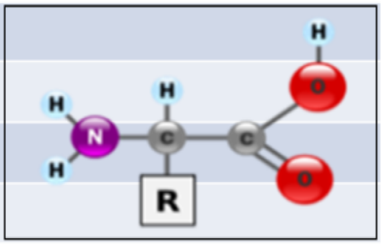

Table 5.2 *Composition of gram flour per 100 gm (adj.) and the general structure of amino acids.*

Transmission electron microscopy (TEM) images (Figure 5.2 c, d) reveal the hierarchically porous structure of the best electrocatalyst, GFMC3 (as discussed later). Field Emission-Scanning Electron Microscopy (FE-SEM) images further confirm the porous structure of this carbon system (Figure 5.2e). Higher resolution FE-SEM

image (Figure 5.2f) shows the sheet like graphitic microstructure of the synthesized carbon catalyst (GFMC3).

X-ray diffraction patterns of GFMC1, GFMC2 and GFMC3 reveal the partially graphitized nature of the carbon formed (Figure 5.3a). This is confirmed by the broad peak obtained at $2\Theta \sim 24.4^0$ corresponds to the (002)-graphite plane and another at $2\Theta \sim 43.7^o$ for the (100) graphite plane.[46] There is a small deviation from the single crystal graphite peaks due to a certain degree of disorder in these materials. The double pyrolysis process ensures a higher degree of graphitization of these carbon species. This further leads to higher electronic conductance of these carbon catalysts. Good electronic conductivity is an essential feature of ORR electrocatalysts as the fast and efficient transport of electrons enhances their performance. Since measuring absolute resistivity of such flaky and porous materials is non-trivial and needs frequency dependent measurements with modelling, we made a simple film based measurement to get a feel of relative differences in electrical properties. Thus 5 mg of each carbon catalyst was mixed with 1 mg of binder (kiner). 1 ml NMP was added and the contents were ground in a mortar pestle to make a uniform thin paste. 7 µL of the paste was drop-cast on 0.5* 0.5 cm of glass slide. Resistance was measured over a distance of 1 mm on a two-probe system. The data is presented in Figure 5.3b. It is seen that the electrical resistance values for the materials obtained by cooking with SiO_2 nanoparticles followed by pyrolysis and acid etching (porous carbons), namely GFMC2 and GFMC3 are lower than that of GFMC1 (processed without SiO_2 addition). For our purpose of electrocatalysis this is a positive factor since concurrent porosity and conductivity increase add to performance enhancement. Introduction of porosity adds edge states and also the processing can modify end groups which could enhance carrier density. Even the forces contributing to stacking of sheets can get modified by porosity. Once again, precise statements on these issues would need much further work which is beyond the scope of this paper.

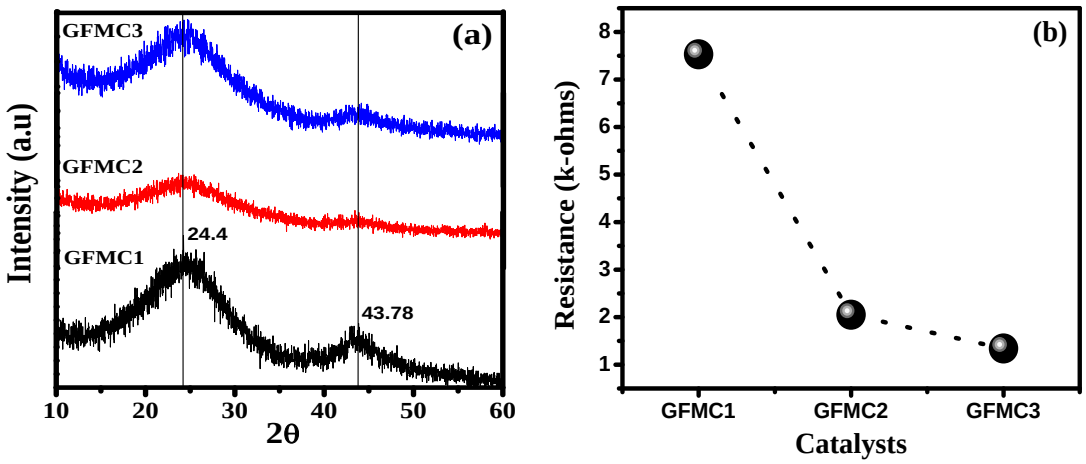

Figure 5.3 *a) XRD patterns of the different carbon catalysts and b) Resistance measurement on carbon films*

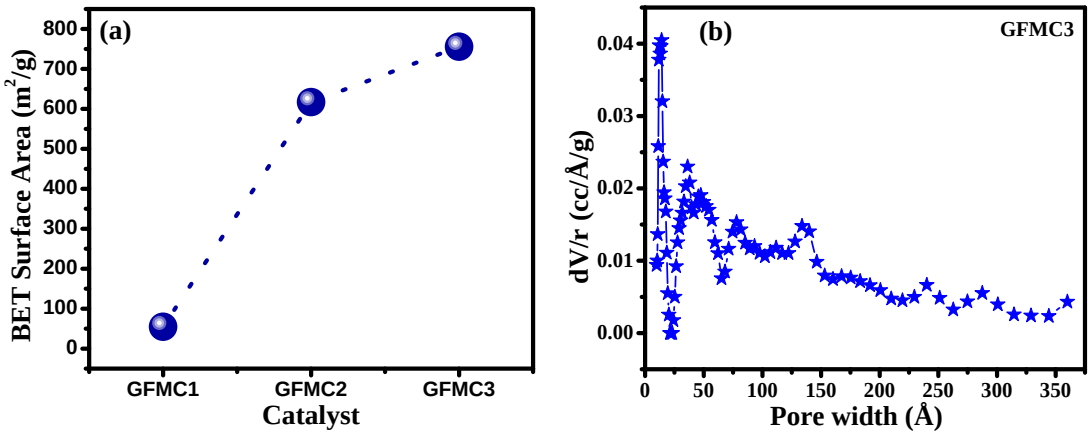

Figure 5.4 *a) BET surface area of the GFMC catalysts b) Pore-size distribution of the high surface area GFMC3*

Two important strategies to improve the efficiency of a carbon catalyst in addition to its high conductivity have been explored previously. They include microscopic structure control and mesoscopic morphology control. Microscopic structure involves the management of dopant heteroatom sites that act as catalytic centers and mesoscopic morphology includes surface area and pore size management.[32] With regard to these required characteristics, we further explored the doping and surface area properties of the carbon materials.

The GFMCs were characterized for surface area using BET measurement (Figure 5.4 a). As expected, it was observed that the surface area exhibited an increasing trend.

GFMC1 showed the lowest area as its synthesis protocol did not involve SiO_2/HF treatment. A very low pore density and an absence of hierarchical porosity were observed in GFMC1. This can be seen in Figure 5.5. With increasing SiO_2 nanoparticle content in the synthesis protocol, the surface area showed an increase. GFMC2 and GFMC3 exhibited a high surface area. However, the increase in the area of GFMC3 (excess ~200 ml ludox used in the synthesis) as compared to GFMC2 (50 ml ludox) is not dramatic. This indicates that the SiO_2 nanoparticle uptake by the grains reaches a saturation point at a certain level.

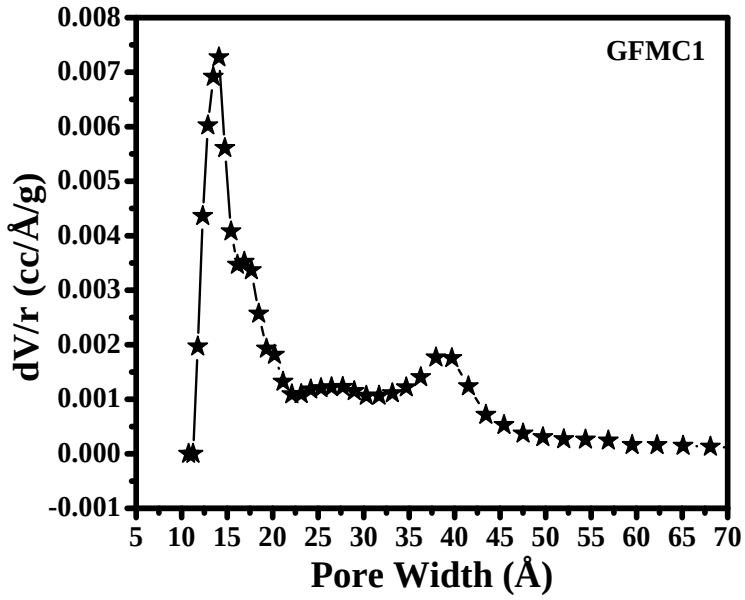

Figure 5.5 *Pore size distribution of GFMC1*

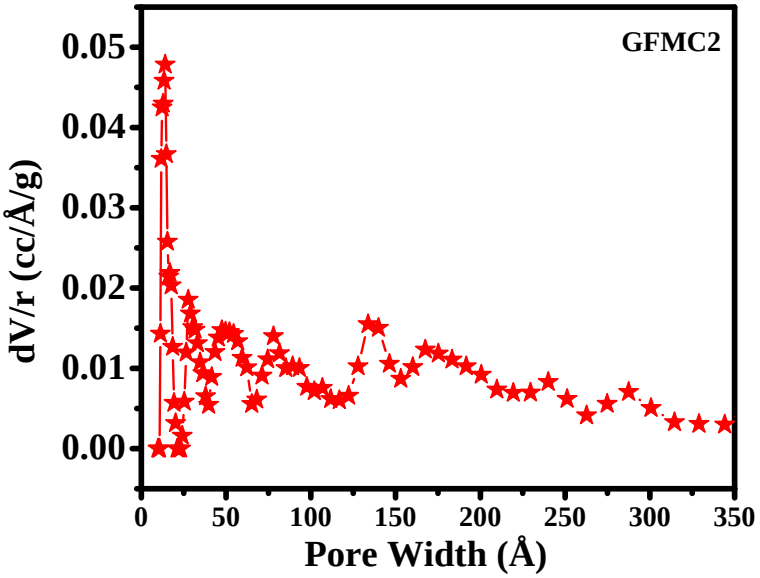

Figure 5.6 Pore size distribution of GFMC2

The pore size distributions for the GFMC2 (Figure 5.6) and GFMC3 (Figure 5.4b) clearly show a wide distribution of pores of several sizes, with the maximum concentration between pore width of (0-2.5 nm). Pores with width ranging from 1 to 30 nm in both these materials confirm a hierarchical pore structure for both these electrocatalysts.

This hierarchical porosity that includes both mesopores and macropores is a very important feature for the material to be an active catalyst for ORR. Studies have established that macropores serve as a reservoir for the electrolyte in order to shorten the diffusion distance of ions inside the material.[32, 47] Mesopores give rise to the higher accessible surface area for ion/charge transport and catalytic action. Since GFMC3 shows the highest surface area along with a hierarchical pore structure, it shows the best electrocatalysis performance towards ORR. The adsorption isotherms for these systems are defined in Figure 5.7.

Adsorption isotherms for GFMCs

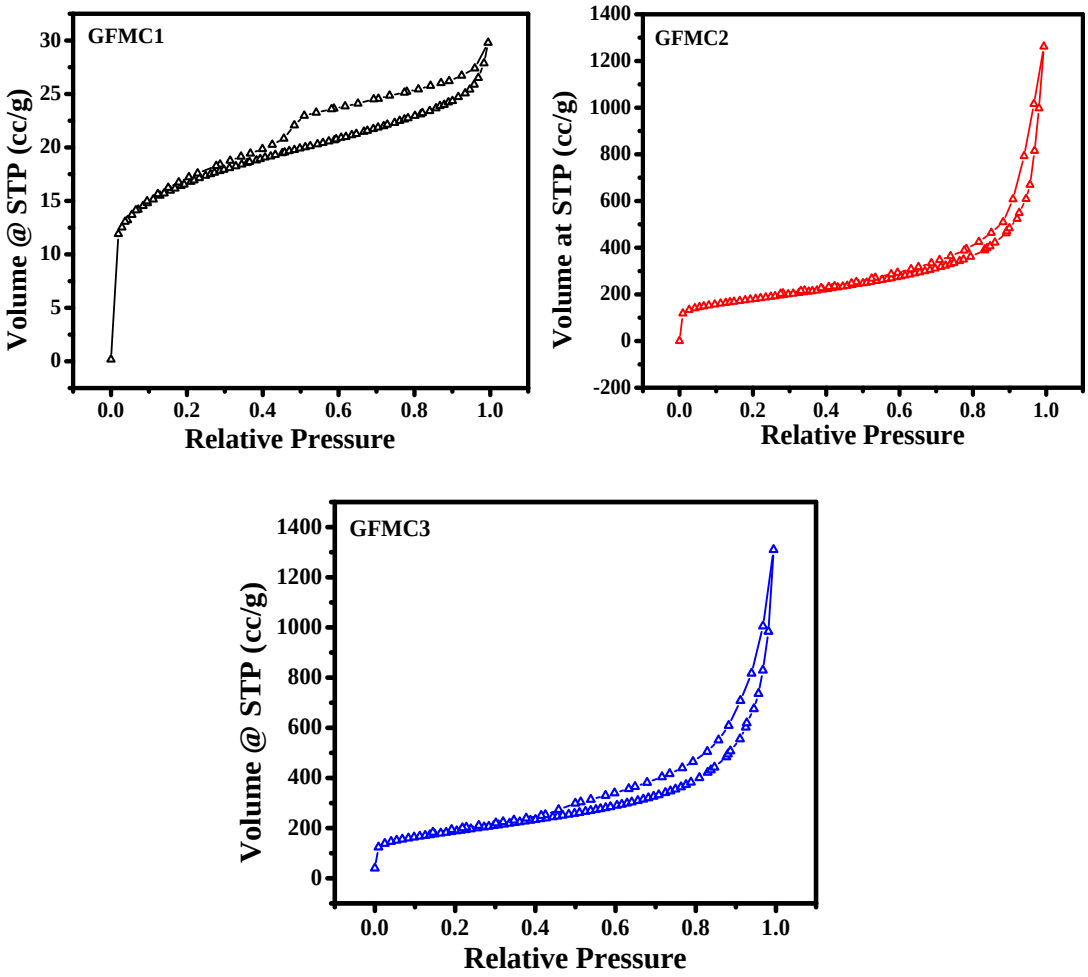

Figure 5.7 *Adsorption isotherms for GFMCs*

All the samples were measured by nitrogen adsorption–desorption experiments at 77 K. All the adsorption isotherms are of type II with typical hysteris loop at high value of p/p^0. Hysteresis loop at high value of p/p^0 signifies microporosity in these materials.

To further determine the atomic composition of electrocatalysts, X-ray Photoelectron Spectroscopy (XPS) was performed on the GFMCs. XPS reveals the presence of C, N and O in the GFMCs. The atomic composition in percentage is shown in the following **Table 5.3**

Material	C	N	O
GMFC1	73.26	1	25.73
GMFC2	84.77	0.75	14.47
GMFC3	88.81	1	10.23

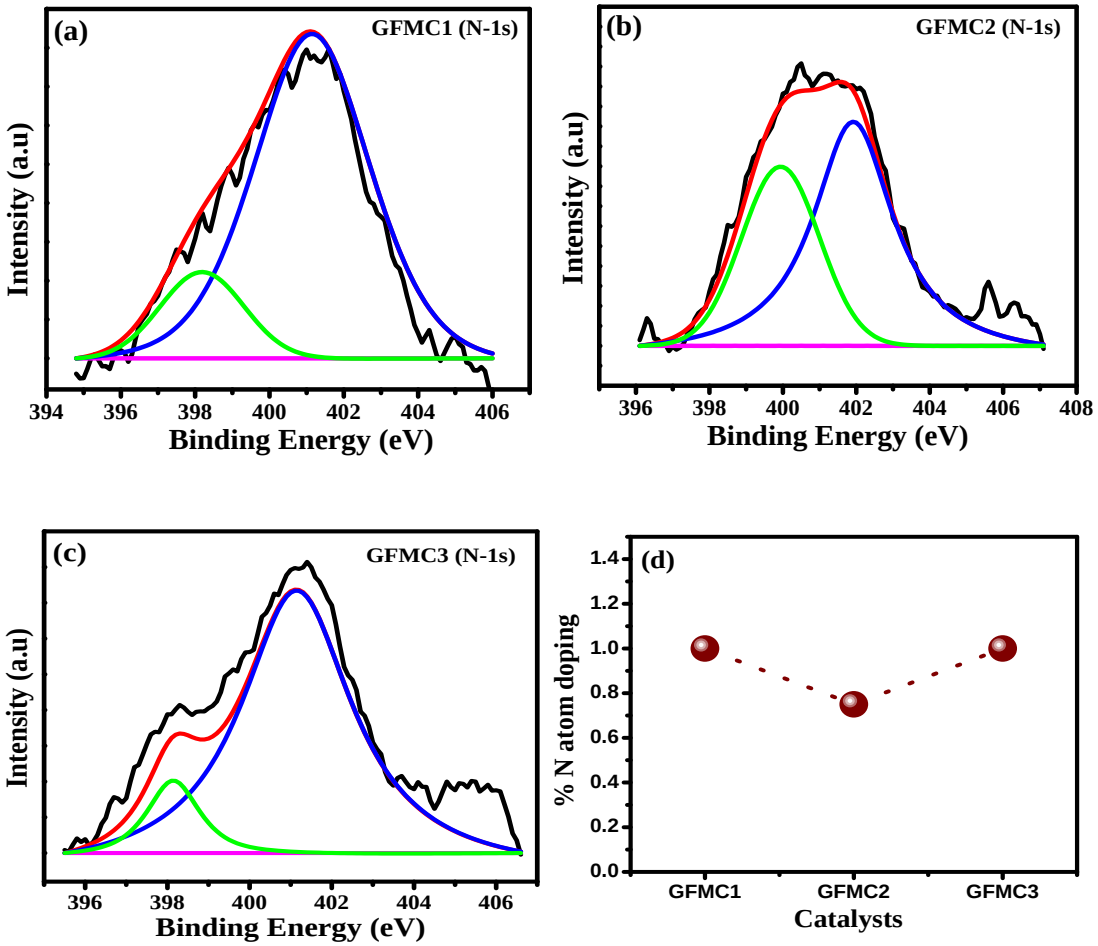

Figure 5.8 *(a,b,c) N1s XPS spectra of GFMC1, GFMC2, GFMC3 respectively and d) N atom doping percentage*

XPS analysis of N content in GFMC1, GFMC2 and GFMC3 was first carried out (Figure 5.8). A doping percentage of ~1 % was observed in these catalytic carbon materials. In each case, the quaternary/graphitic nitrogen peak (401 - 402 eV) is the most intense one. The graphitic nitrogen is the most stable species at pyrolysis temperature above 800^{o}C. The presence of pyrrolic and pyridinic species is also observed to a limited extent in the materials. GFMC1 has pyridinic nitrogen content of ~15.6 % along with 84.4 % of graphitic nitrogen in the total nitrogen content of the material. Similarly, GFMC3 exhibits 11.5 % pyridinic nitrogen content and 88.5 % graphitic nitrogen content.

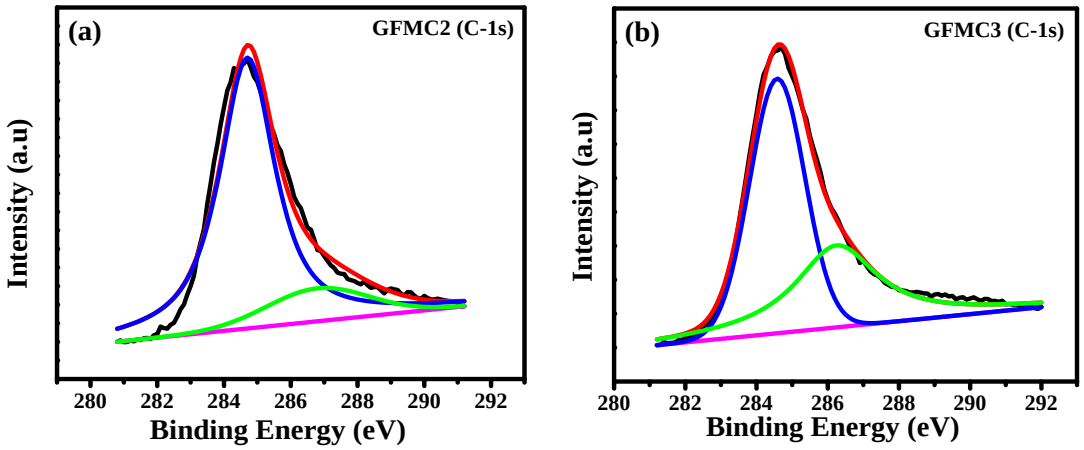

Figure 5.9 *C1s XPS spectra of a) GFMC2 and b) GFMC3*

However, GFMC2 case shows negligible level of pyridinic nitrogen and instead contains 40.2 % of pyrrolic nitrogen in addition to the 59.7 % graphitic N composition. Most studies have indicated that the graphitic nitrogen species possess the highest ORR catalytic potential and are the most active catalytic centers for O_2 adsorption.[34]

Additionally, some reports mention that pyridinic species improve ORR by their role in providing thermodynamically favourable pathways.[34, 48]A high graphitic N content and a moderate doping percentage are realized in our case due to the double pyrolysis synthesis process of the catalysts at temperature of 1000^{o}C in argon atmosphere.

Silva *et. al.* recently reported that pyrolysis in the presence of SiO_2 imparts several oxygen functionalities (eg. C-OH, C=O) to the carbon material.[36] These oxygen dopants/groups in co-ordination with the nitrogen dopants give rise to tautomeric pyridone like groups (-NH-C=O). Such groups impart very strong oxygen reduction catalytic centers to the carbon material. The high oxygen content observed in the XPS of GFMCs indicates significant presence of such oxygen species and catalytic centers. The C1s spectra of GFMC2 and GFMC3 shown in Figure 5.9 point out to the presence of such C-OH/C=O species at peak values of 286.9 and 286.2 eV, respectively, in addition to the sp^2 C=C species (284.7 eV)

To evaluate the electrocatalytic activity of GFMCs towards oxygen reduction, we carried out cyclic voltammetry (CV) of all the three catalysts in oxygen saturated 0.1 M KOH solution with Hg/HgO as the reference electrode. Potentials for all the electrochemical measurements done have been reported with reference hydrogen electrode (RHE) as the reference. This was done by calibration of the Hg/HgO reference electrode in terms of RHE (Figure 5.10).

Conversion of Hg/HgO to RHE

Hg/HgO electrode calibration was carried in a three electrode system with Pt wires as working and counter electrode and Hg/HgO as reference electrode. Hydrogen saturated 0.1 M KOH was used as an electrolyte. Linear sweep voltammetry was performed at 1 mV/s scan rate and the potential at which current crosses zero was taken as thermodynamic potential (vs Hg/HgO) for the hydrogen electrode.

The potential at which current crosses zero is -0.949V vs Hg/HgO

So E (RHE) = E (Hg/HgO) + 0.949

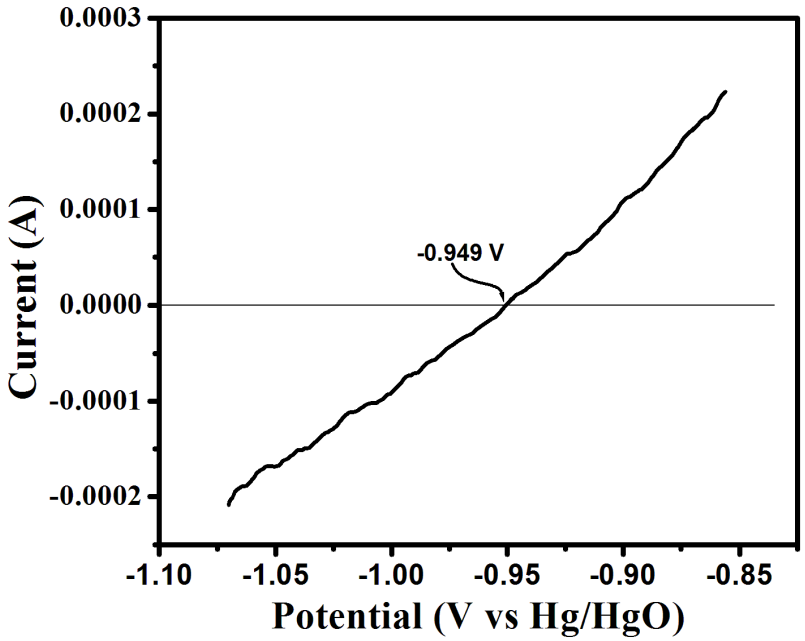

Figure 5.10 *Calibration curve for reference electrode*

In the CV, A graphite rod was as counter electrode, at a scan rate of 5 mV s^{-1}. The amount of GFMC loading (0.255 mg cm^{-2}) was kept constant for all the three samples. From Figure 5.11a, the dioxygen reduction potential for ORR of GFMC3 is seen to be shifted to positive side as compared to GFMC1 and GFMC2. Similarly, double layer charging of GFMC2 and GFMC3 is almost the same. GFMC3 shows a clear reduction peak potential at 0.82 V. Along with the peak potential, GFMC3 also shows prominent reduction current density which is higher than GFMC1 and GFMC2. This improved reduction current density of GFMC3 is mainly attributed to its more active reaction sites and high surface area for proper mass transfer along with good electrical conductivity.

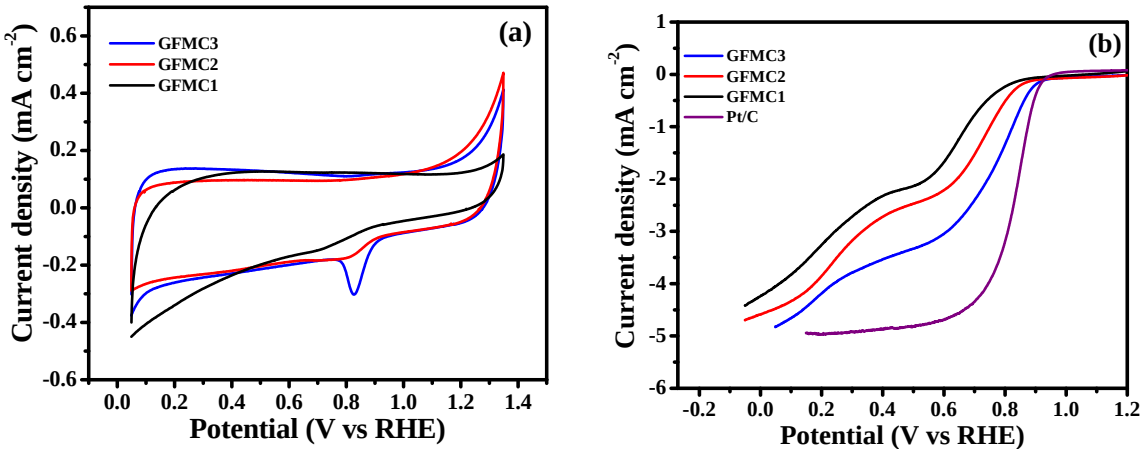

Figure 5.11 a) Cyclic Voltammogram of GFMCs in oxygen saturated 0.1 M KOH at 5 mV s-1 scan rate b) LSV studies of the GFMC catalysts in oxygen saturated 0.1 M KOH with an electrode rotation of 1600 rpm and scan rate is 5 mV s-1. For both experiments, reference electrode was RHE and a graphite rode was used as the counter electrode.

To further elucidate the ORR reaction activities of GFMCs, we carried out linear sweep voltammetry (LSV) using a rotating disc electrode (RDE) in an oxygen saturated 0.1 M KOH at a scan rate of 5 mV s^{-1} and an electrode rotation speed of 1600 rpm (LSV plot shown in Figure 5.11b). Commercially available Pt/C (20 wt %) catalyst was used for comparison. Since the area, particle size and loadings are important parameters for determining the performance of these systems, [49, 50] the details for the catalyst used by us are provided below in Figure 5.12.

Details of commercial Pt/C (20%) used for the comparison of electrochemical performance

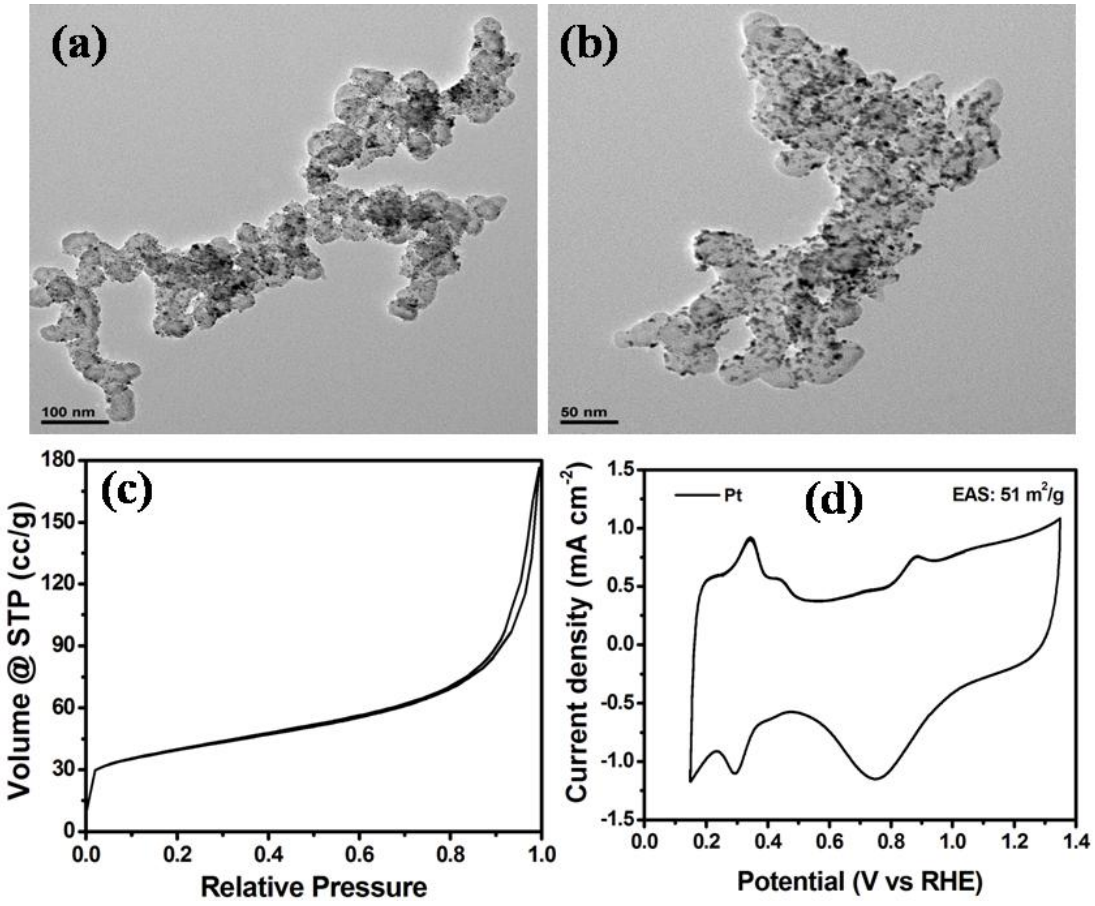

Figure 5.12 *(a) & (b) are the TEM images of Pt/C at different magnification. Pt particle size is varying in between 3 - 5 nm (c) N_2 adsorption isotherm of Pt/C. Calculated BET surface area is 130 m^2/g (d) Cyclic voltammogram of Pt/C at 50 mV/s scan rate in 0.1 M KOH solution. Electrochemical active surface was calculated from the hydrogen desorption area of the voltammogram and it is 51 m^2/g. (Pt loading in the electrode is 25 µg/ cm^2 and area of electrode is 0.196 cm^2).*

From Figure 5.11b, the onset potential of GFMC3, 0.949 V, is seen to be 23 mV lesser than the commercial 20 % Pt/C with a Pt loading of 25 µg cm^{-2} (0.972 V) catalyst. The onset potential of GFMC1, 0.934 V, is 15 mV lesser than GFMC3 and the oxygen reduction current density at 0.4 V is 1.3 and 1.5 times lower than GFMC2 and GFMC3, respectively. In the case of GFMC2, the onset potential 0.926 V shifts

towards more negative as compared to GFMC1 and GFMC3, but its oxygen reduction current density is higher as compared to GFMC1 and lesser than GFMC3. This can be explained by considering the nature and distribution of the active sites on the surface. GFMC2 has higher surface area which creates more active sites as compared to GFMC1. The onset potential was calculated by the process described below in the Figure 5.13.

Onset potential determination

The potential where the reduction current sharply increasing compared to blank is considered as the onset potential for the ORR. (LSV in oxygen saturated 0.1 M KOH at 1600 rpm is given in black and LSV in nitrogen saturated 0.1 M KOH at 0 rpm as blank in red)

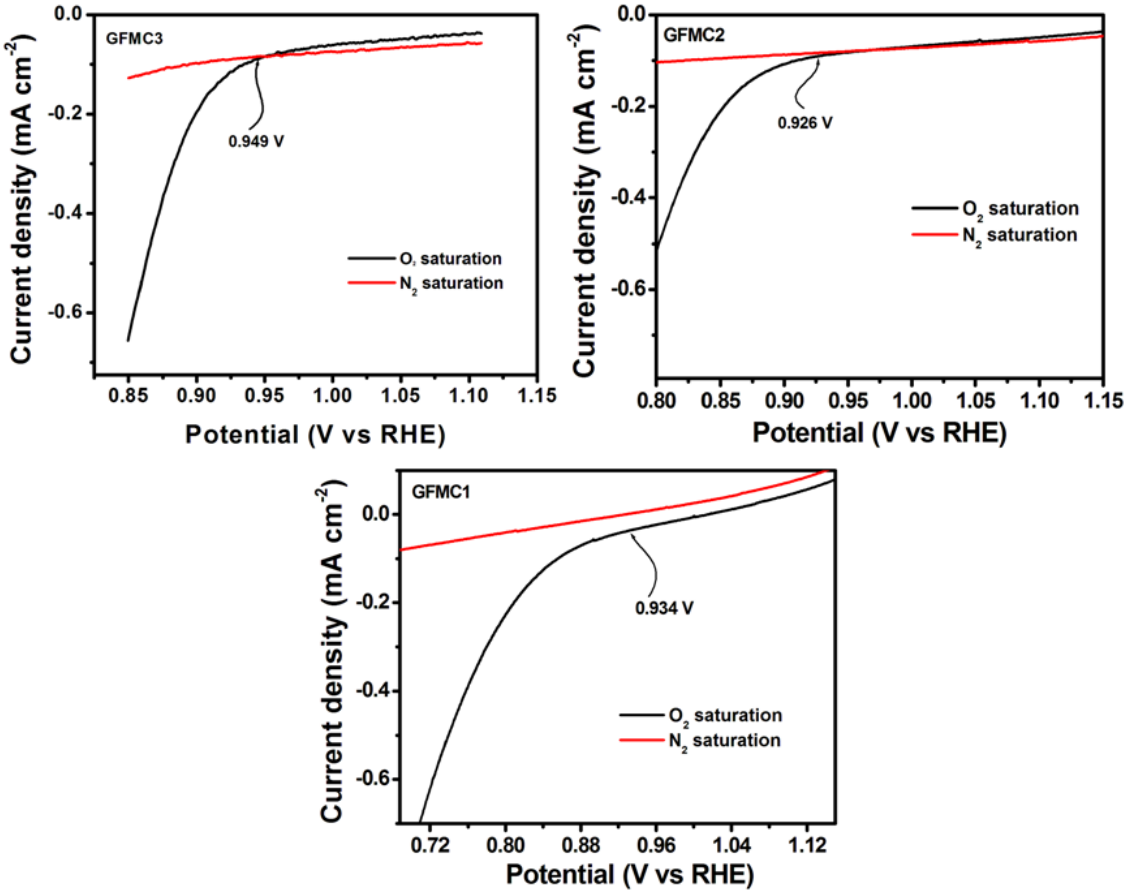

Figure 5.13 *Linear sweep voltammogram of GFMC at rotation at 1600 rpm in an oxygen saturated 0.1M KOH with a scan rate of 5 mV* s^{-1} *(Black) and in nitrogen saturated 0.1 M KOH at zero rotation (Red).*

Similarly, the onset potential of the materials strongly depends on the nitrogen coordination in the carbon matrix. Pyridinic nitrogen content in GFMC1 and GFMC3 shifts the onset potential towards more positive side as compared to GFMC2 which lacks pyridinic nitrogen content.[48] Similarly, half wave potential ($E_{1/2}$) of GFMC3 is higher than that of GFMC1 and GFMC2. Relatively poor electrical conductivity as well as surface area of GFMC1 shifts $E_{1/2}$ towards more negative potential as compared to GFMC2 and GFMC3. Due to improved conductivity, nitrogen coordination and high surface area, GFMC3 shows higher ORR activity compared to GFMC1 and GFMC2. GFMC3 shows onset potential very close to the commercial Pt/C, but $E_{1/2}$ and oxygen reduction current density are lesser as compared to Pt/C. However, both onset potential and $E_{1/2}$ of GFMC3 are higher than GFMC2 and GFMC1, which indicate that both the intrinsic ORR activity as well as number of active reaction centres increases after the two stage annealing with preferred nitrogen coordination and high surface area. [52]

In order to further understand the amount of peroxide formed during ORR, we carried out rotating ring disc electrode (RRDE) study. The ring electrode potential was kept at 1.5 V. The catalyst coated (50 µg) on a 0.24 cm^2 glassy carbon disc having a Pt ring was used as the working electrode, with RHE and graphite rod used as the reference and counter electrodes, respectively, in oxygen saturated 0.1 M KOH solution. With the collection efficiency of the electrode of 0.37 and the percentage of peroxide formation, the electron transfer number was calculated using the equations given below:

$$\mathbf{1}.\ H_2O_2\ (\%) = 200 * \frac{\frac{I_{ring}}{N}}{I_{disc} + \frac{I_{ring}}{N}}$$

$$\mathbf{2}.\ n = \frac{4\ I_{disc}}{I_{disc} + \frac{I_{ring}}{N}}$$

where, I_{ring} is the Faradaic ring current

I_{disc} is the Faradaic disc current

N is the collection efficiency (0.37)

'n' is the number of electron transfer

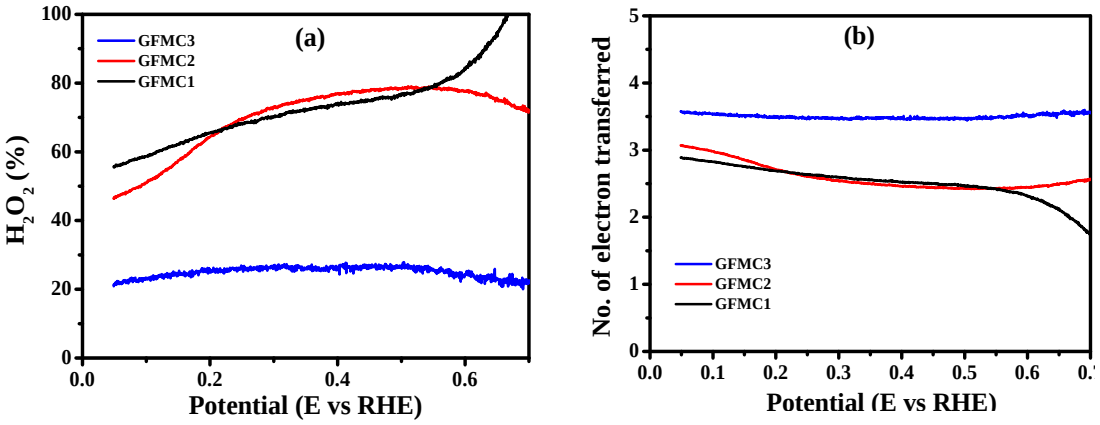

Figure 5.12 *a) Peroxide formation of GFMCs calculated from RRDE analysis at different potential in oxygen saturated 0.1 M KOH at 1600 rpm at 5 mV s^{-1} scan rate b) Number of electron transfer calculated from the percentage of peroxide formed during the reduction.*

Figure 5.12a presents the yield of H_2O_2 produced during oxygen reduction at different potentials. GFMC3 shows less yield of peroxide as compared to the GFMC1 and GFMC2. GFMC3 shows an H_2O_2 yield of ~ 26 %, which gets slowly decreased to 22% at lower potentials. GFMC1, on the other hand, shows a gradual decrease in peroxide yield from higher potentials, reaching a value of 56 % at lower potentials. GFMC2 also displays a high yield of peroxide at higher potentials, decreasing to 46 % at lower potentials. Such a high percentage of peroxide formation in the case of conducting carbon was reported by Lee *et al.*[3] The calculated number of electrons from the H_2O_2 yield is given in Figure 5.12b. From the figure, it is clear that electron transfer number in GFMC3 is 3.5 in the potential range of 0.7 to 0.1 V and this electron transfer number is higher than that in GFMC1 and GFMC2. This indicates that GFMC3 reduces oxygen molecule to $4OH^-$ through a direct pathway. On the other hand, GFMC2 shows a perfect potential dependent electron transfer. At lower potentials, GFMC2 follows a two electron pathway up to 0.3 V, after which the number of electrons transferred increases with higher potentials, reaching to a level corresponding to 3 electron transfer. This indicates that both two electron and four electron pathways concurrently occur in this system as reported by Wang *et al.* [52,53]

Contrary to GFMC2, the ORR over GFMC1 follows a 2-electron pathway for the entire potential range. The large number of active sites and higher electrical conductivity of GFMC3 are presumably acting as the favourable factors for shifting the electron transfer from 2.5 (for GFMC1) to 3.5 from the starting potential itself.

Fuel crossover is one of the major problems of the low temperature polymer electrolyte membrane fuel cells. Liquid fuels such as methanol, ethanol, formic acid etc. can permeate through the membrane and poison the cathode electrocatalyst, thereby reducing the ORR activity. To study the poisoning effect of the catalyst, we carried out chronoamperometric analysis in 0.1 M oxygen saturated KOH with a rotation rate of 1000 rpm at 0.8 V At around 500 s, 3 M methanol was added in the reaction solution in order to study the effect of methanol tolerance (Figure 5.13). In the case of Pt/C, a sharp increase in the oxidation current was observed after the addition of methanol in the reaction solution which clearly indicates the poisoning effect of methanol on Pt. In contrast to Pt, GFMC3 does not show any oxidation current upon the addition of methanol in the reaction mixture. This clearly demonstrates that GFMC3 is highly tolerant towards methanol.

Finally, the durability of GFMC3 and Pt/C was analysed using accelerated durability test (ADT). For ADT, 5000 potential cycling was given in between 0.55 and 1.15 V at a scan rate of 100 mV s^{-1} in oxygen saturated 0.1 M KOH. To understand the stability of the electrocatalyst, LSV was carried before and after ADT with a rotation of 1600 rpm at a scan rate 5 mVs^{-1}. It is established that after ADT the ORR activity of Pt/C decreases dramatically (Figure 5.14). A 35 mV difference in the onset potential and a 0.31 mA cm^{-2} decrease in the limiting current density are observed for Pt/C after the ADT analysis. In contrast to Pt/C, GFMC3 (Figure 5.15) does not show any noticeable change in the onset potential but its oxygen reduction current density increases after ADT. This indicates that more number of active centres are generated so as to reduce oxygen during this process. Chung *et al* as well as Liu *et al* observed a similar kind of behaviour in their recently published work.[51, 54] This stands as clear evidence of the extremely good electrochemical durability of GFMC3 when it functions as the ORR catalyst in an alkaline medium.

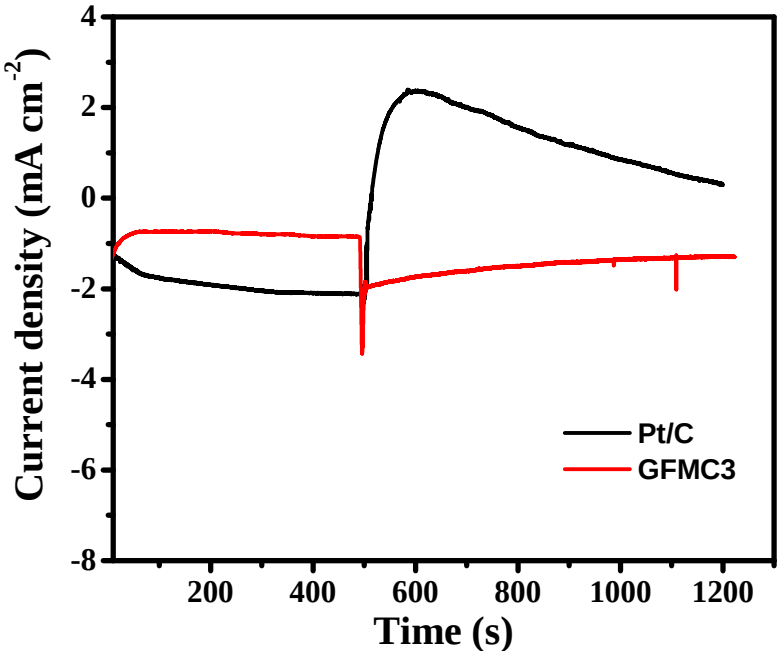

Figure 5.13 *Methanol tolerance studies of GFMC3 at a rotation speed of 1000 rpm in oxygen saturated 0.1 M KOH at 0.8 V. At 500 s, 3 M methanol was added into the electrolyte in order to evaluate the crossover effect.*

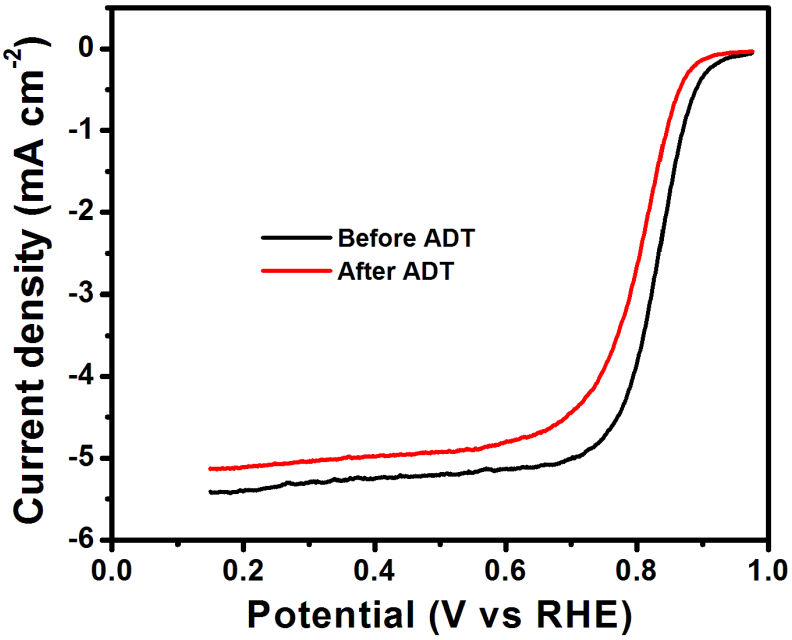

Figure 5.14 *Linear sweep voltammogram of a) Pt/C catalyst at rotation of 1600rpm in an oxygen saturated 0.1M KOH with a scan rate of 5 mV* s^{-1} *before and after 5000 potential cyclinge (Accelerated Durability Test (ADT)).*

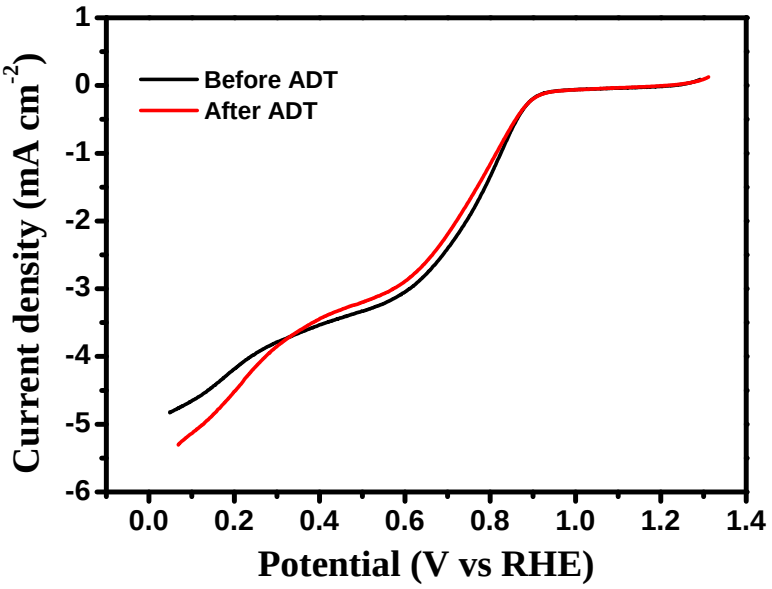

Figure 5.15 *LSV of GFMC3 at rotation of 1600 rpm in an oxygen saturated 0.1 M KOH with a scan rate of 5 mV* s^{-1} *before and after 5000 potential cycling (ADT is accelerated durability test).*

In order to conclusively demonstrate that the precursors used in this work are generic in nature, we also synthesized doped carbon based electrocatalysts using soybean powder as the natural precursor (SBMC1) instead of gram flour. The basic procedure was similar to what was used for GFMC3. Owing to the higher protein content in natural soybean (36.5 % as compared to 22 % in gram flour), as expected, the carbon catalyst obtained from soybean has a higher nitrogen doping percentage (~1.25 % as against 1 % in the case of GFMC samples). However, the surface area for this SBMC1 sample was found to be much lower (28 m^2/g) as compared to GFMC samples. Similarly, the concentration of pores and the conductivity were also lower. This implies that the three parameter space of heteroatom type and concentration, surface area and porosity, and electrical conductivity together needs optimization based on the constitution of the precursor.

SBMC1 as an electrocatalyst for ORR

XPS analysis shows that SBMC1 contains Carbon, Nitrogen and Oxygen in the ratio of 22:1.25:80. Very high oxygen content is observed in this material. A slightly greater % N atom doping (1.25%) is seen in SBMC1. This may be due to increased protein content of the precursor. The nitrogen content shows peaks at 399.7 eV (pyrrolic N), 401.3 eV (graphitic N), 403.3 eV (oxygenated N) (Figure 5.16)

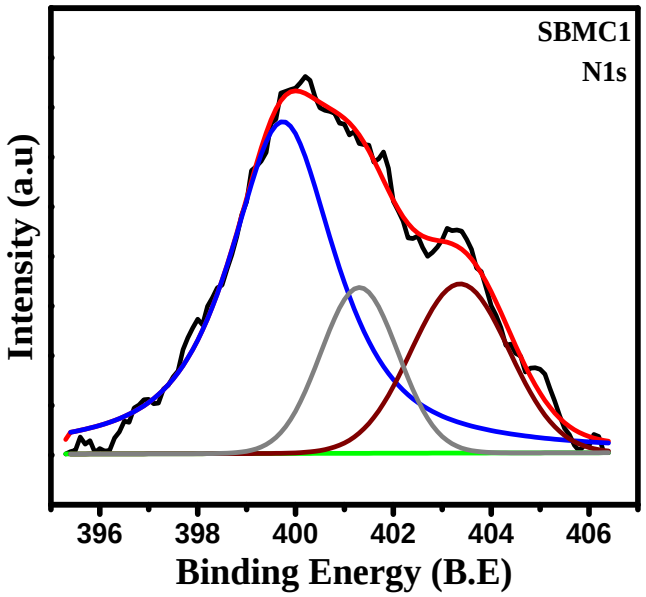

Figure 5.16. *XPS analysis of N1s in SBMC1*

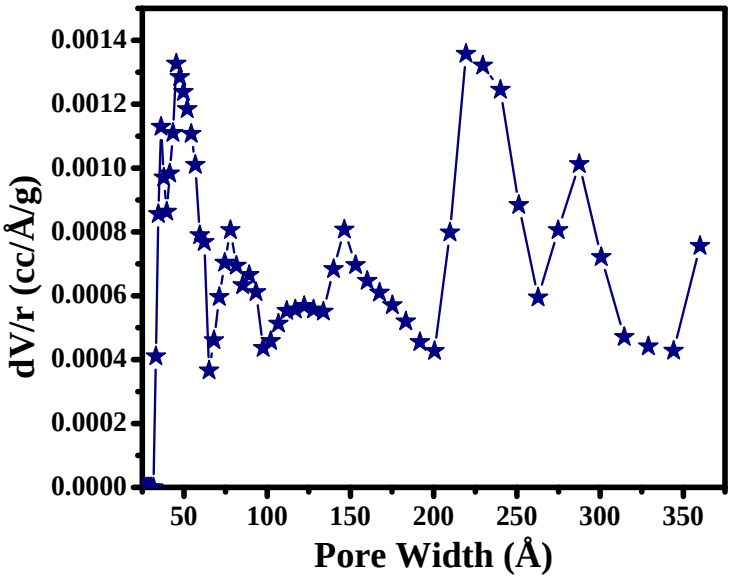

Figure 5.17. *Pore size distribution of SBMC1*

The pore size distribution of SBMC1 shows a similar hierarchical pore distribution which is responsible for enhanced catalytic activity (Figure 5.17). The BET surface area of SBMC1 however is low (28 m^2/g).

This could be due to insufficient penetration of SiO_2 nanoparticles into the seed coat of soybean grains during the synthesis. The resistance of SBMC1 pellet also shows an increase as compared to GFMCs (~ 10.23 ohms). However the good performance in ORR in this case can be attributed to an increased nitrogen doping percentage and oxygen functionalization as compared to GFMCs. It is quite clear that SBMC1 possesses large number of catalytic sites inspite of having lesser surface area and conductivity as compared to GFMC2.

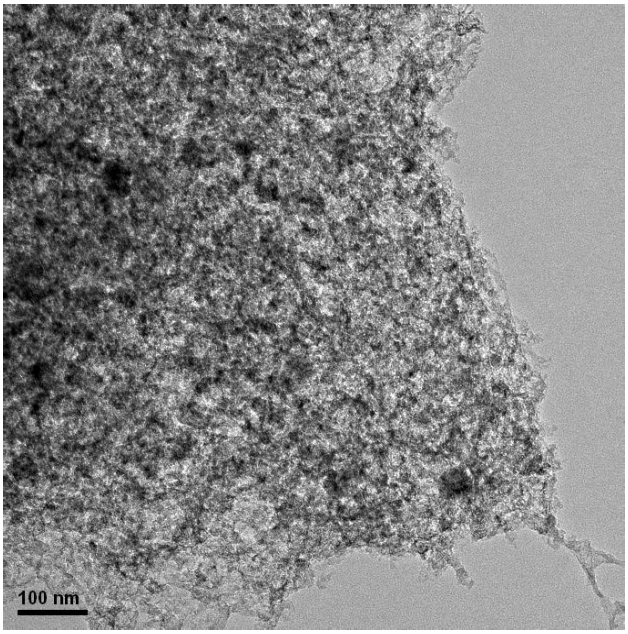

Figure 5.18 *TEM image of SBMC1*

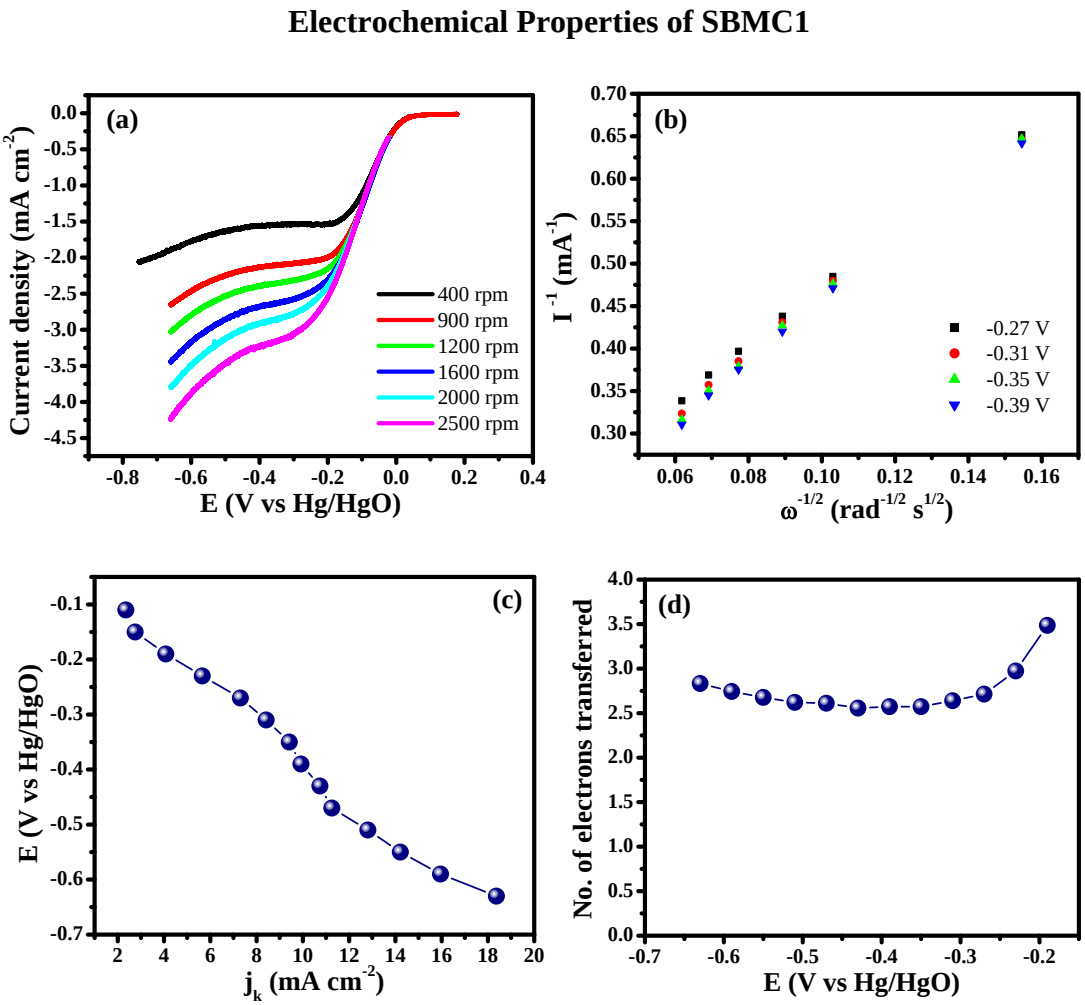

Figure 5.19 *a) LSV studies of the SBMC1 catalysts in 0.1 M oxygen saturated KOH at different electrode rotation with scan rate is 5 mV s^{-1}. Reference electrode is Hg/HgO and graphite rode as counter electrode. b) K-L plots of the SBMC1 at different potential. Plots are derived from the LSV at different rotation speed. c) Kinetic current density of the GFMCs Calculated from the slope of K-L plot d) Number of electron transfer calculated from the slope of K-L plot.*

Figure 5.19 a, shows LSV curves of SBMC1 at different rotation speed with an onset potential of 0.05 V vs Hg/HgO for ORR. SBMC1 also showing excellent ORR activity similar to GFMCs. SBMC1 shows ORR electron transfer number around 3 in the entire potential range. This clearly indicates that SBMC1 follow a mixed kinetics where both peroxide and OH- formation occurs. Electrocatalytic activity of SBMC1

proves pyrolysis of protein enriched food waste is a generalized strategy to synthesize cost effective fuel cell electrocatalyst for ORR.

5.4 Conclusions

We demonstrate novel synthesis and applicability of a metal-free, nitrogen-doped, hierarchically porous, oxygen-functionalized highly-conducting carbon electrocatalyst for oxygen reduction reaction (ORR) in an alkaline electrolyte. The material exhibits remarkable electrocatalytic behaviour due to the synergistic effects of high conductance, hierarchical porosity and heteroatom doping which are simultaneously achieved in the synthesis of this catalyst. The process involves the utilization of a protein rich-food grains, making it a sustainable, potentially large scale alternative for synthesis of an efficient carbon based electrocatalyst in AEMFCs.

References

1. R. Bashyam and P. Zelenay, Nature, 2006, 443, 63-66.
2. R. Jasinski, Nature, 1964, 201, 1212-1213.
3. J.-S. Lee, G. S. Park, S. T. Kim, M. Liu and J. Cho, Angewandte Chemie International Edition, 2013, 52, 1026-1030.
4. B. Winther-Jensen, O. Winther-Jensen, M. Forsyth and D. R. MacFarlane, Science, 2008, 321, 671-674.
5. Y. Zhao, K. Watanabe and K. Hashimoto, Journal of Materials Chemistry A, 2013, 1, 1450-1456.
6. P. Chen, T.-Y. Xiao, Y.-H. Qian, S.-S. Li and S.-H. Yu, Advanced Materials, 2013, 25, 3192-3196.
7. Z. Chen, D. Higgins and Z. Chen, Carbon, 2010, 48, 3057-3065.
8. Z. Chen, D. Higgins, H. Tao, R. S. Hsu and Z. Chen, The Journal of Physical Chemistry C, 2009, 113, 21008-21013.
9. C. H. Choi, S. H. Park and S. I. Woo, Green Chemistry, 2011, 13, 406-412.
10. D. Geng, Y. Chen, Y. Chen, Y. Li, R. Li, X. Sun, S. Ye and S. Knights, Energy & Environmental Science, 2011, 4, 760-764.
11. K. Gong, F. Du, Z. Xia, M. Durstock and L. Dai, Science, 2009, 323, 760-764.
12. D. Higgins, Z. Chen and Z. Chen, Electrochimica Acta, 2011, 56, 1570-1575.

13. H. Li, W. Kang, L. Wang, Q. Yue, S. Xu, H. Wang and J. Liu, Carbon, 2013, 54, 249-257.
14. Z. Lin, M.-k. Song, Y. Ding, Y. Liu, M. Liu and C.-p. Wong, Physical Chemistry Chemical Physics, 2012, 14, 3381-3387.
15. R. Liu, D. Wu, X. Feng and K. Müllen, Angewandte Chemie International Edition, 2010, 49, 2565-2569.
16. Y. Liu, S. Chen, X. Quan, H. Yu, H. Zhao, Y. Zhang and G. Chen, The Journal of Physical Chemistry C, 2013, 117, 14992-14998.
17. Y. Ma, L. Sun, W. Huang, L. Zhang, J. Zhao, Q. Fan and W. Huang, The Journal of Physical Chemistry C, 2011, 115, 24592-24597.
18. T. C. Nagaiah, S. Kundu, M. Bron, M. Muhler and W. Schuhmann, Electrochemistry Communications, 2010, 12, 338-341.
19. J.-i. Ozaki, S.-i. Tanifuji, A. Furuichi and K. Yabutsuka, Electrochimica Acta, 2010, 55, 1864-1871.
20. S. Shanmugam and T. Osaka, Chemical Communications, 2011, 47, 4463-4465.
21. Z.-H. Sheng, L. Shao, J.-J. Chen, W.-J. Bao, F.-B. Wang and X.-H. Xia, ACS Nano, 2011, 5, 4350-4358.
22. H. Wang, T. Maiyalagan and X. Wang, ACS Catalysis, 2012, 2, 781-794.
23. S. Wang, D. Yu, L. Dai, D. W. Chang and J.-B. Baek, ACS Nano, 2011, 5, 6202-6209.
24. Z. Wang, R. Jia, J. Zheng, J. Zhao, L. Li, J. Song and Z. Zhu, ACS Nano, 2011, 5, 1677-1684.
25. W. Y. Wong, W. R. W. Daud, A. B. Mohamad, A. A. H. Kadhum, K. S. Loh and E. H. Majlan, International Journal of Hydrogen Energy, 2013, 38, 9370-9386.
26. J. Wu, D. Zhang, Y. Wang and B. Hou, Journal of Power Sources, 2013, 227, 185-190.
27. Z. Yang, Z. Yao, G. Li, G. Fang, H. Nie, Z. Liu, X. Zhou, X. a. Chen and S. Huang, ACS Nano, 2012, 6, 205-211.
28. Z. Yao, H. Nie, Z. Yang, X. Zhou, Z. Liu and S. Huang, Chemical Communications, 2012, 48, 1027-1029.
29. L. Zhang and Z. Xia, The Journal of Physical Chemistry C, 2011, 115, 11170-11176.
30. H. Zhong, H. Zhang, Z. Xu, Y. Tang and J. Mao, ChemSusChem, 2012, 5, 1698-1702.

31. Z. Lin, G. H. Waller, Y. Liu, M. Liu and C.-p. Wong, Carbon, 2013, 53, 130-136.
32. Z. Liu, H. Nie, Z. Yang, J. Zhang, Z. Jin, Y. Lu, Z. Xiao and S. Huang, Nanoscale, 2013, 5, 3283-3288.
33. A. Morozan, P. Jégou, M. Pinault, S. Campidelli, B. Jousselme and S. Palacin, ChemSusChem, 2012, 5, 647-651.
34. Z. Yang, H. Nie, X. a. Chen, X. Chen and S. Huang, Journal of Power Sources, 2013, 236, 238-249.
35. Y. Zheng, Y. Jiao, M. Jaroniec, Y. Jin and S. Z. Qiao, Small, 2012, 8, 3550-3566.
36. R. Silva, D. Voiry, M. Chhowalla and T. Asefa, Journal of the American Chemical Society, 2013, 135, 7823-7826.
37. S. Chen, J. Bi, Y. Zhao, L. Yang, C. Zhang, Y. Ma, Q. Wu, X. Wang and Z. Hu, Advanced Materials, 2012, 24, 5593-5597.
38. J. Liang, Y. Jiao, M. Jaroniec and S. Z. Qiao, Angewandte Chemie International Edition, 2012, 51, 11496-11500.
39. Z. Lin, G. Waller, Y. Liu, M. Liu and C.-P. Wong, Advanced Energy Materials, 2012, 2, 884-888.
40. Z. Liu, G. Zhang, Z. Lu, X. Jin, Z. Chang and X. Sun, Nano Research, 2013, 6, 293-301.
41. S. Wang, L. Zhang, Z. Xia, A. Roy, D. W. Chang, J.-B. Baek and L. Dai, Angewandte Chemie International Edition, 2012, 51, 4209-4212.
42. S.-A. Wohlgemuth, T.-P. Fellinger, P. Jaker and M. Antonietti, Journal of Materials Chemistry A, 2013, 1, 4002-4009.
43. D.-S. Yang, D. Bhattacharjya, S. Inamdar, J. Park and J.-S. Yu, Journal of the American Chemical Society, 2012, 134, 16127-16130.
44. C. Zhang, N. Mahmood, H. Yin, F. Liu and Y. Hou, Advanced Materials, 2013, 25, 4932-4937.
45. S. Kaur, N. Singh, N. S. Sodhi and J. C. Rana, Food Chemistry, 2009, 117, 282-289.
46. Z. Q. Li, C. J. Lu, Z. P. Xia, Y. Zhou and Z. Luo, Carbon, 2007, 45, 1686-1695.
47. Z. Chen, W. Ren, L. Gao, B. Liu, S. Pei and H.-M. Cheng, Nat Mater, 2011, 10, 424-428.
48. L. Lai, J. R. Potts, D. Zhan, L. Wang, C. K. Poh, C. Tang, H. Gong, Z. Shen, J. Lin and R. S. Ruoff, Energy & Environmental Science, 2012, 5, 7936-7942.

49. K. Mayrhofer, B. Blizanac, M. Arenz, V. Stamenkovic, P. Ross, N. Markovic, J. Phys. Chem. B 2005, 109, 14433–14440.
50. K. Mayrhofer, D. Strmcnik, B. Blizanac, V. Stamenkovic, M. Arenz, N. Markovic, Electrochim. Acta 2008, 53, 3181–3188
51. H. T. Chung, J. H. Won and P. Zelenay, Nat Commun, 2013, 4, 1922
52. S. Wang, D.Yu, L. Dai, D.-W. Chang, J.-B. Baek, ACS Nano, 2011, 5, 6202-6209
53. S. Wang, D. Yu and L. Dai, J. Am. Chem. Soc., 2011, 133, 5182–5185
54. J. Liu, X. Sun, P. Song, Y. Zhang, W. Xing and W. Xu, Advanced Materials, 2013

Chapter 6

Oligomer salt derived 3D, heavily nitrogen doped, n-layer graphene cages for Li-ion hybrid electrochemical capacitors application

3D high surface area n-layer graphene cages are seen to form via self assembly of porous graphene sheets by direct pyrolysis of an oligomer salt tailored for the realization of molecular level activation. The oligomer salt was derived from 4-amino benzoic acid as the monomer by a facile free radical polymerization process. Incorporation of the functional groups (-COONa) eliminate the need for any external activating agents (KOH, $ZnCl_2$ etc.) and also render high degree of sub-nanoscale homogeneity. This oligomer derived carbon (ODC) exhibits efficient performance in non-aqueous charge storage application namely Li-ion hybrid electrochemical capacitor (Li-HEC) owing to its high surface area, 3D interconnectivity and an appropriate pore size distribution. The Li-HEC fabricated with ODC based electrodes delivered a maximum energy density of ~63 Wh kg^{-1} with spinel $Li_4Ti_5O_{12}$ as the anode.

6.1 Introduction

Porous conducting carbons for application in energy storage devices like supercapacitors and batteries have been derived from several natural sources by heat treatment and use of specific activation processes involving chemical and physical means. [1-5] Although activation provides a generalized protocol to induce structural modifications like micro and meso-porosity in a material, this method is not suitable for fine tuning of carbon materials to achieve a desired morphology with appropriate structural, physical and chemical properties. It is for this reason that there has been some exploration of polymers as precursors for the synthesis of functional carbon. [6-14] Polymers offer a unique platform for precursor tunability in order to obtain the desired final products for targeted applications. Despite the stated possibility of multiple advantages offered by this methodology, only a limited amount of work has been carried out in this research area.

Chemical activation strategy using KOH was employed to synthesize hierarchically porous carbon from poly-pyrrole microsheets by Qie et al. [15] and activated carbon (AC) from polypyrrole precursors by Wei et al. [16] Silica hard templating strategies to generate high surface area carbon from polymers have also been utilized. [17] Wang et al. [18] synthesized a high surface area nitrogen enriched ordered mesoporous carbon by direct pyrolysis of soft-templated polymeric composites in ammonia atmosphere for application as capacitive material. Zhong et al. [19] synthesized nanoporous carbon from the co-polymer of polyacrylonitrile and a sacrificial block, poly (*n*-butyl acrylate), wherein a high pseudo-capacitance was observed due to a large N dopant concentration in the carbon. A novel strategy for obtaining 3D porous carbon from alkali metal salts of commercially available polymers: polymer poly(4-styrenesulfonic acid-co-maleic acid) sodium salt and poly(acrylamide-co-acrylic acid) potassium salt was successfully adopted by Yadav et al. [20] and Puthussery et al. [21, 22] respectively. However till date, most of the research work on polymer derived carbon involves use of activation/templating protocols or the use of commercially available expensive polymers.

3D graphene based architectures have assumed significance in recent days due to their potential for high surface area, an established structural framework that contributes to electrical interconnectivity and superior charge storage properties. [15, 20, 22-26] In this

work, we demonstrate a tailored synthesis of 3D, n-layer and N-doped graphene sheet assembled cage type morphology by a direct one-step pyrolysis of an oligomer salt. This precursor is a short chain polymer generated by the free radical polymerization of 4-amino-benzoic acid. This 3D carbon formation process does not require any templating/external activation process but instead involves the use of specific functional groups which give rise to an *in-situ* molecular level activation and graphene-sheet formation. Interestingly, the sheets formed during the pyrolysis process assemble themselves in n-layer graphene assembly giving rise to high surface area functional carbon at a temperature as low as 800^{o}C. Moreover the presence of nitrogen atoms in the precursor concurrently dopes the carbon at a high N concentration. This high surface area graphene n-layer stacking assembly exhibits a micro and meso-pore size distribution thereby enabling the material to exhibit efficient electrochemical charge storage performance in non-aqueous electrolytes. Heavy nitrogen doping is also a plus in this context. The porous n-layer, N-doped graphene cage morphology synthesized in this work is termed as oligomer derived carbon (ODC) in the chapter.

We used the ODC as the positive electrode for the construction of high energy density electrochemical storage device, Li-ion hybrid electrochemical capacitor (Li-HEC). Utilization of aqueous electrolyte is the general choice for the electrolyte solution in Li-HEC, but unfortunately the water splitting issue at ~1.23 V limits the possible usage to achieve higher energy density. Hence, organic electrolyte is the only available option for the fabrication of such Li-HEC. Generally, Li-HEC shows the combined advantages of two well-known electrochemical energy storage devices like supercapacitor and Li-ion battery (LIB). Therefore, Li-HEC is capable of delivering high energy density than supercapacitors and high power density than LIB. Originally, the concept of integrating such power systems in non-aqueous medium was proposed by Amatucci et al. [27] In principle, Li-HEC is fabricated with high surface area carbonaceous materials i.e. supercapacitor component along with Li-intercalating material i.e. battery type as counter electrode. [28]

Because of the concurrent high energy and power capability, the Li-HEC is expected to power zero emission transportations like electric vehicles and plug-in hybrid electric vehicles in the future. Although, several Li-insertion materials have been proposed for Li-HEC, $Li_4Ti_5O_{12}$ remains attractive because of its salient features like

lower insertion potential (~1.5 V *vs.* Li), no volume variation during Li-insertion/extraction ("zero-strain" host), high reversibility *i.e.* columbic efficiency (>99%), appreciable capacity (~175 mAh g^{-1}), eco-friendliness etc. [29-36] But unfortunately very few efforts have been put into the development of counter electrodes *i.e.* carbon based electrodes for enhancement in the performance of Li-HEC. [21, 37-40] In this scenario, by realizing the specific advantages offered by ODC, we employed this material for the supercapacitor component in a Li-HEC configuration with $Li_4Ti_5O_{12}$ as counter electrode in an organic medium. Extensive physico-chemical and electrochemical studies were performed and are described in detail. In addition, ODC based symmetric supercapacitor was also fabricated and tested in the same organic medium for the sake of comparison.

6.2 Experimental

6.2.1 Synthesis of the oligomer and its sodium salt:

First, 4-amino benzoic acid (8.7 g, 64 mmol) was dissolved in 1400 ml de-ionized (DI) water and sonicated for 15-20 min. Separately, ammonium persulfate (APS) (14.7 g, 64 mmol) was dissolved in 200 ml DI water and sonicated for 5-10 mins. The APS solution was gradually added dropwise into the 4-amino benzoic acid solution under constant stirring. The solution mixture turns dark in colour after few minutes. The reaction was kept for 48 h under constant stirring condition. The solution was then filtered through a 0.2 µm pore-size poly-tetrafluoroethylene (PTFE) membrane under vacuum. The solid filtrate was collected and re-dispersed in 200 ml DI water. 64 mmol (equimolar to the monomer) sodium hydroxide (NaOH) pellets were added to this solution and kept under constant stirring for 12h. The entire solution was then kept for drying in a vacuum oven at 120 ^oC for 12-18 h. The resultant dried flakes of sodium salt of the oligomer were crushed and used as such for further studies.

6.2.2 Synthesis of the ODC:

The oligomer salt was pyrolyzed at 800 ^oC for 3 h with temperature ramp of 10 degrees per minute under Argon flow. The obtained carbon was washed in dil. HCl by sonication and filtered through a 0.2 µm pore-size PTFE membrane under vacuum. The obtained carbonaceous product was washed by DI water for several times. Then it

was dried in an oven and then used for characterization studies. Synthesis of chemically converted graphene (CCG) for comparison of the data was carried out by a previously reported method. [41]

2.3 Characterization:

Powder X-ray diffraction (XRD) measurements were performed using Philips X'Pert PRO equipped with Cu K_α radiation. Raman spectra were collected from micro-Raman spectrometer (Horiba-JY T64000) in a backscattering configuration with an excitation wavelength of 532 nm with a power of 1 mW. A matrix-assisted laser desorption/ionization (MALDI-MS) study of the sample was done on an AB SCIEX TOF/TOF5800 instrument. For the measurements 5 µl of the sample was mixed with 20 µl of the αCHCA matrix. Fourier transform infrared (FTIR) spectroscopy was done in transmission mode using a Nicolet Magna IR-750 spectrophotometer. Thermogravimetric analysis (TGA) was also carried out on the sample. Field emission scanning electron microscope (FE SEM) (FEI, NOVA NANO SEM) was used to study the morphological features of the synthesized carbonaceous material. The internal structure was examined by high resolution transmission electron microscope (HR-TEM, JEM-2010, JEOL USA Inc.). Element determination was carried out by X-ray photoelectron spectroscopy (XPS) (ESCA-3000, VG Scientific Ltd. England with a 9 channeltron CLAM4 analyzer under vacuum better than 1 108Torr, using Al Ka radiation (1486.6 eV) and a constant pass energy of 50 eV). The surface area of carbon was obtained from Brunauer, Emmett and Teller (BET) surface area measurements (Quantachrome Quadrasorb automatic volumetric instrument). All the electrochemical studies in non-aqueous medium were performed using CR 2016 coin-cell configuration. For the single electrode studies, the composite electrode was formulated with accurately weighed 5 mg of ODC, 1 mg of Super P and 1 mg of teflonized acetylene black (TAB-2) binder. They were mixed using mortar and pestle to form the homogeneous film using ethanol and then pressed over a stainless steel mesh (area of 200 mm^2 with 0.25 mm thickness, Goodfellow, UK) which served as a current collector. The test cells were fabricated with the mentioned composite electrode along with metallic Li counter electrode (0.59 mm thick) which were separated by Whatman paper (Cat. No. 1825-047, UK) and filled with 1M $LiPF_6$ in ethylene carbonate (EC): di-ethyl carbonate (DEC) (1:1, BASF, Germany) as

electrolyte solution. For the case of Li-HEC assembly, the same preparation procedure was repeated for the fabrication of $Li_4Ti_5O_{12}$ and ODC electrodes with different mass loadings (exact mass loading was described in the later sections). Cyclic voltammogram was recorded using Solartron, 1470E and SI 1255B impedance/gain-phase analyzer coupled with a potentiostat. Galvanostatic cycling studies were performed for single electrode and Li-HEC configurations using an Arbin 2000 battery tester at room temperature.

6.3 Results and Discussion

The free radical polymerization of amine containing aromatic rings using APS as the radical initiator is a known technique which is generally used in the synthesis of polyaniline from aniline precursors. [42-46] In this work, we used this free radical polymerization technique to generate short chain polymers from 4-amino-benzoic acid. MALDI-MS studies were performed on the synthesized polymerized product. The spectrum (Figure 6.1) shows the highest molecular peak at 821 (m/z value). Since the molecular weight of the precursor is ~ 137 g mol^{-1}, the number of monomer units in the polymerized product is ~6. This data clearly points to the formation of short chain oligomers with differing chain lengths.

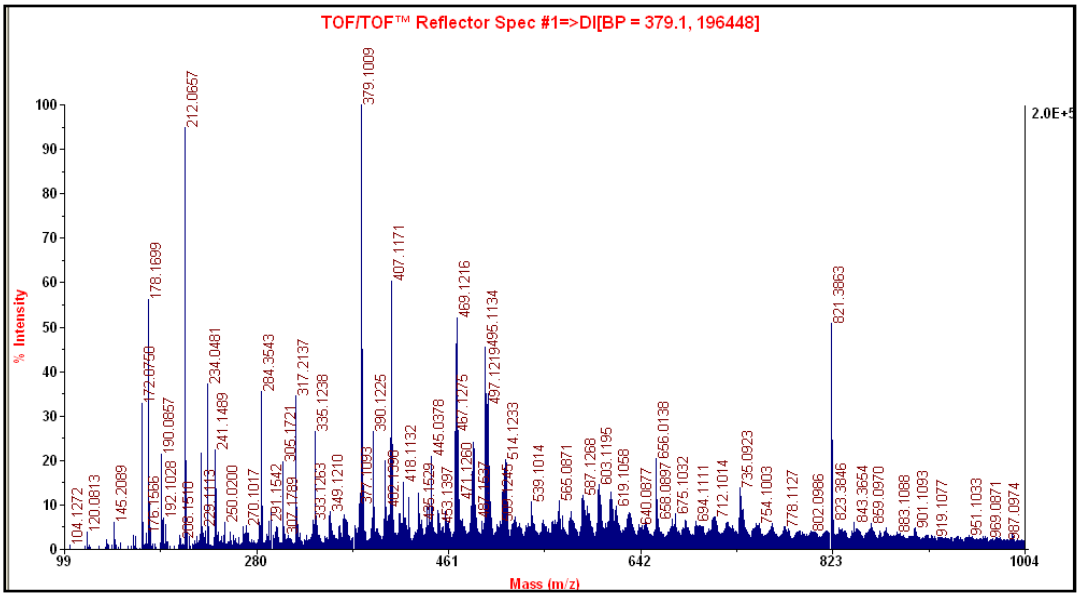

Figure 6.1 *MALDI MS of the PABA oligomer with Alpha cyano 4-hydroxycinnamic (α-CHCA) acid as the matrix*

- The main peaks represented by the α-CHCA matrix are at m/z value of: 164, 195, 172, 379, 212, 294.
- Hence the peaks appearing at the m/z value of 379 and lower can be attributed to the matrix.
- Most other regions than that included in the range of the above data do not exhibit any peaks.
- The peak at 821 is the most significant and the probable molecular peak of the short chain polymer.
- Rest of the low intensity peaks could be due to the fragment formation of the product molecule or the formation of smaller molecules during the reaction

FTIR spectrum (Figure 6.2a) gives further confirmation with regard to the obtained product. The peaks at 3226, 3364 and 3464 cm^{-1} arising due to the primary N-H groups in the monomer 4 amino-benzoic acid disappear in the polymer indicating the formation of the oligomer at the N atom centre. However, a broad residual peak of the monomer is observed at 2922 cm^{-1} in the oligomeric system. This arises due the O-H vibration in the unreacted –COOH groups in the product. The peak at 1671 cm^{-1} is observed because of the C=O bond of the COOH group in 4-amino-benzoic acid. Due to the formation of the sodium salt (-COONa) in our final oligomeric product the C=O group now shifts to 1550 cm^{-1}. The 1600 cm^{-1} peak commonly observed in the monomer and the final product arises due to the aromatic C=C bond. The aromatic amine C-N peak observed at 1290 cm^{-1} in the monomer is shifted towards lower energies (at 1267 cm^{-1}) due to additional conjugation with another aromatic ring in the polymeric structure.

TGA (Figure 6.2b) of the carbonization process of the sodium salt derived from 4-amino-benzoic acid oligomer in inert atmosphere provides an insight into the formation of the porous n-layer graphene. The minor weight loss observed up to 300 ^{o}C is due to the removal of moisture from the precursor. Carbon formation starts taking place from 300-400 ^{o}C which is indicated by the rapid weight loss observed in this range. This weight loss results from the evaporation of volatile organic products and other gaseous impurities. Higher temperature treatment shows a gradual decrease in weight due to graphitization.

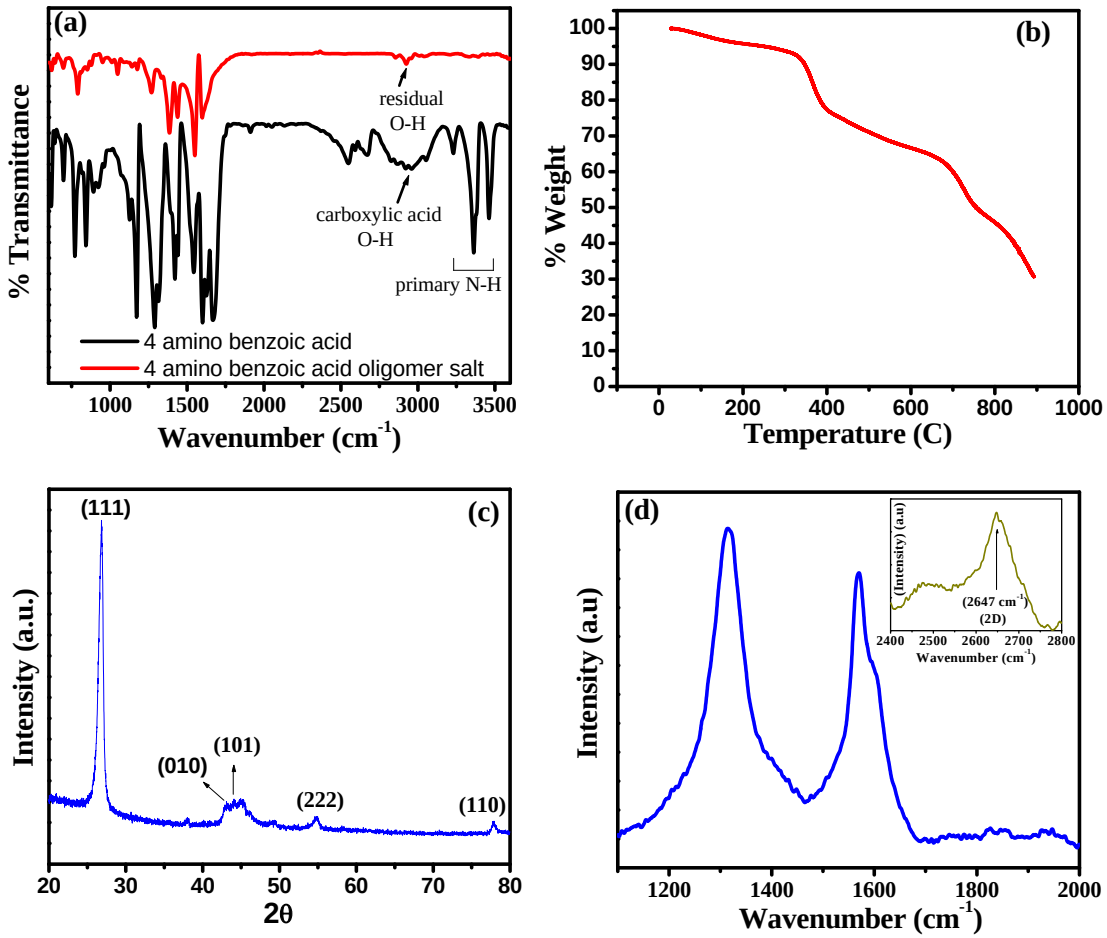

Figure 6.2 *(a) FTIR spectrum of 4-amino-benzoic acid (monomer) and the sodium salt of its oligomer; (b) TGA of the polymer carbonization process in inert atmosphere; (c) XRD pattern of the ODC sample; (d) Raman spectrum of the ODC sample.*

XRD analysis (Figure 6.2c) of the ODC clearly indicates the presence of a highly crystalline graphite phase (hexagonal) with the presence of the rhomb-center as well as the primitive lattices. The reflection at ~26.8 corresponds to the (111) plane of the rhomb-centered lattice in the hexagonal phase. The reflections at 43.16 and 44.09 correspond to the 010 (rhomb-center lattice) and 101 (primitive lattice) planes, respectively. Finally, the peaks at 54.8 and 77.8 indicate the presence of the (222) and (110) planes of the rhomb-center lattice. The crystallite size values were calculated from the Scherrer formula ($\tau = K\lambda/\beta \cos\theta$) and found to be about 12 nm (which

corresponds to 33-34 graphitic monolayers). It is well established that with decreasing particle/crystallite size a peak broadening effect is observed in XRD giving rise to an increasing full-width at half maximum (FWHM) value. From the Figure 6.3 (giving the comparison of ODC with commercial graphite and chemically exfoliated graphene) it is observed that the peak for ODC at 2θ=26.8 is broader (FWHM 2θ = 0.7) than the peak for commercially obtained graphite (FWHM 2θ =0.39) indicating the decreased dimensions of the graphite crystallite. The peak however has a much lower FWHM as compared to the corresponding broad peak (between 20-25) observed in chemically obtained few layer graphene indicating the perfect stacking of carbon layers to form crystalline n-layer graphene nanoparticles with 'n' of about 33-34.

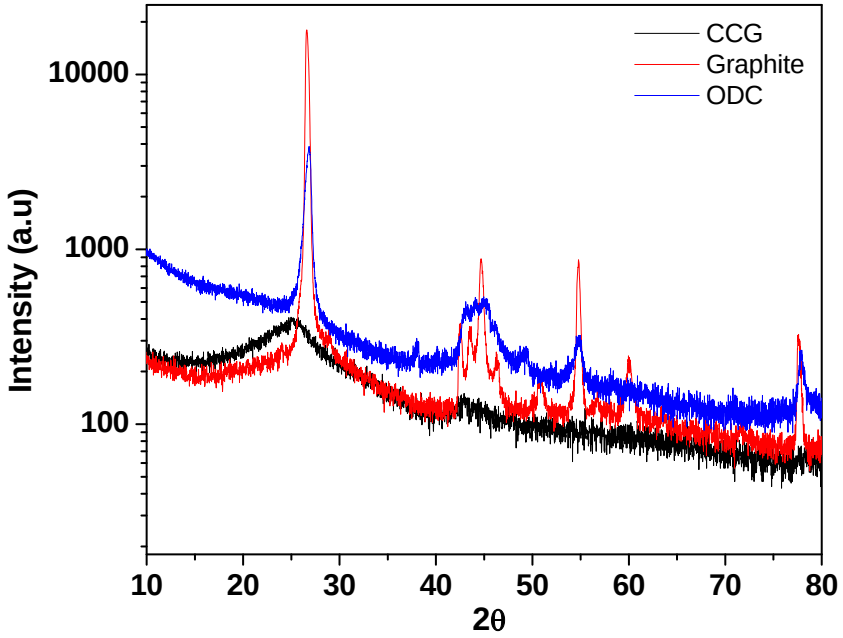

Figure 6.3 *Comparison of the XRD of ODC with commercial graphite flakes and chemically converted graphene (CCG)*

The Raman spectrum of the ODC (Figure 6.2d) exhibits signatures of porous crystalline graphitic material formed by the 3D assembly of n-layers of graphene nanosheets. [47, 48] The G band arising out of the in-plane stretching vibrations of sp^2 carbons occurs at 1570 cm^{-1} in ODC. The defect induced D peak is observed at 1318 cm^{-1} along with the second order overtone 2D (usually occurs in single layer/few layer graphene and crystalline graphitic materials) which is seen at 2647 cm^{-1} (inset). An increasing disorder in the graphene sheets results in the D′ band which occurs as a

shoulder to the G band. This is observed in the ODC at ~1604 cm^{-1}. The disorder is probably a result of the porosity induced in the graphitic material in our case as well as the increased number of graphene layer stacking in the crystallite. [49-51] The D′ band is observed in commercial graphite but absent in graphene. The I_D/I_G ratio of ODC is ~1.10 which is much more than commercial graphite flakes (0.37) and slightly lower than chemically converted graphene (1.20). This can be attributed to the increased porosity and possible decrease in the number of graphene layers as compared to graphite, but a slightly greater degree of order as compared to CCG. This behavior is perfectly consistent with the FWHM which shows that the ordering of the ODC system is exactly between that of graphite and chemically obtained few layer graphene (Figure 6.4). Figure 6.4 gives a detailed comparison of the ODC with commercial graphite flakes and chemically obtained reduced graphene oxide. Further detailed analysis of the Raman spectra is described.

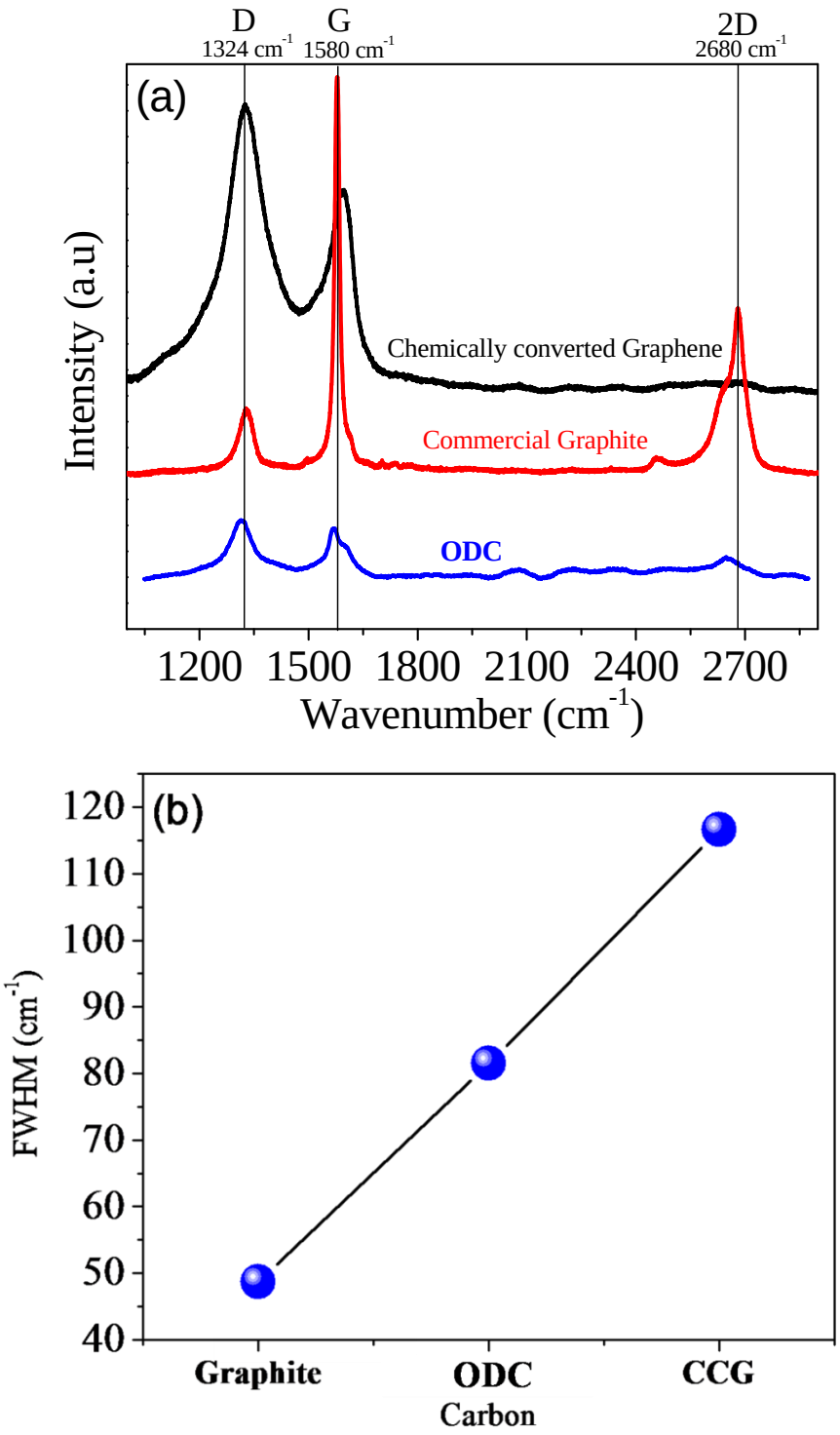

Figure 6.4 *(a) Raman spectra comparison of ODC with commercial graphite and chemically converted graphene (CCG) (b) FWHM of the D peak of ODC, commercial graphite and CCG.*

Defect free single layer/few layer graphene synthesized by CVD usually shows a strong and sharp 2D band. With increasing number of layers (towards graphite formation) the 2D band becomes less intense and broader due to splitting which

results from an increasing number of modes. The chemically converted graphene usually does not possess the 2D band due to a large number of defects.

The FWHM values of the D peak for commercial graphite flakes and the synthesized ODC is 76.8 cm^{-1} and 87.8 cm^{-1}, respectively. The FWHM of 2D peaks and I_{2D}: I_G ratios give an indication of the number of graphene layers in the crystallite. The I_{2D}: I_G ratio is ~ 0.45 and 0.39 respectively. This gives an indication of similar number of layers in both these materials. However this may not give a precise indication for the ODC case because it possesses more number of defects due to its porous structure. Hence the possibility of lesser number of graphene layers in this structure as compared to commercial graphite cannot be denied.

Figure 6.5 depicts the HR-TEM images of the graphene layer assembled porous n-graphene cage like structure. The general structure is clearly presented in Figure 6.5a, b which shows the porous graphene assembly into the n-graphene lattices. Figure 6.5c presents the individual graphene sheets which form the building blocks of this 3D assembly. Interestingly hexagonal n-graphene cages are also clearly visible in Figure 6.5d.

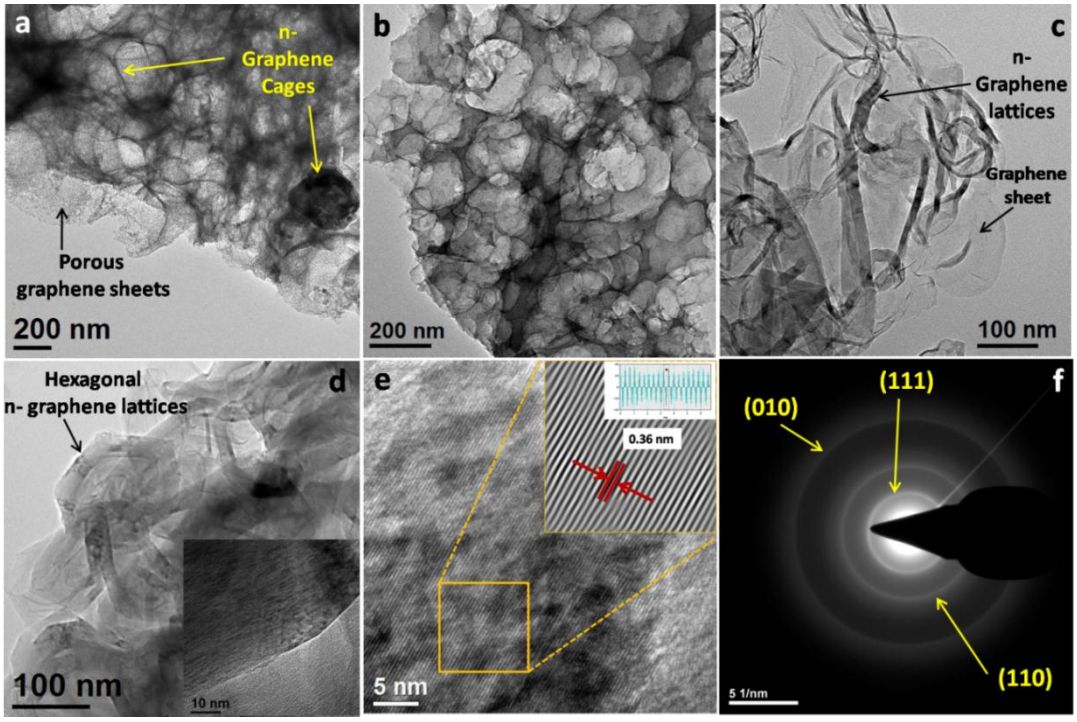

Figure 6.5 *HR-TEM images of the n-graphene cages formed by the assembly of porous graphene sheets: (a, b) Porous n-graphene cage like assembly of graphene sheets; (c) Graphene sheets; (d) Hexagonal n-graphene lattices; (e) Lattice fringes clearly indicating a d-spacing of 0.36 nm which is that of graphite; (f) the electron diffraction pattern confirming the presence of principle graphite-like planes.*

A higher resolution analysis of these lattices (Figure 6.5e) establishes a *d*-spacing of 0.36 nm which is in tune with the interlayer spacing in crystalline graphite. Selected area electron diffraction pattern (Figure 6.5f) is a further confirmation of the presence of crystalline hexagonal graphite lattices e.g. (010), (111) and (110). Figure 6.6

exhibits the presence of porosity along with the crystalline n-graphene arrangement at a very high resolution. FE SEM images (Figure 6.7) re-affirm the existing characteristics of the material. Figure 6.7a is a low magnification image which show graphite-like crystallites. Higher magnification images (Figure 6.7 b-d) clearly show that these graphite crystallites have a porous cage like microstructure formed by the self assembly of graphene sheets.

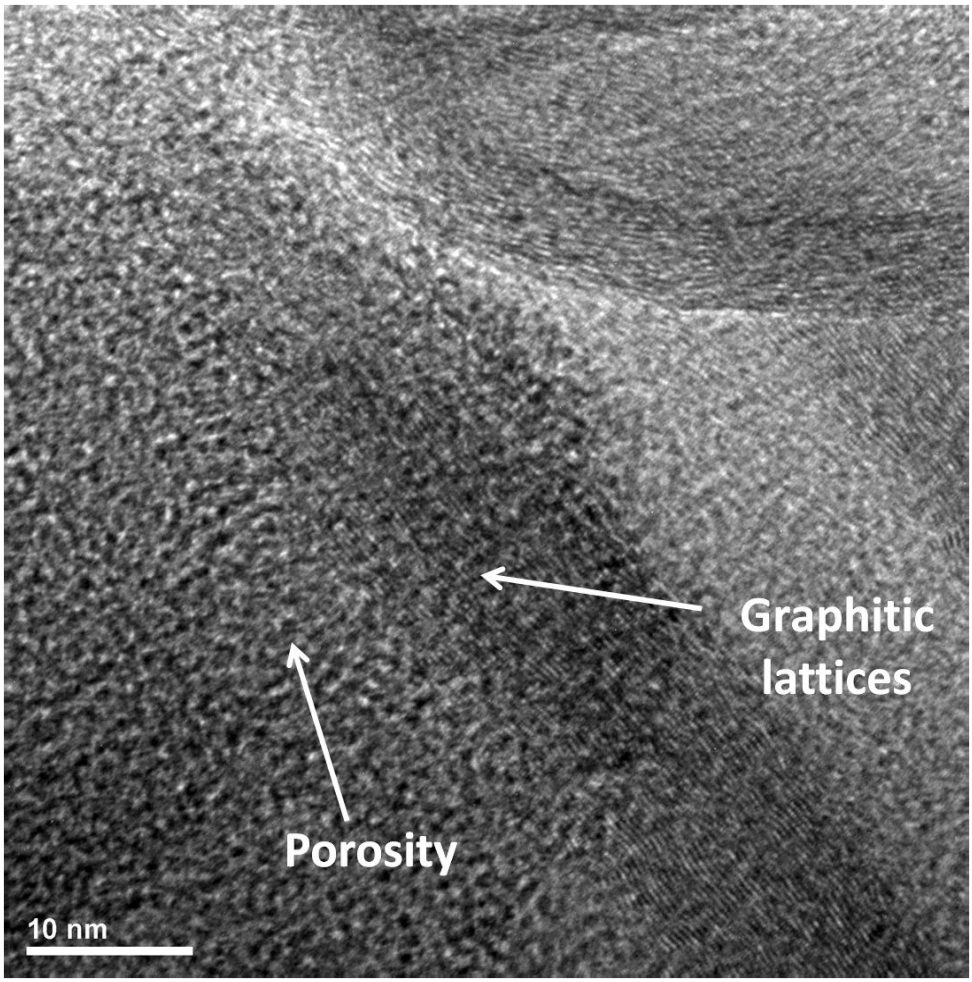

Figure 6.6 High resolution HR TEM of graphitic lattices with porosity in the graphitic carbon

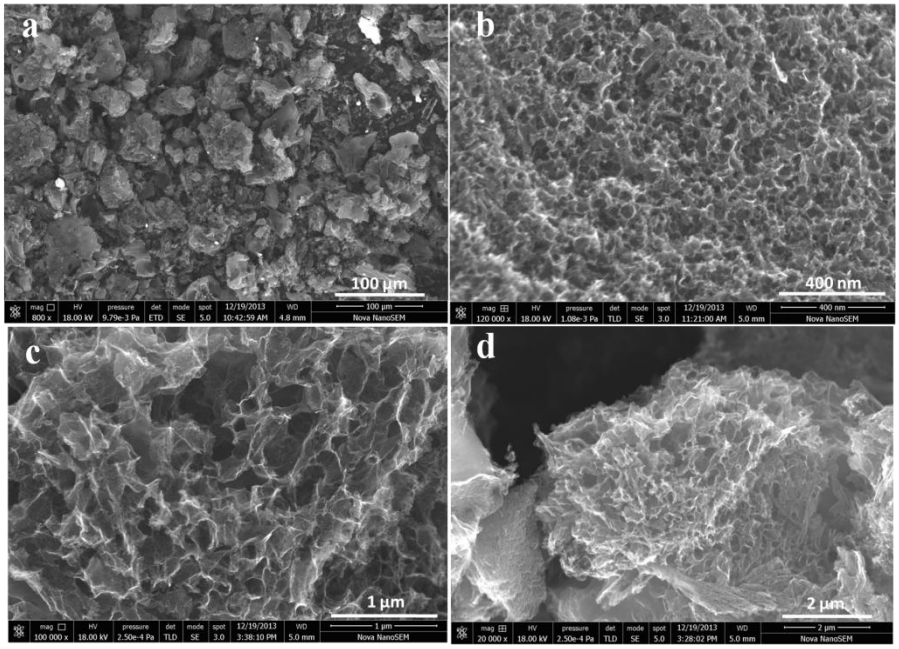

Figure 6.7 FESEM images of (a) Graphite like crystallites observed at lower magnification; (b-d) 3D assembly of graphene sheets into porous cage network seen under different magnifications.

XPS (Figure 6.8) shows the presence of three important elements, Carbon, Nitrogen and Oxygen. As expected a high proportion of carbon is observed in the material (Figure 6.8a). This carbon mainly exists in the sp^2 form (peak at 284.7 eV) and also the carbon bonded to oxygen C-O at 285.9 eV. Notably a very high content of doped nitrogen ~16% (Figure 6.8b) is observed due to the large number of nitrogen functionalities in the precursor and the low pyrolysis temperature (800^0C). The nitrogen peak at 400.6 eV is the quarternary or graphitic N in the carbon matrix and the peak at 398.3 eV can be attributed to the pyridinic nitrogen. Heavy nitrogen doping can enhance the conductivity of the ODC leading to a better rate capability and simultaneous increase in energy density in the Li-HEC device. This is clearly the implication of the appropriate choice of the precursor in this case. Figure 6.8c also shows the presence of oxygen in the material.

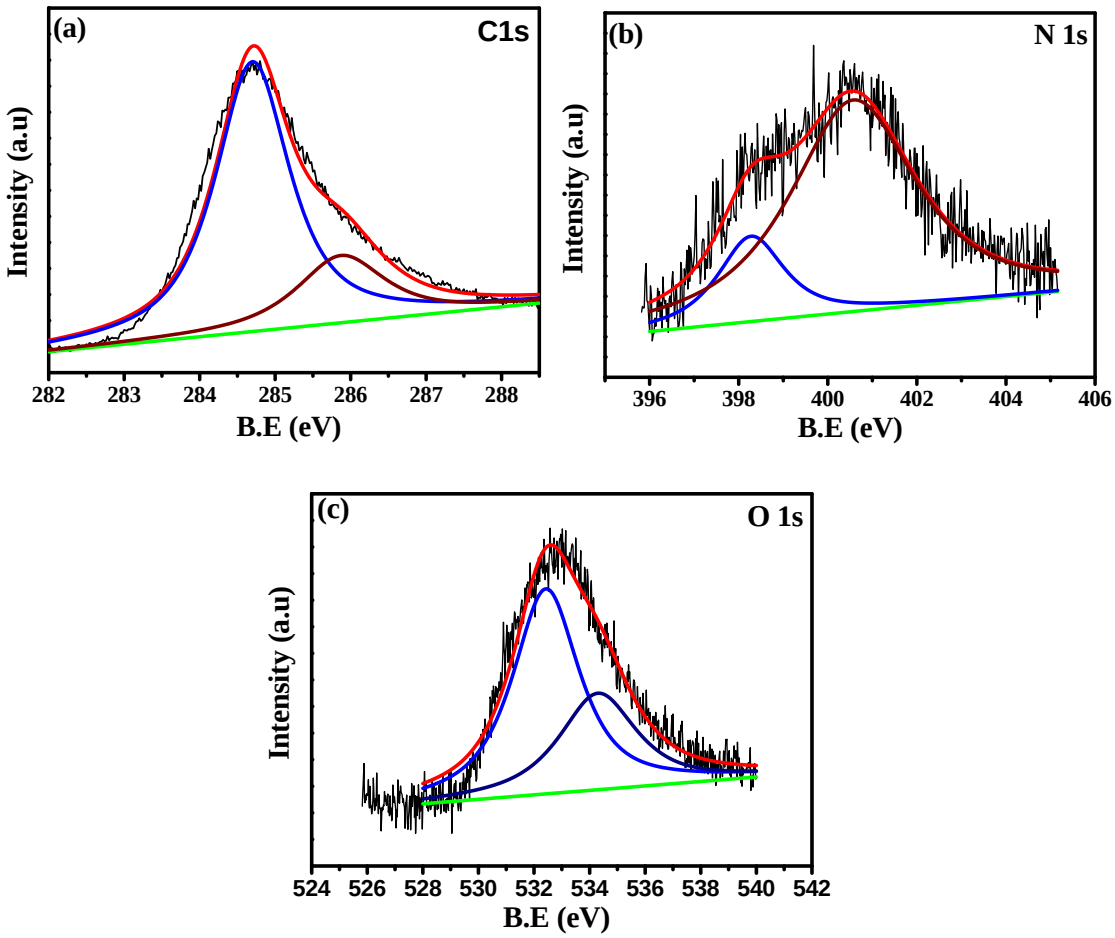

Figure 6.8 *XPS of ODC (a) C 1s (b) N 1s (c) O 1s*

As stated earlier, 4-aminobenzoic acid was used as a monomer for the free radical polymerization in order to generate a short chain polymer. The free radical initiator used in this process is APS. A similar polymerization process is generally used in the synthesis of polyaniline chains from aniline. In this case though only short chain polymers are synthesized due to an apparent quick quenching of free radicals generated in the process. This could be due to the additional functional groups present on the aromatic ring. The 4-aminobenzoic acid was chosen as the precursor because of the presence of a COOH group on the ring. This -COOH group can be readily converted into its sodium salt (-COONa) in the oligomeric chain (Figure 6.9A). During the pyrolysis process adjacent –COONa groups get converted into sodium carbonate Na_2CO_3 and result in generation of pores in the carbonaceous matrix by a process similar to activation. This entire process of introducing porosity creating functional groups on the monomer/polymers prior to carbonization could be termed as

a 'molecular activation'. Interestingly, the formation of Na_2CO_3 from –COONa groups on adjacent chains also results in a stitching together of the adjacent carbonized polymer chains. This gives rise to a sheet like morphology. [20] These graphene sheets formed during pyrolysis, stack or self assemble together into nanocrystalline graphitic (n-layer graphene) cages. Since the oligomers possess short chain length, the graphite lattices eventually formed exhibit nano-sized dimensions. Figure 6.9 (A) shows the schematic of the oligomer synthesis. An equimolar amount of NaOH and the monomer precursor were used. Figure 6.9(B) shows the 3D images of the monomer (a), oligomer (b), and the final carbonized graphitic cages (c).

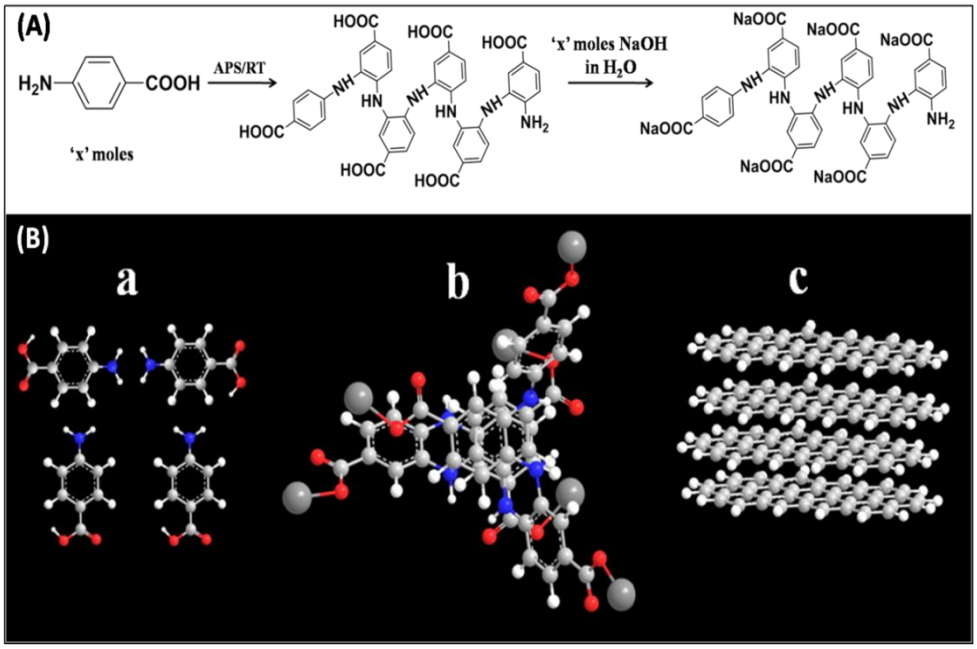

Figure 6.9 *(A) Schematic representation of the synthesis mechanism; (B) 3D molecular representation of the precursor and product structures.*

The BET specific surface area obtained from the N_2 adsorption data shows a high value of 1381 $m^2\ g^{-1}$ which indicates that the ODC is suitable as an electrode material for use in supercapacitors. Figure 6.10a shows the N_2 adsorption–desorption isotherm and Figure 6.10b shows the pore size distribution obtained from it. The pore size distribution indicates a perfectly hierarchical porosity which is suitable for electrochemical double layer capacitor (EDLC) applications. Highest concentration of

pores is in the micropore domain with pore diameters in the range of 1-2 nm. Such micropores assist in a large amount of accommodation of ions. A significant concentration of pores are observed in the mesopore domain (pore diameter of 2- 6 nm). These pores assist in the fast transport of the electrolyte ions and provide access to the micropores for the ion storage. Some macropores (> 10 nm) are also present in the ODC which act as electrolyte reservoirs. [52]

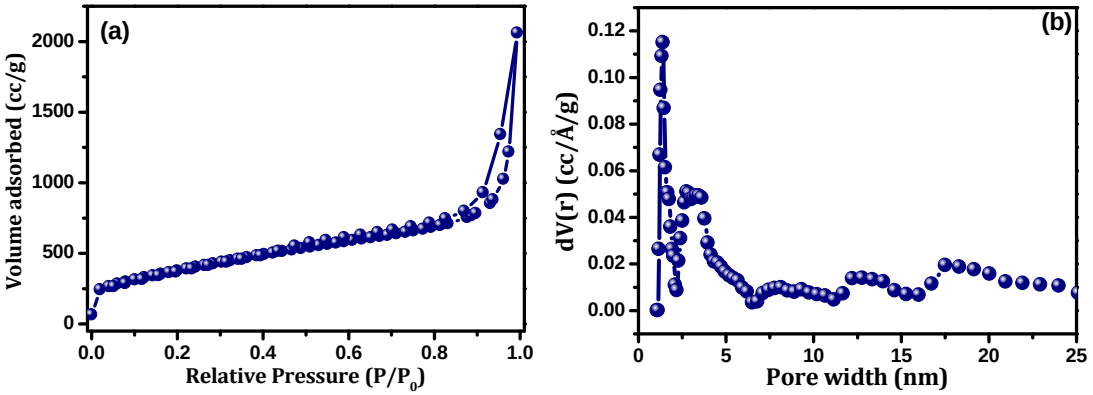

Figure 6.10 *BET surface area analysis: a) Adsorption isotherm for ODC b) Pore size distribution*

Li-HEC was fabricated with ODC as the cathode and commercially available $Li_4Ti_5O_{12}$ as insertion anode in the presence of an organic electrolyte (1 M $LiPF_6$ in EC: DEC). Before the fabrication of Li-HEC, an appropriate optimization between the mass loadings of the electrodes was carried out. In the case of symmetric supercapacitor *e.g.* EDLC (fabricated with same mass loading), the applied potential is divided between the two electrodes which is mainly because the both electrodes undergo same charge storage mechanism. On the other hand, in Li-HEC assembly, carbonaceous cathode involves the double layer formation and $Li_4Ti_5O_{12}$ undergoes Li-insertion/extraction reaction and therefore the applied potential gets divided according to the specific capacities of the individual electrodes. Mass balance was carried out based on the single electrode performance of the individual components with metallic Li under the same current density of 100 mA g^{-1}.

Single electrode performance of ODC with respect to metallic lithium (Li/ODC) and typical electrochemical profiles are illustrated in Figure 6.12. Figure 6.12a represents

the typical galvanostatic charge-discharge curves of ODC cycled between 3-4.6 V *vs.* Li in ambient conditions. A linear increase in time (*i.e.* capacity) with respect to potential indicates the formation of perfect electric double layer formation (PF_6^- anion double layer) across the electrode/electrolyte interface. Formation of such electric double layer has been clearly supported from the charge-discharge curves of ODC based symmetric supercapacitor configuration fabricated with same electrolyte solution (Figure 6.11). The specific capacitance for ODC was found to be 105 F g^{-1} at a current density of 1 A g^{-1}. The observed specific capacitance values are consistent with the previous reports of graphene nanosheets in organic medium. [53] Increasing current rate decreases the specific capacitance, for instance 60 F g^{-1} is noted at current density of 10 A g^{-1}. Along with high rate capability, the ODC retained ~90% of the initial capacitance even after 5000 cycles at current density of 4 A g^{-1}. From the electrochemical profiles of the ODC based symmetric supercapacitor, a mirror like triangular nature of the galvanostatic charge-discharge curve indicates the perfect EDLC behaviour i.e. non-Faradaic process with high reversibility. The half-cell delivered the initial reversible capacity of ~56 mAh g^{-1} at current density of 100 mA g^{-1}, which is almost two times higher than that of commercial AC (30-35 mAh g^{-1}) under the similar testing conditions. [29, 32]

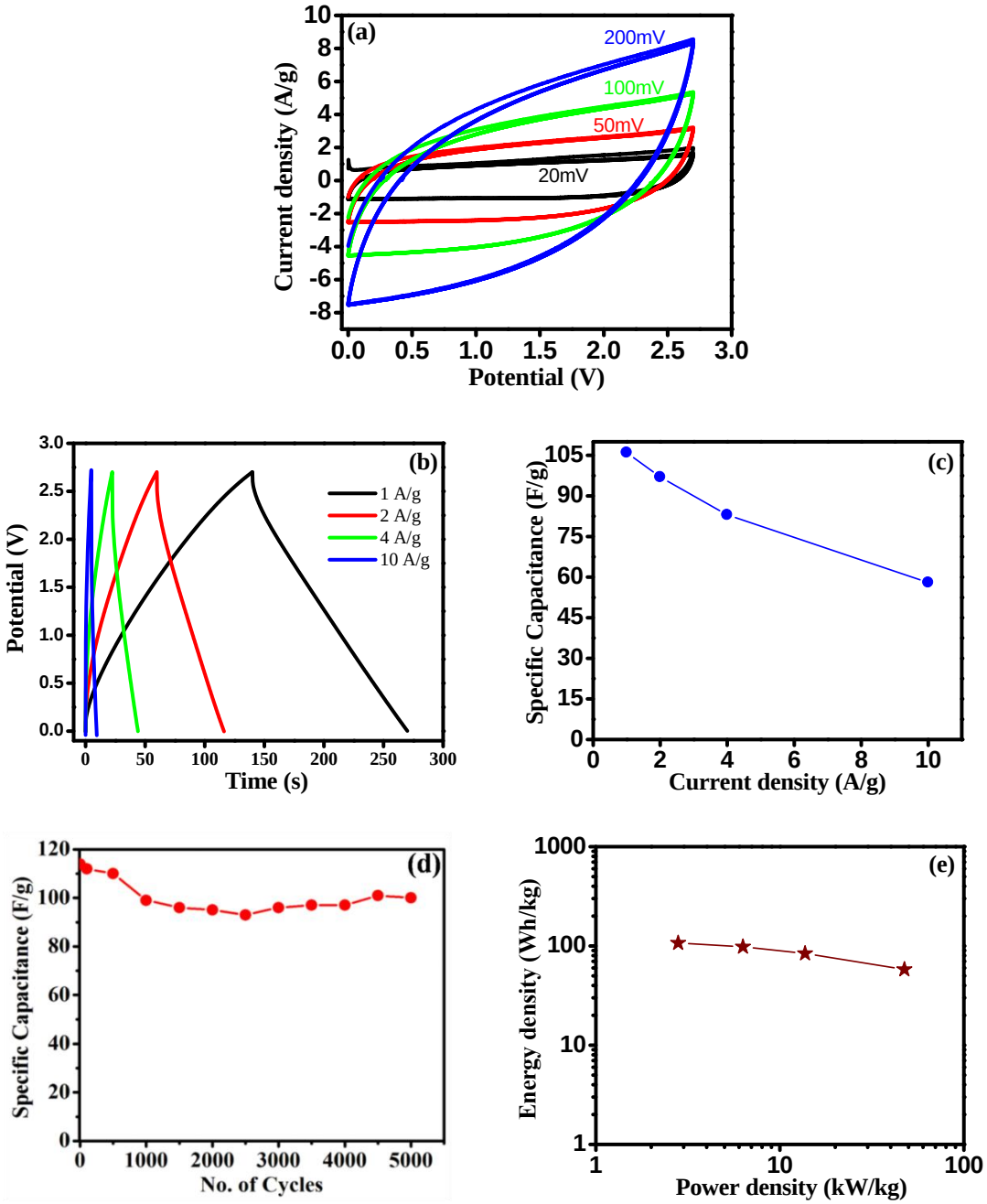

Figure 6.11 *(a) Plot of reversible capacity vs. cycle number of ODC in single electrode configuration between 3-4.6 V vs. Li at constant current density of 100 mA* g^{-1}*. Inset: Typical charge-discharge curves of Li/ODC cell, (b) Galvanostatic charge-discharge traces of ODC/*$Li_4Ti_5O_{12}$ *Li-HEC between 1-3 V at various current densities, (c) Ragone plot of OCD/*$Li_4Ti_5O_{12}$ *and commercial AC/*$Li_4Ti_5O_{12}$*, and (d) Cycling profiles of ODC/*$Li_4Ti_5O_{12}$ *Li-HEC at current density of 2 A* g^{-1}.

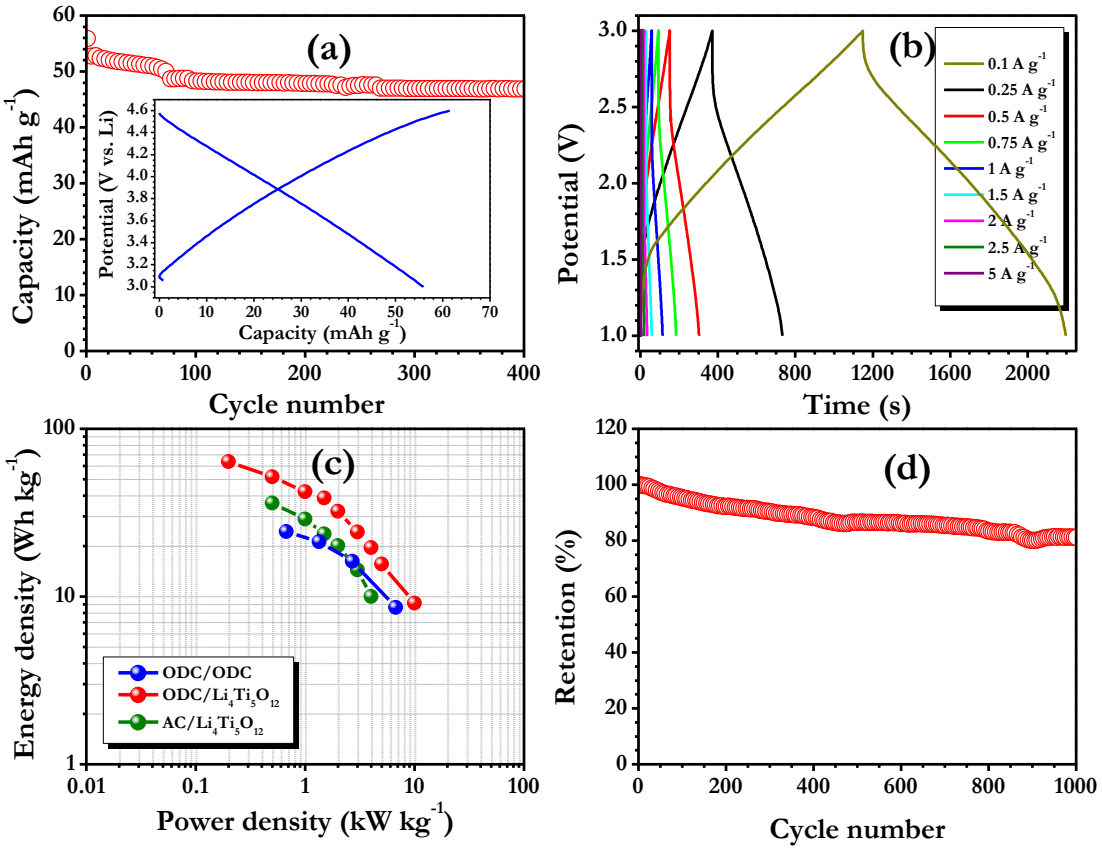

Figure 6.12 *(a) Plot of reversible capacity vs. cycle number of ODC in single electrode configuration between 3-4.6 V vs. Li at constant current density of 100 mA* g^{-1}*. Inset: Typical charge-discharge curves of Li/ODC cell, (b) Galvanostatic charge-discharge traces of ODC/*$Li_4Ti_5O_{12}$ *Li-HEC between 1-3 V at various current densities, (c) Ragone plot of OCD/*$Li_4Ti_5O_{12}$ *and commercial AC/*$Li_4Ti_5O_{12}$*, and (d) Cycling profiles of ODC/*$Li_4Ti_5O_{12}$ *Li-HEC at current density of 2 A* g^{-1}.

This enhanced performance is mainly because of high specific surface area and tailored mesoporosity along with electronic connectivity offered by the graphene nanosheets assembled in a 3D structure. The single electrode performance clearly suggests that ODC is a promising candidate to employ them in Li-HEC configuration as cathode active material to conquer high energy density.

Based on the electrochemical performance of both ODC and insertion anode $Li_4Ti_5O_{12}$ in single electrode configuration (Figure 6.13) at the same current density, the mass loading between anode to cathode was fixed at a ratio of 1:3.04 (3 mg: 9.10 mg) for the construction of Li-HEC. The Li-HEC was cycled between 1-3 V at

various current densities in ambient temperature (Figure 6.12b). It is worth mentioning that the applied current is calculated based on the total active mass of both the electrodes (12.10 mg), for example, 12.1 mA is applied at a current density of 1 A g^{-1}. Apparent to note that, increasing current density results in decrease in the reaction time. This decrease in reaction time is mainly due to the involvement of only the surface of the active material in the electrochemical reaction, rather than bulk system at high current rates. In so far as the charge storage mechanism is concerned, during charge, Li-ions are intercalated into spinel $Li_4Ti_5O_{12}$ lattice and simultaneously the anion, PF_6^- is adsorbed on the ODC surface to maintain the charge neutrality in the electrolyte solution. In the discharge process the mentioned reaction is completely reversed. The specific energy (E_{SP}) and power densities (P_{SP}) are calculated using the following relations: $P_{SP} = (\Delta E \cdot i/m)$ and $E_{SP} = (P_{SP} \cdot t)$, where

$$\Delta E = (E_{max} + E_{min})/2$$

and E_{max} and E_{min} are, respectively, the potential at beginning of discharge and at the end of discharge curves of galvanostatic cycle, m is the mass of active material used to fabricate Li-HEC (12.1 mg). [21, 29, 32, 37, 54] The ODC based Li-HEC was noted to be capable of delivering the maximum energy density and power density of ~63 Wh kg^{-1} and ~10 kW kg^{-1}, respectively. The observed energy density is much higher than the commercially available activated carbon (AC)/$Li_4Ti_5O_{12}$ based system in the same testing conditions and its symmetric configuration as well (Figure 6.12c). The ODC based Li-HEC not only outperforms the commercial AC/$Li_4Ti_5O_{12}$ system, but also displays much better performance than previously reported graphene based Li-HEC. For instance, Stoller et al. [40] first reported the utilization of KOH activated microwave exfoliated graphite oxide as cathode with spinel $Li_4Ti_5O_{12}$ and this system delivered the energy density of 40.8 Wh kg^{-1}. Similarly, trigol reduced graphene oxide/$Li_4Ti_5O_{12}$ system reported by our group (~45 Wh kg^{-1}) as well. [37] Cycleability is another important criterion to evaluate the compatibility during prolonged cycling. In this regard, ODC/$Li_4Ti_5O_{12}$ Li-HEC was cycled at current density of 2 A g^{-1} and the cycling profiles are given in Figure 6.12d. It can be clearly seen that only a meagre fading occurs during cycling, with the retention of ~81% of the initial value. This fading is mainly because of the intrinsic nature of the commercially available $Li_4Ti_5O_{12}$ anode used which can be tackled by adopting either carbon coating or

making composites with carbonaceous materials to further enhance the power capability of the system. [33]

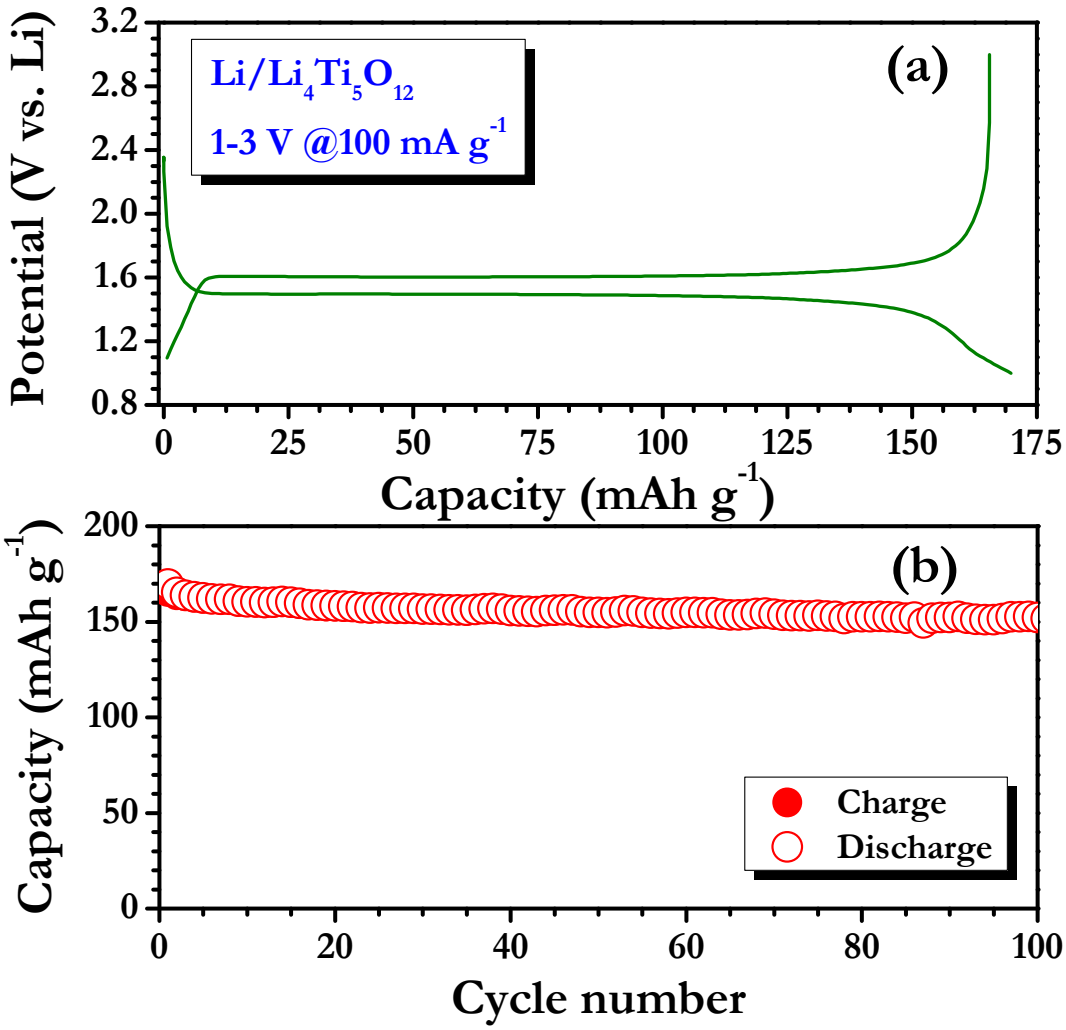

Figure 6.13 Galvanostatic charge-discharge curves of $Li/Li_4Ti_5O_{12}$ (Sigma-Aldrich, USA) half-cells cycled between 1-3 V *vs.* Li at constant current density of 100 mA g^{-1}, and (b) plot of capacity *vs.* cycle number.

6.4 Conclusion

A 3D high surface area n-graphene cage morphology is reported by pyrolysis of a tailored oligomer. It evolves through self assembly of porous graphene networks. The sodium salt form of oligomer is derived from 4-amino benzoic acid. Specific functional groups on the precursors, namely –COONa render a molecular level activation without any external activating agent. This carbon is used as the positive electrode for the construction of Li-HEC application with $Li_4Ti_5O_{12}$ anode in an organic medium. The Li-HEC delivered exceptional performance delivering an energy density of ~63 Wh kg^{-1} which is higher than the graphene based materials. The present study opens up new avenues for the preparation of 3D architectures of high surface area porous graphenes based on tailored oligomer/polymer precursors.

References

1. C. Kim, B. T. N. Ngoc, K. S. Yang, M. Kojima, Y. A. Kim, Y. J. Kim, M. Endo and S. C. Yang, Advanced Materials, 2007, 19, 2341-2346.
2. J. Wang and S. Kaskel, Journal of Materials Chemistry, 2012, 22, 23710-23725.
3. H. Wang, Z. Xu, A. Kohandehghan, Z. Li, K. Cui, X. Tan, T. J. Stephenson, C. K. Kingondu, C. M. B. Holt, B. C. Olsen, J. K. Tak, D. Harfield, A. O. Anyia and D. Mitlin, ACS Nano, 2013, 7, 5131-5141.
4. M. Sevilla and A. B. Fuertes, Energy & Environmental Science, 2011, 4, 1765-1771.
5. K. Gergova and S. Eser, Carbon, 1996, 34, 879-888.
6. H. Zhu, X. Wang, X. Liu and X. Yang, Advanced Materials, 2012, 24, 6524-6529.
7. Q. Zhao, T.-P. Fellinger, M. Antonietti and J. Yuan, Journal of Materials Chemistry A, 2013, 1, 5113-5120.
8. J. Yuan, C. Giordano and M. Antonietti, Chemistry of Materials, 2010, 22, 5003-5012.

9. X. Yang, D. Wu, X. Chen and R. Fu, The Journal of Physical Chemistry C, 2010, 114, 8581-8586.
10. Z. Xiang, Y. Xue, D. Cao, L. Huang, J.-F. Chen and L. Dai, Angewandte Chemie International Edition, 2014, 53, 2433-2437.
11. X. Xiang, E. Liu, Y. Wu, Y. Tian, H. Xie, Z. Wu and Y. Zhu, Fuel Cells, 2012, 12, 892-897.
12. T. Morishita, Y. Soneda, T. Tsumura and M. Inagaki, Carbon, 2006, 44, 2360-2367.
13. D.-C. Guo, J. Mi, G.-P. Hao, W. Dong, G. Xiong, W.-C. Li and A.-H. Lu, Energy & Environmental Science, 2013, 6, 652-659.
14. N. Gavrilov, I. A. PaÅ¡ti, M. VujkoviÄ‡, J. Travas-Sejdic, G. Ä†iriÄ‡-MarjanoviÄ‡ and S. V. Mentus, Carbon, 2012, 50, 3915-3927.
15. L. Qie, W. Chen, H. Xu, X. Xiong, Y. Jiang, F. Zou, X. Hu, Y. Xin, Z. Zhang and Y. Huang, Energy & Environmental Science, 2013, 6, 2497-2504.
16. L. Wei, M. Sevilla, A. B. Fuertes, R. Mokaya and G. Yushin, Advanced Functional Materials, 2012, 22, 827-834.
17. Y. Liang, H. Liu, Z. Li, R. Fu and D. Wu, Journal of Materials Chemistry A, 2013, 1, 15207-15211.
18. X. Wang, C.-G. Liu, D. Neff, P. F. Fulvio, R. T. Mayes, A. Zhamu, Q. Fang, G. Chen, H. M. Meyer, B. Z. Jang and S. Dai, Journal of Materials Chemistry A, 2013, 1, 7920-7926.
19. M. Zhong, E. K. Kim, J. P. McGann, S.-E. Chun, J. F. Whitacre, M. Jaroniec, K. Matyjaszewski and T. Kowalewski, Journal of the American Chemical Society, 2012, 134, 14846-14857.
20. P. Yadav, A. Banerjee, S. Unni, J. Jog, S. Kurungot and S. Ogale, ChemSusChem, 2012, 5, 2159-2164.
21. D. Puthusseri, V. Aravindan, S. Madhavi and S. Ogale, Electrochimica Acta, 2014, 130, 766-770.
22. D. Puthusseri, V. Aravindan, S. Madhavi and S. Ogale, Energy & Environmental Science, 2014, 7, 728-735.
23. Y. Zhao, C. Hu, Y. Hu, H. Cheng, G. Shi and L. Qu, Angewandte Chemie, 2012, 124, 11533-11537.
24. L. Zhang, F. Zhang, X. Yang, G. Long, Y. Wu, T. Zhang, K. Leng, Y. Huang, Y. Ma, A. Yu and Y. Chen, Sci. Rep., 2013, 3.

25. M. A. Worsley, S. O. Kucheyev, H. E. Mason, M. D. Merrill, B. P. Mayer, J. Lewicki, C. A. Valdez, M. E. Suss, M. Stadermann, P. J. Pauzauskie, J. H. Satcher, J. Biener and T. F. Baumann, Chemical Communications, 2012, 48, 8428-8430.
26. X. Cao, Y. Shi, W. Shi, G. Lu, X. Huang, Q. Yan, Q. Zhang and H. Zhang, Small, 2011, 7, 3163-3168.
27. G. G. Amatucci, F. Badway, A. Du Pasquier and T. Zheng, Journal of The Electrochemical Society, 2001, 148, A930-A939.
28. I. Plitz, A. DuPasquier, F. Badway, J. Gural, N. Pereira, A. Gmitter and G. G. Amatucci, Applied Physics A: Materials Science & Processing, 2006, 82, 615-626.
29. V. Aravindan, W. Chuiling and S. Madhavi, Journal of Materials Chemistry, 2012, 22, 16026-16031.
30. V. Aravindan, N. Shubha, W. C. Ling and S. Madhavi, Journal of Materials Chemistry A, 2013, 1, 6145-6151.
31. V. Aravindan, M. V. Reddy, S. Madhavi, S. G. Mhaisalkar, G. V. Subba Rao and B. V. R. Chowdari, Journal of Power Sources, 2011, 196, 8850-8854.
32. V. Aravindan, W. Chuiling, M. V. Reddy, G. V. S. Rao, B. V. R. Chowdari and S. Madhavi, Physical Chemistry Chemical Physics, 2012, 14, 5808-5814.
33. K. Naoi, W. Naoi, S. Aoyagi, J.-i. Miyamoto and T. Kamino, Accounts of Chemical Research, 2013, 46, 1075-1083.
34. K. Naoi and P. Simon, Electrochemical Society Interface, 2008, 17, 34-37.
35. K. Naoi, Fuel Cells, 2010, 10, 825-833.
36. K. Naoi and Y. Nagano, in Supercapacitors, Wiley-VCH Verlag GmbH & Co. KGaA, Weinheim, Germany, 2013, pp. 239-256.
37. V. Aravindan, D. Mhamane, W. C. Ling, S. Ogale and S. Madhavi, ChemSusChem, 2013, 6, 2240-2244.
38. A. Jain, V. Aravindan, S. Jayaraman, P. S. Kumar, R. Balasubramanian, S. Ramakrishna, S. Madhavi and M. Srinivasan, Scientific reports, 2013, 3.
39. A. Banerjee, K. K. Upadhyay, D. Puthusseri, V. Aravindan, S. Madhavi and S. Ogale, Nanoscale, 2014, 6, 4387-4394.
40. M. D. Stoller, S. Murali, N. Quarles, Y. Zhu, J. R. Potts, X. Zhu, H.-W. Ha and R. S. Ruoff, Physical Chemistry Chemical Physics, 2012, 14, 3388-3391.

41. D. Mhamane, S. M. Unni, A. Suryawanshi, O. Game, C. Rode, B. Hannoyer, S. Kurungot and S. Ogale, Journal of Materials Chemistry, 2012, 22, 11140-11145.
42. Z. Wei and M. Wan, Advanced Materials, 2002, 14, 1314-1317.
43. S. K. Pillalamarri, F. D. Blum, A. T. Tokuhiro and M. F. Bertino, Chemistry of Materials, 2005, 17, 5941-5944.
44. J. Huang and R. B. Kaner, Journal of the American Chemical Society, 2003, 126, 851-855.
45. S. C. N. H. S. O Chan, W. S. Sim, K. L. Tan and B. T. G. Tan, Macromolecules, 1992, 25, 6029-6034.
46. A. F. S. A. A. Khalil, M. M. Azab, A. A. Mahmoud, A. M. Metwally, J Polym Res, 2013, 20.
47. A. J. M. S. Dresselhaus, A. G. Souza Filho, R. Saito, Phil. Trans. R. Soc. A, 2010, 368, 5355-5377.
48. L. G. CanÃ§ado, M. A. Pimenta, B. R. A. Neves, M. S. S. Dantas and A. Jorio, Physical Review Letters, 2004, 93, 247401.
49. A. C. Ferrari and D. M. Basko, Nature Nanotechnology, 2013, 8, 235-246.
50. A. C. Ferrari and J. Robertson, Physical Review B, 2000, 61, 14095-14107.
51. F. Tuinstra and J. L. Koenig, The Journal of Chemical Physics, 1970, 53, 1126-1130.
52. A. G. Pandolfo and A. F. Hollenkamp, Journal of Power Sources, 2006, 157, 11-27.
53. Y. Sun, Q. Wu and G. Shi, Energy & Environmental Science, 2011, 4, 1113-1132.
54. H. Kim, K.-Y. Park, M.-Y. Cho, M.-H. Kim, J. Hong, S.-K. Jung, K. C. Roh and K. Kang, ChemElectroChem, 2014, 1, 125-130.

Chapter 7

Research Summary and Future Scope

In this chapter some of the salient features of our work have highlighted and an attempt to summarize the entire PhD research has been made. In addition to this a broad vision for future research work has also been provided.

7.1 Thesis Summary

The objective of this thesis was to develop novel routes towards the synthesis of functional carbon forms for different energy applications like energy storage and energy generation.

Traditionally carbon macro, micro and nanoforms have been synthesized by physical and chemical methods that include chemical vapour deposition, pulsed laser deposition, arc discharge, pyrolysis, hydrothermal or chemical synthetic routes. All these techniques either involve high temperatures or high energies for the processing. In my research a new photochemical route towards the synthesis of carbon materials has been explored. This process involves a rapid photochemical reaction of free radicals resulting in the formation of carbon nano-forms. The process can take place at room temperature and ambient conditions. This bottom-up process involves the use of small haloaromatic molecule precursors. We demonstrate that this process can be used to make a range of carbon nanoparticles and films. It is also shown that this photochemical process presents new avenues and possibilities of forming new carbon structural and molecular forms which have been hitherto unexplored. Furthermore, in the PhD research, the use of protein rich food waste like gram flour to generate porous hetero-atom doped carbon forms was also explored by 'cooking' the flour in a SiO_2 nanoparticle solution. The hierarchically porous carbon was used as an efficient catalyst in the cathodic oxygen reduction reaction of fuel cells. Finally some exploration into specific synthesis of oligomerss with in-situ functional groups that give rise to molecular level activation on pyrolysis was carried out. The carbon synthesized by this method was used as a high performance material in Li-ion hybrid electrochemical capacitor for energy storage.

Specific results that we obtained have been summarized herein:

1) Pulsed laser induced photochemical stitching (PLPS) process is introduced to engineer solid carbon nanoparticles from liquid halobenzenes by laser photochemistry at room temperature and laboratory environment. Electrically conducting high surface area carbon nano-spheres (CNSs) have thus been directly synthesized from routine laboratory solvents. Furthermore, in principle, a complete conversion of liquid materials (CB & DCB) to solid

carbon can be achieved by a cyclic process of solvent irradiation and distillation to recycle the solvent followed by further irradiation, which we have confirmed. Laser photochemical synthesis does not require high temperature that is usually associated with the synthesis of carbon based materials facilitating the synthesis of carbon nanocomposites with polymers and other organic compounds.

2) Unique vertically aligned and hierarchically carbon nanoparticle-self assembled film morphology of conducting carbon with a broccoli-like structure was realized by PLPS involving irradiation of a supported DCB film. Such films exhibit remarkable superhydrophobicity that can be easily process-tuned. Given the electronically conducting and porous nature of the carbon films, we explored their application as counter electrodes in dye sensitized solar cells. The laser generated carbon on FTO-glass surfaces demonstrates excellent catalytic activity, which is almost comparable to the established Pt-coated FTO counter electrodes. Furthermore, this new laser induced photochemical deposition process can be implemented on several substrates to generate different morphologies of carbon.

3) We demonstrated the novel synthesis and applicability of a metal free, nitrogen-doped, hierarchically porous, oxygen-functionalized highly-conducting carbon electrocatalyst for oxygen reduction reaction (ORR) in an alkaline electrolyte. The material exhibited remarkable electrocatalytic behaviour due to the synergistic effects of high conductance, hierarchical porosity and heteroatom doping which are simultaneously achieved in the synthesis of this catalyst. The process involves the utilization of protein rich-food grains, making it a sustainable, potentially large scale alternative for synthesis of an efficient carbon based electrocatalyst for ORR in AEMFCs.

4) A 3D high surface area n-graphene cage morphology is done by pyrolysis of a tailored oligomer. It evolves through self assembly of porous graphene networks. The sodium salt form of oligomer is derived from 4-amino benzoic acid. Specific functional groups on the precursors, namely –COONa render a

molecular level activation without any external activating agent. This carbon is used as the positive electrode for the construction of Li-HEC application with $Li_4Ti_5O_{12}$ anode in an organic medium. The Li-HEC delivered exceptional performance delivering an energy density of ~63 Wh kg^{-1} which is higher than the graphene based materials. The present study opens up new avenues for the preparation of 3D architectures of high surface area porous graphenes based on tailored oligomer/polymer precursors.

7.2 Future work

1. **Synthesis of Transition metal/N/Carbon catalysts for the Oxygen Reduction Reaction in Fuel Cells:**

With an ever increasing global energy requirement and simultaneously depleting availability of conventional resources accompanied by the extensive environmental damage caused by them, the need for alternative clean energy generation and storage systems has gained momentum in recent days. Solar cells (Silicon, DSCs, QDSCs), Fuel Cells have been widely explored for harvesting sun's enormous energy and devices like Ultracapacitors, Batteries have been used to store this harvested energy. However the use of precious metals (eg. Platinum) and oxides (eg. FTO, ITO etc) in these devices make them expensive and less cost effective. There are also several stability issues for oxide based supercapacitors (pseudocapacitors) that limit their widespread usage. In light of these drawbacks, the use of carbon materials and carbon-metal/metal oxide composites in many of the energy harvesting and storage devices has been studied in the last decade with promising results. Carbon is an important material since it offers inexpensive synthetic routes (like pyrolysis, CVD, hydrothermal synthesis etc.) in addition to a very stable chemical nature. Carbon composites with metal and metal oxide systems also offer a significant advantage of enhanced performance and stability along with cost effective synthesis procedures.

One of the major obstacles to the large scale deployment of fuel cell technology is the oxygen reduction step at the cathode. Commercially Pt/C based systems are used as catalysts for this reduction step. However these systems are expensive, not durable and possess slow electron-transfer kinetics. Hence several alternative systems have been studied. They include materials like N coordinated transition metal macromolecules, chalcogenides, oxynitrides etc. Recently doped carbon nanomaterials (N, S doped CNTs, Graphene, Mesoporous carbon etc.) have been shown to exhibit a very good electrocatalytic activity in the ORR process. Co-doping carbon nanostructures with more than one heteroatom (N, S, B) has also been employed to further increase the ORR catalytic performance of carbon. Doped/ undoped carbon composites with transition metal systems have also been tested effectively for their catalytic performance.

With the use of novel polymer, small molecules and other precursors like metal organic frameworks, I would be interested in the synthesis of such M-N-C based systems for application in electrocatalysis in the future. Different transition metals and doped carbon structures will be incorporated for the same purpose.

2. Synthesis of porous carbons from specifically designed polymers

Use of polymers for synthesis of porous carbon materials has been less explored due to their cost and tedious synthetic protocols involved. In the near future my target would be design cost-effective and facile synthetic pathways for the synthesis of polymers which possess active functional group that give rise to porosity in the final pyrolyzed carbon product. The polymers would also contribute in providing a strong structural framework to the final carbon material

Appendix

This appendix section deals with two different works carried out during the course of this PhD. In chapter 4, we had discussed the formation of carbon films with a broccoli like morphology for application in solar cells. Section I of the appendix deals with a different application of these carbon films, namely field emission. Section II deals with the synthesis of graphene quantum dots by the PLPS method described in this thesis. The GQDs are used in biological applications.

Section I

Field Emission Studies:

Electron sources are the chief building blocks of various applications such as flat panel displays, x-ray sources, mass spectrometers and space based applications like thrusters, tethers etc. In all these applications thermionic emitters have been replaced by the field emitters. This has become possible because of the current developments of cheap and robust field emitters. The ideal field emitter should possess high aspect ratio, and good conductivity material with high mechanical strength, in addition to being robust, cheap and easy to process. Carbon based materials like CNT, [1] Graphene, [2] and Diamond [3] have already demonstrated their ability to become potential candidates as field emitters. In this work we studied the field emission (FE) behavior of three different specimens viz, 3 minute laser irradiated film (Specimen A), 5 minute laser irradiated film (Specimen B) and a rather interesting case of a thin layer graphene drop-cast on the 3 minute laser irradiated carbon film (Specimen C). The field emission current density-electric field (J-E) characteristics were obtained in all-metal field emission microscope with load-lock chamber in ultra high vacuum (UHV) conditions. The experimental procedures for current density measurements are described in detail elsewhere [g]. In this study, the effective emission area was ~0.25 cm^2 and cathode to anode distance was kept ~500 µm for all the specimen.

Figure A1 (a) depicts the field emission current density as a function of applied electric field (J-E). The turn-on field, defined as the field required to draw an emission current of ~ 10 $\mu A/cm^2$, is found to be ~ 9 V/µm, 7.5 V/µm and 5.6 V/µm for Specimen A, B and C respectively. The results are summarized in Table 5.

Specimen	**Turn-on Field, to draw J = 10 µA/cm^2**	**Threshold Field, to draw J = 100 µA/cm^2**
Specimen A	**9 V/µm**	**11 V/µm**
Specimen B	**7.5 V/µm**	**9.9 V/µm**
Specimen C	**5.6 V/µm**	**7.9 V/µm**

Table A1*: Table of Comparison*

From **Table A1**, it is seen that the FE properties of Specimen A are inferior to Specimen B. The reason for this behavior is the difference in their morphology. The SEM image of Specimen B reveals that the carbon nanoparticle matrix is quite dense in this case as compared to Specimen A. Moreover careful observation shows that the number of carbon nanoparticles embedded in an individual matrix is higher in Specimen B, which means more number of emitters are available.

The FE properties of Specimen C are far superior to those of Specimen A and B. This is because in sample C the effective electron emission takes place from both, the carbon nanoparticles and graphene. The atomically sharp edge of the graphene sheet can act as an additional emission site and hence the turn-on field is observed to decrease. Moreover the dispensed graphene sheets would be crumpled on a rough morphology increasing the number of favorable emitting points. The FE properties of carbon films can thus be tuned further by forming a composite or heterostructure. It will be interesting to examine *in situ* (in process) formation of rough and conducting carbon based nanocomposite films by the process discussed herein.

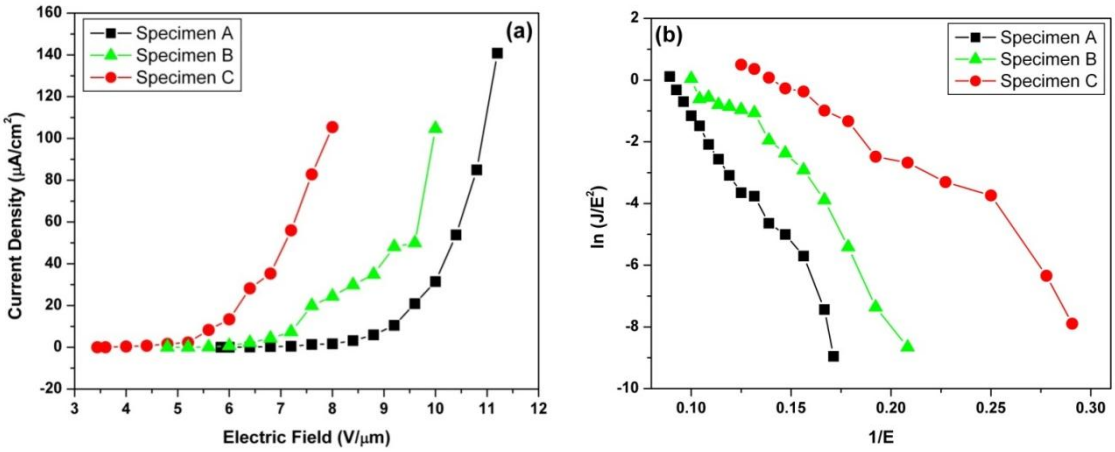

Figure A1. *Field emission Characteristics (a) Current density-applied electric field (J-E) characteristics. (b) Corresponding Fowler-Nordheim (F-N) plot.*

The Fowler-Nordheim (F-N) plot derived from the observed JE characteristic is shown in **Figure A1** (b). The F-N plot shows an overall linear behavior with decrease in the slope (non-linearity) at very high applied field range.

References

1. Z. Wu, S. Pei, W. Ren, D. Tang, L. Gao, B. Liu, F. Li, C. Liu, H. Cheng, Advanced Materials 2009, 21, 1756-1760.
2. W. Kang, J. Davidson, Y. Wong, K. Holmes, Diamond and Related Materials 2004, 13, 975-981
3. D. Shinde, P. Chavan, S. Sen, D. Joag, M. More, S. Gadkari, S. Gupta, ACS Appl. Mater. Interfaces 2011, 3, 4730–4735

Section II

1. Introduction

In view of the recent explosion in research on luminescent carbon nanoparticles or carbon dots, it is quite evident that such biocompatible fluorescent carbon systems are at the vanguard of several applications ranging from photovoltaics to biology. Owing to their favourable characteristics of solution processibility, biocompatibility, low toxicity, chemical inertness, and low cost of synthesis, these materials hold a great promise as replacements for toxic semiconductor quantum dots in most of the application domains.[1] Graphene quantum dots (GQDs) constitute a newly discovered class of carbon dots that have been explored for synthesis, structure, luminescence and various applications.[2] GQDs are largely categorized as large polyaromatic species or nano-graphene particles having dimensions in the range of 1-100 nm with stacking up to 10 layers and possessing a size dependent tunable bandgap. Established synthesis protocols for GQDs include top-down chemical approaches like hydrothermal[3] and electrochemical[4] cutting of graphene sheets, solvothermal routes,[5] nanolithography techniques,[6] hydrazine hydrate reduction of graphene oxide,[7] electrochemical synthesis[8] and oxygen plasma treatment of graphene[9]. Alternately bottom-up routes to synthesize GQDs involve techniques like cage opening of fullerenes[10] or use of several organic synthetic chemistry methods as well. [2a, 11]

Pulsed laser-induced photochemical stitching (PLPS) has been recently introduced as a new, room temperature technique for generating conducting carbon nanostructures and thin films from small haloaromatic molecules like chlorobenzene and o-dichlorobenzene.[12] In this communication, PLPS is demonstrated as a novel, facile photochemical bottom-up route toward the synthesis of fluorescent GQDs using a small molecule haloaromatic precursor.

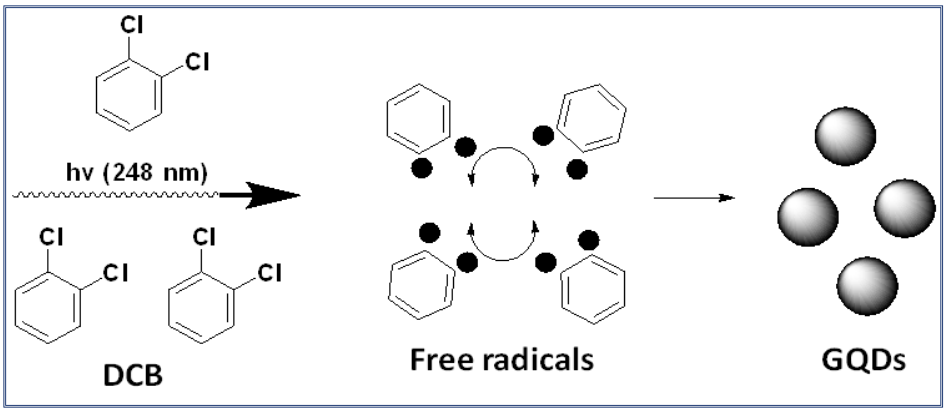

Figure 1. *Schematic representation of the mechanism*

UV laser irradiation entails bombardment of a large number of photons on the targeted system. When high energy photons of wavelength 248 nm generated by a KrF excimer laser, strike small haloaromatic molecules like chlorobenzene and dichlorobenzene, the carbon-halogen bond undergoes homolytic photochemical cleavage resulting in a large number of free radicals (**Figure 1**). These aromatic free radicals are then reorganized by 'stitching together' into carbon nanospheres. The process, however, occurs stepwise. The free radicals initially combine to yield large polyaromatic molecules (GQD structures), some of which grow in dimensions with increasing time of laser irradiation. The increased surface energy of these grown structures in solution causes them to curl into nanospheres of carbon. Hence transparent liquid o-dichlorobenzene (DCB) when irradiated by UV laser photons turns black in colour due to the formation of carbon powder.[12b] This carbon residue can be separated by filtration of the liquid through a PTFE membrane (0.2 μm pore size). Interestingly, a large concentration of GQDs remains in the irradiated liquid after removal of the residual carbon matter by ultrafiltration because of their high dispersibility and nano-sized dimensions. Thus the filtrate obtained is a brownish yellow coloured liquid system that is rich in fluorescent GQDs (Figure S1) (Supporting Information). The carbon powder (GQDs) can be isolated by removal of the DCB by distillation. The process proves to be very efficient as the entire liquid precursor is retained and can be reused.

Experimental Section

50 ml of o-Dichlorobenzene in a quartz beaker was irradiated by UV laser pulses for a time period of 10 minutes. (KrF excimer, λ = 248 nm, energy density ~ 170 mJ/cm^2, pulse duration 20 ns, pulse repetition rate =10 Hz). The resulting liquid was filtered through a 0.2 µm pore size PTFE membrane to discard the carbon residue formed. The light brown coloured filtrate was collected. The fluorescent GQDs were isolated by removal of the dichlorobenzene in the filtrate by distillation. The product was redispersed in dichloromethane, vacuum dried and analyzed.

Results and Discussion

The X-ray diffraction (XRD) pattern of the sample (**Figure 2a**) shows a broad peak at 2Θ = 25.5. This is a broadened and shifted peak of graphite (002 plane).[13] The XRD thus indicates the presence of a graphitic carbon domain in the sample. A few layer stacking of nano-graphene domains in the GQDs gives rise to this peak in XRD. Fourier transform infrared (FTIR) spectrum (**Figure 2b**) of the GQDs points to the presence of aromatic C=C bonds (1450 cm^{-1} and 1582 cm^{-1}). In addition to several other peaks, the spectrum also shows the C=O peak at 1715 cm^{-1}. GQDs are known to possess C=O peaks at their edges.

Elemental analysis of our sample was done by X-ray photoelectron spectroscopy (XPS). XPS analysis primarily shows the presence of carbon as the chief constituent in the sample along with additional presence of oxygen and chlorine. The nature of the carbon in the sample was studied from the XPS spectrum (**Figure 2c**). It is clear from the graph that carbon exists largely in the C=C (sp^2) form (identified by the peak at 284.7 eV) along with additional C=O, C-O and the residual C-Cl groups from the reactant molecules. The XPS study of Cl and O content was also done (**Figure S2- SI**).

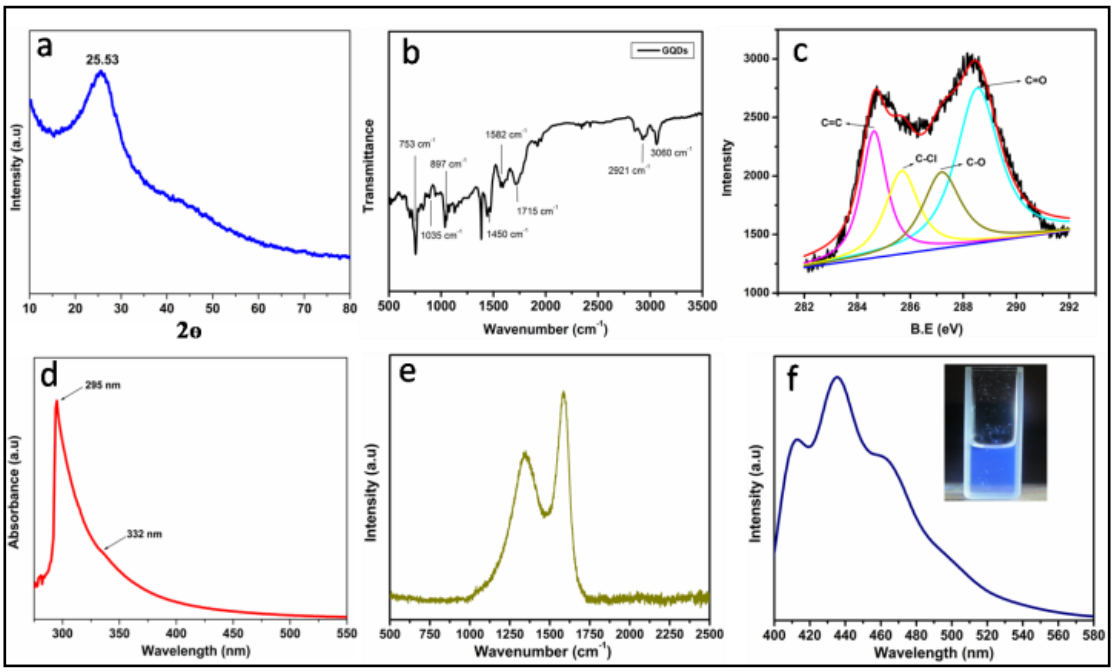

Figure 2. *Characterization of the GQDs in the sample a. X-Ray Diffraction pattern b. FT-Infrared absorption spectrum c. X-ray Photoelectron Spectroscopy d. UV-visible absorption spectrum e. Raman spectrum f. PL spectrum (inset: blue fluorescence visible under UV lamp)*

The UV-Visible absorption spectrum of the sample (**Figure 2d**) shows a strong absorption by the particles at 295 nm. This possibly arises due to the π- π* transition of electrons in the molecular orbital of GQDs. A shoulder peak at 332 nm is also observed. This is a typical characteristic of graphene containing species and arises due to the n-π* transition of electrons in the molecular orbital of the C=O group in GQDs. Furthermore, GQDs are known to possess a size and shape dependent band gap and hence several varieties of such particles synthesized in different ways show a varying light absorption behavior.

The Raman spectrum of the sample is shown in **Figure 2e**. The D band which arises due to the κ-point phonons of A_{1g} symmetry clearly appears at 1340 cm^{-1}, along with the usual G band (1583 cm^{-1}) that appears in sp^2 carbons (E_{2g} phonons).[14] The low I_D: I_G ratio (~ 0.73) value indicates a low number of defects (sp^3 sites, oxygen/nitrogen defects) in these nanoparticles. This is probably a reflection of the

photochemical synthesis method. Since the carbon nanostructures are formed by a molecule by molecule photochemical stitching process, and the process takes place at room temperature/pressure, the defect population is controlled. However the D band in these structures arises due to the size induced defects in the carbon system.

The sample shows a bright blue luminescence in the visible (**Figure 2f**) when excited in UV light (365 nm). The photoluminescence (PL) emission is broad over a range of 400 to 580 nm in the visible spectrum, typical of luminescent carbon nanostructures. The maximum emission at ~ 440 nm and the shoulders at ~410 and 460 nm arise due to the variable size distribution of the GQDs. A quantum yield of 2.56 % was calculated for these particles using Quinine sulfate as the standard, by a reported procedure (**Figure S3 - SI**).[15] Though the precise cause of luminescence in carbon nanostructures has not yet been conclusively established, there have been several hypotheses on this topic. Surface emissive defects that cause quantum confinement effects are proposed to be primarily responsible for luminescence in crystalline and amorphous carbon nanoparticles and nanodiamonds.[1, 16] Eda et al.[17] attributed the blue luminescence from chemically derived GO to the presence of isolated sp^2 clusters in a largely carbon-oxygen sp^3 matrix resulting in localization of the e-h pairs facilitating radiative recombination. However a strong explanation for the blue luminescence from GQDs was provided by Pan et al. [3] It was proposed that the emissive sites for the luminescence are the free zigzag sites at the edges of the graphitic particles that have a triplet ground state. Due to the small size of GQDs, such zigzag sites are present in a large concentration. The triplet states are represented by the electronic configuration of $\sigma^1\pi^1$ with each unpaired electron occupying a sigma and pi-orbital each. On absorption of a photon from the excitation wavelength, an electron is excited from the highest occupied molecular orbital (HOMO) (σ and π) to the lowest unoccupied molecular orbital (LUMO). Such electrons relax by radiative decay giving rise to the observed intense PL. Similar explanation was also given by Peng et al.[18] to explain the blue luminescence of the GQDs derived from carbon fibers.

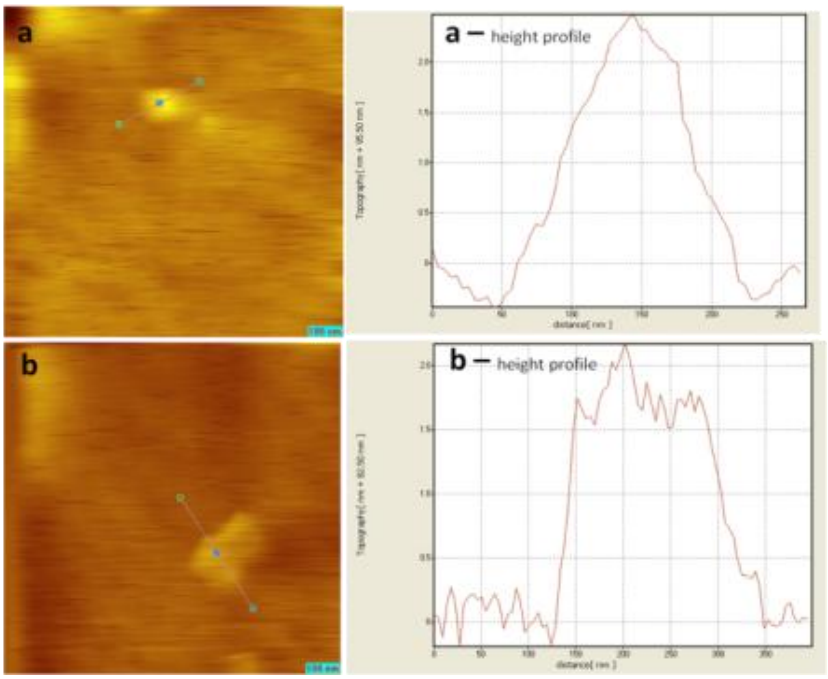

Figure 3. *a. AFM image of the GQDs in a specific area with their height profile b. Similar AFM images of GQDs in another area with height profile.*

To conclusively prove that the nanoparticles obtained by our method are GQDs that possess a few graphene layers, we performed atomic force microscopy (AFM) imaging (**Figure 3**) to obtain their topography. These images and the height profiles clearly prove that the thickness of GQDs was just above 2 nm indicating a presence of approximately 5 layers. The horizontal size of these particles appears to be larger in the AFM images because it is difficult to isolate the particles completely. They exist as a lateral agglomeration, a fact which is indicated further by the transmission electron microscopy (TEM) images as well. However their thickness values can be determined.

TEM images (**Figure 4**) of the GQDs exhibit their nanosized dimensions. Figure 4a-c show that most GQDs have size in the range of 15-30 nm. The lattice fringes are clearly visible in the high resolution TEM images (**Figure 4c-inset**). As a confirmation of the graphene-like arrangement in the nanoparticles the hexagonal atomic arrangement of carbon atoms in the lattice is also clearly identified in **Figure 4d**.

One may question whether polyaromatic hydrocarbons (PAHs) formed in photochemical processes could be the reason for the blue luminescence observed. However we can

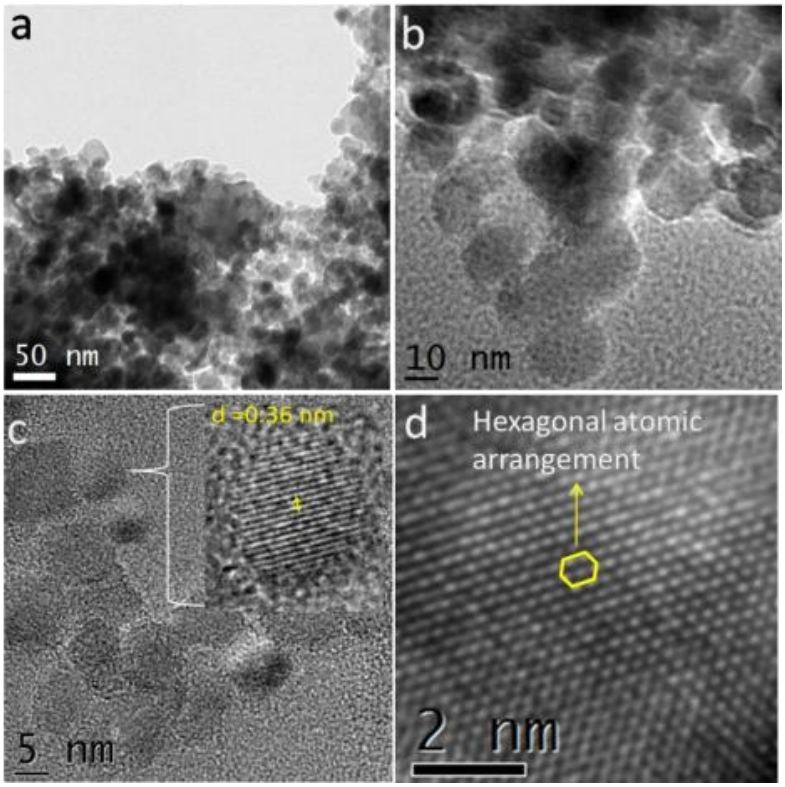

Figure 4. *TEM images a-b. GQDs at different scales c. GQDs with magnified image of lattice fringes (inset) (d=0.36 nm) d. Hexagonal atomic arrangement visible at high resolution.*

systematically prove that the products obtained in our experiment are GQDs and not PAHs. Firstly the XRD pattern observed in the product is ample proof that the product has graphitic origin and does not simply comprise of large organic molecules. Secondly, the Raman spectra of several blue luminescent PAHs (eg. anthracene, phenanthrene, triphenylene, pyrene, fluorene, and naphthalene) studied in literature show multiple intense sharp peaks in the region of 700-800 cm^{-1} (eg. peaks at753, 756, 696, 763 cm^{-1}) and 1000-1060 cm^{-1} (eg. 1010, 1012, 1059, 1036 cm^{-1}). [19] These peaks have not been observed in the Raman spectra obtained for the GQDs, ruling out the possibility of any substantial PAH contamination. Thirdly, UV-visible absorption spectra of these PAHs show intense sharp absorption peaks at 220, 262, 251, 251, 256 nm for naphthalene, fluorene, anthracene, phenanthrene, triphenylene respectively and several multiple peaks at 240, 272, 305, 318, 334 nm for pyrene.[19b] The absence of

these signatures in our data further establish our argument in favor of GQDs. Finally, it is a well known fact that PAHs are carcinogenic and toxic in nature. Hence considerable research has been dedicated to the removal of PAHs. However the GQDs obtained in our research show a very strong biocompatibility as discussed further.

Biological Studies

Fluorescent GQDs have been previously explored for their use as probes in bioimaging due to their stable PL and good biocompatibility. [2, 15, 18, 20] In our study we have used these laser synthesized GQDs (post-functionalization) as fluorescent probes for cellular imaging.

Functionalization of GQDs

In order to use the GQDs in the biological domain, their water dispersibility is an essential criteria.For this purpose 50 mg of the carbon powder (GQDs) was refluxed in conc. HNO_3 (69 % GR) for 12 hrs at 100ºC with continuous stirring. The water-dispersible functionalized dots were removed by centrifugation. Further washing was done by centrifugation (10000 rpm for 10 mins) in dilute aqueous NaOH solution and de-ionized water respectively (2 to 3 times).

Cell Phagocytosis

To study the general use of GQDs as such probes we used them to detect two different types of human cell lines, macrophages and HEK (Human Embryonic Kidney) cells. These cells were cultured in their respective appropriate medium and were incubated with the fluorescent GQDs for a particular period of time. The confocal microscopy images were later obtained at an excitation of wavelength 405 nm. It was clearly observed that the GQDs are present outside the ThP-1 macrophages cells around the membrane after a period of 30 mins (**Figure 5a**) and are internalised by the cells after 45 mins incubation (**Figure 5b**). Additional bio-imaging carried out with the HEK cells shows uniform distribution of fluorescent GQDs inside the cells and around the nucleus (**Figure 5c**).This fluorescence of the particles appears to be quite stable under the microscope. We thus show the efficient role of our GQDs as fluorescent nanoprobes in cellular bio-imaging. Additional details are given in SI.

Cytotoxicity and UV stability studies

Cell culture

NIH3T3 (Mouse Embryonic fibroblast cell line) cells were grown in Dulbecco's Modified Eagle's medium (DMEM, Gibco, Carlsbad, CA, USA) medium supplemented with bovine calf serum to a final concentration of 10% and penicillin / streptomycin under 5% CO_2 atmosphere at 37º C.

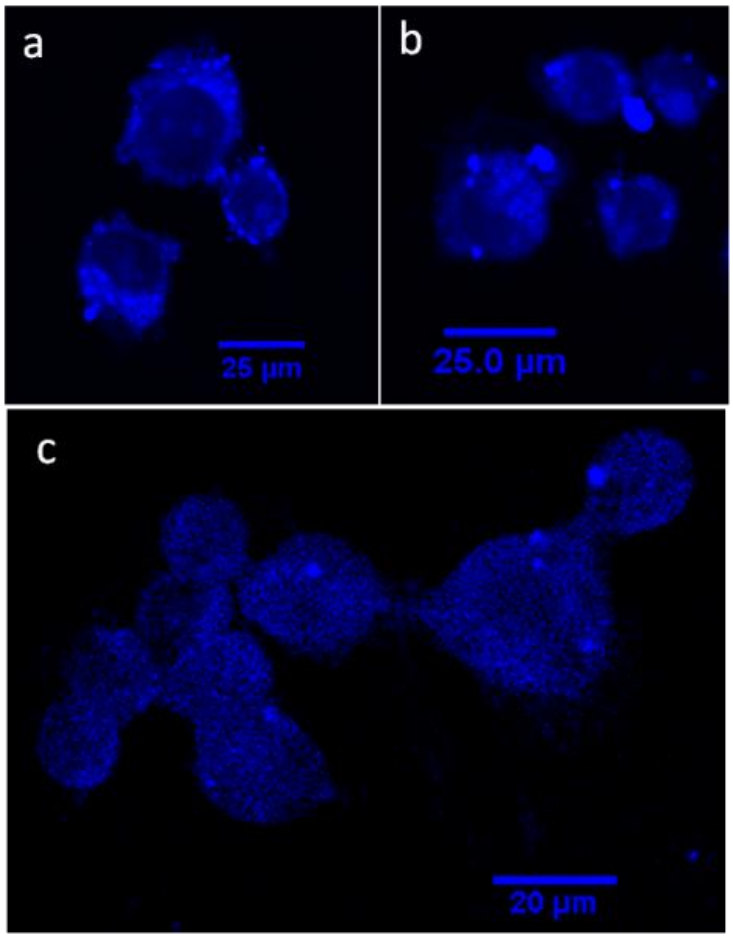

Figure 5. *a. Macrophages after 30 mins b. Macrophages after 45 mins c. HEK cells with GQDs.*

Cytotoxicity assay

The cytotoxicity of GQD particles on NIH3T3 was assessed by MTT (3-(4, 5-dimethylthiazol-2-yl)-2, 5-diphenyltetrazolium bromide) assay. For MTT assay, cells were seeded at the density of 104 cells/ well in 96 well plates and incubated for 12-16 hrs at 37º C before starting the treatment. Cells were treated with increasing

concentration of GQDs (in the range of 0.01µg/ ml to 10µg/ ml) and incubated for 48 hrs. At the end of incubation period, MTT solution was added to a final concentration of 0.05 mg/ ml to each well and incubated in dark at 37º C for 4 hrs. Formazan crystals were dissolved by adding 100 µl dimethyl sulfoxide to each well and the optical absorbance was measured at 540 nm on a plate reader. The readings in untreated cells were considered to be 100 % viable. **Figure 6a** shows the cell viability of above 80 % for different concentrations of the GQDs in water.

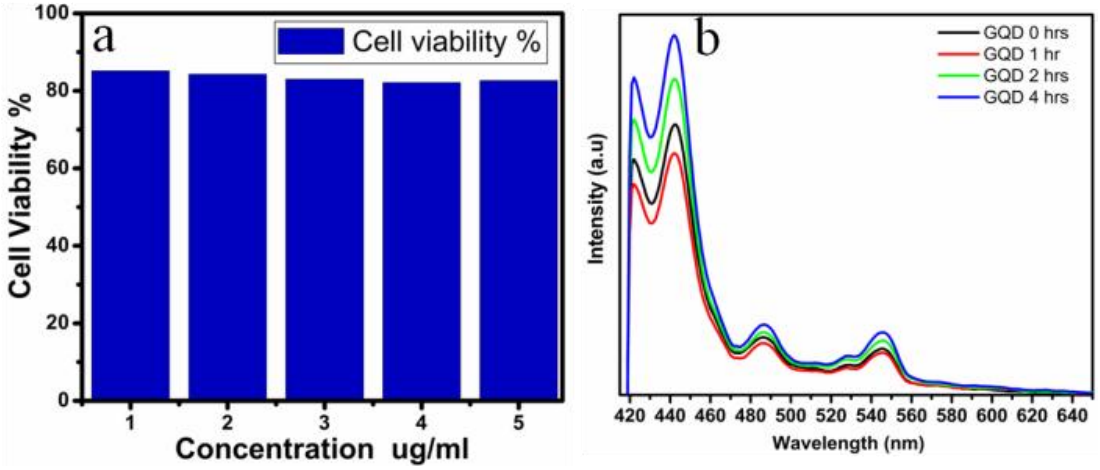

Figure 6. *a. Cell viability data for GQDs b. PL spectrum for UV treated GQDs in water.*

UV stability

The GQDs in water were tested for their stability under an intense UV lamp for up to 4 hrs. Interestingly there doesn't appear to be any drastic photo-bleaching effect on the functionalized GQDs. The emission of the GQDs remained stable about a mean value even after 4 hrs under the UV lamp (**Figure 6b**). This experiment determines the stability of these GQDs as luminescent probes even under constant and long UV exposure.

A laser photochemical route to synthesize blue-fluorescent GQDs from small aromatic molecules is demonstrated. The process offers a new room temperature, bottom-up pathway to the synthesis of GQDs which are important materials due to their diverse applicability, ranging from bio-imaging to photovoltaics The blue fluorescent GQDs have been shown to be effective for bio-imaging applications.

Since these GQDs are synthesized from organic solvents, they have a potential for application in photovoltaics. Laser photochemistry also offers potential routes to synthesize doped GQDs

References

[1] G. Baker. S. Baker, Angew. Chem. Int. Ed. 2010, 49.

[2] a. J. Shen, X. Yang, C. Li Chem. Commun. 2012, 48, 3686; b. Z. Zhang, N. Chen, L. Qu, Energy Environ. Sci. 2012 5, 8869.

[3] D. Pan, Z. Li, M. Wu Adv. Mater. 2010, 22.

[4] Y. Li, Y. Hu, Y. Zhao, G. Shi, L. Deng, Y. Hou et al. , Adv. Mater. 2011, 23, 776–780.

[5] S. Zhu. et. al., Chem. Commun. 2011, 47 6858–6860.

[6] L. Wang, Appl. Phys. Lett 2010, 97 262113.

[7] J. Shen, Y. Zhu, C. Chen, X. Yang, C. Li. , Chem. Commun. 2011, 47, 2580–2582.

[8] J. Zhou, C. Booker, R. Li, X. Zhou, T. Sham, X. Sun, Z. Ding, J. Am. Chem. Soc. 2007, 129, 744–745.

[9] T. Gokus et. al., ACS Nano 2009, 3, 3963-3968.

[10] J. Lu, P. Yeo, C. Gan, P. Wu, K. Loh, . Nat. Nanotechnol. 2011 6, 247–252.

[11] a. R. Liu, D. Wu, X. Feng, K. Mullen, J. Am. Chem. Soc. 2011, 133, 15221–15223; b. X. Yan, X. Cui, L. Li, J. Am. Chem. Soc. 2010, 132, 5944.

[12] a R. Gokhale et. al., Nanoscale 2012, 4, 6730; b. R. Gokhale, V. Thakare, S. Warule, b. Lefez, B. Hannoyer, J. Jog, S. Ogale AIP Advances 2012, 2, 022130.

[13] Z. Li, C. Lu, Z. Xia, Y. Zhou, Z. Luo, Carbon 2007, 45, 1686.

[14] A. Ferrari, J. Robertson, Phil. Trans. R. Soc. Lond. A 2004, 362, 2477.

[15] S. Sahu, B. Behera, T. Maiti, S. Mohapatra Chem. Commun. 2012, 48, 8835-8837.

[16] V. Mochalin, O. Shenderova, D. Ho, Y. Gogotsi, Nat. Nanotechnology 2012, 7, 11.

[17] G. Eda, Y. Lin, C. Mattevi, H. Yamaguchi, H. Chen, I. Chen, C. Chen, M. Chhowala Adv. Mater. 2010, 22, 505.

[18] D. Pan et. al., J. Mater. Chem. 2012, 22, 3314.

[19] L. Colangeli, V. Mennella, G. Baratta, E. Bussoletti, G. Strazzulla Astrophys. J. 1992, 396, 369; b. R. Rumelfanger, S. Asher, M. Perry, Appl. Spectrosc. 1988, 42 267-271.

[20] J. Peng et al., Nano Lett 2012, 12, 844.

List of Publications

- *Synthesis of an efficient heteroatom-doped carbon electro-catalyst for oxygen reduction reaction by pyrolysis of protein-rich pulse flour cooked with SiO_2 nanoparticles.* **R. Gokhale**, S. Unni, D. Puthusseri, S. Kurungot and S. Ogale. **Phys. Chem. Chem. Phys.**, 2014, 16, 4251-4259.

- *Blue luminescent graphene quantum dots by photochemical stitching of small aromatic molecules: Fluorescent nanoprobes in cellular imaging*. **R. Gokhale** and P. Singh, **Particle and Particle Syst. Charact.**, 2014, 31, 433-438.

- *Fluorescent sophorolipid molecular assembly and its magnetic nanoparticle loading: a pulsed laser process*. P. Singh, R. Mukherji, K. Joshi-Navare, A. Banerjee, **R. Gokhale**, S. Nagane, A. Prabhune, S. Ogale. **Green Chemistry**, 2013, 15, 943-953.

- *Laser synthesized super-hydrophobic conducting carbon with broccoli-type morphology as a counter-electrode for dye sensitized solar cells*. **R. Gokhale**, S. Agarkar, J. Debgupta, D. Shinde, B. Lefez, A. Banerjee, J. Jog, M. More, B. Hannoyer and S. Ogale. **Nanoscale**, 2012, *4*, 6730-6734.

- *MOF derived porous carbon–Fe_3O_4 nanocomposite as a high performance, recyclable environmental superadsorbent*. A. Banerjee, **R. Gokhale**, S. Bhatnagar, J. Jog, M. Bhardwaj, B. Lefez, B. Hannoyer and S. Ogale. **J. Mater. Chem**, 2012, *22*, 19694-19699.

- *From small aromatic molecules to functional nanostructured carbon by pulsed laser-induced photochemical stitching*. **R. Gokhale**, V. Thakare, S. Warule, B. Lefez, B. Hannoyer, J. Jog, and S. Ogale. **AIP Advances**, 2012, *2*, 022130.

- *Oligomer-salt derived 3D, heavily N-doped, n-layer graphene cages for Lithium ion hybrid electrochemical capacitors (Li-HEC) application*. **R. Gokhale**, V. Aravindan, P. Yadav, S. Jain, D. Phase, S. Madhavi and S. Ogale. Submitted to **Carbon**.

- *Large scale synthesis of graphene quantum dots (GQDs) from waste biomass and their use as efficient and selective photoluminescence on-off-on probe for Ag^{+} ions.* A. Suryawanshi, M. Biswal, D. Mhamane, **R. Gokhale**, S. Patil, D. Guin, and S. Ogale. Under Revision in **Nanoscale**.